UNIVERSITAT POLITÈCNICA DE CATALUNYA BARCELONATECH

Titanium dioxide and nanoshaped ceria for solar hydrogen production

Jarosław Serafin

Titanium dioxide and nanoshaped ceria for solar hydrogen production

This dissertation is submitted for the doctoral degree by

Jarosław Serafin

Directed by

Prof. Dr. Jordi Llorca Piqué

Dr. Luis Carlos Pardo

Thesis for compendium of publications

Universitat Politècnica de Catalunya

PhD Program in Chemical Process Engineering

February 2022

“If we knew what it was we were doing, it would not be called research, would it?”
— **Albert Einstein**

TO MY PARENTS

For raising me to believe that

anything was possible

Acknowledgments

I would like to thank my thesis advisors, Prof. Dr. Jordi Llorca Piqué and Dr. Luis Carlos Pardo Soto, for creating an extremely superior scientific research environment, for providing me with the best platform and resources, and for allowing me to devote myself to scientific research during my PhD study. Many thanks to my NEMEN group members in UPC especially Shiva, Isabel, Lluís, Ilaria, Xavier, Xènia, Nuria, Alejandro, Laia, Asier, Yufen, Andrea and Marina for their support and great contribution and constant and indispensable help.

Finally and most importantly, I would also like to thank my parents Krystyna and Adam for always being a reassuring certainty in any case present in my life. I would also like to thank my sister Ewa and my best friend Kinga.

Index

Contents

Summary

There are many methods of producing hydrogen from non-renewable fossil sources, but these methods have a negative environmental impact through emissions of pollutants and/or greenhouse gases. Therefore, alternative and environmentally friendly methods are being sought. The two main sustainable methods for producing hydrogen from renewable resources are the photocatalytic and thermocatalytic processes. This work focuses on the study of these processes on TiO_2 and CeO_2, respectively.

Although the development of photocatalytic research with the use of semiconductor photocatalysts does not last longer than about 40 years, this field of knowledge is gaining more and more interest from both science and industry. Photocatalytic water decomposition or photocatalytic detoxification of industrial wastewater is currently the subject of research in many centers. As explained in the **Introduction**, the potential use of free solar radiation as the primary energy source in photocatalytic processes is an unquestionable advantage of this method. Unfortunately, the research for new photocatalysts active in visible radiation, which has been going on for years, has led to mediocre progress in this field. There is still a shortage of effective photocatalysts, especially for the photocatalytic decomposition of water. Here, under strictly anaerobic conditions, the quantum efficiency are very low. Therefore, work in many laboratories focuses on increasing the photocatalytic efficiency of the tested photocatalysts, preparing new photocatalysts, or designing hybrid systems. The section **Compendium of articles** describes the preparation of catalysts for the photocatalytic production of hydrogen. For this purpose, catalysts based on carbon materials (reduced graphene/activated carbon) and titanium dioxide doped with metal nanoparticles (Au/Pt) were prepared (Objective 1).

Also, the use of macroporous silicon microreactors to photogenerate hydrogen after coating the microchannels with Au/TiO_2 and Pt/TiO_2 photocatalysts was investigated (Objective 2).

The development of solar technologies for converting CO_2 into fuel has become a great energy challenge as it completes the anthropogenic carbon cycle and leads to the production of sustainable transport fuels on a global scale. However, the low mass conversion, poor selectivity, or low energy efficiency of the current approaches hinder their industrial application. The section **Annex** presents the thermochemical decomposition of CO_2 (an analogous process to water decomposition into hydrogen) on different shapes of cerium oxide catalyst doped with metals (Pt, Au, Ni, Ru, Pd). Moreover, the influence of the catalyst preparation method (ball milling vs. incipient wetness impregnation) has been studied (Objectives 3, 4 and 5). To better understand the functioning mechanism of the cerium oxide catalyst, molecular dynamics simulations with water molecules were performed (Objective 6). The **Conclusions** of this doctoral thesis are presented in the last chapter.

Overall, the specific objectives of this thesis are:

Objective 1: To synthesize and characterize titanium dioxide-carbon composites as photocatalysts to produce hydrogen from water/alcohol mixtures.

Objective 2: To explore the use of macroporous silicon structures to photogenerate hydrogen after coating the microchannels with Au/TiO_2 and Pt/TiO_2 photocatalysts.

Objective 3: To synthesize and characterize nanoshaped ceria exposing different crystallographic planes for thermochemical conversion of CO_2.

Objective 4: To study the influence of metal nanoparticles (Au, Ni, Pd, Pt, Ru) on nanoshaped ceria for thermochemical conversion of CO_2.

Objective 5: To study the influence of catalyst preparation methods using incipient wetness impregnation (IWI) and ball milling (BM).

Objective 6: To use molecular dynamics to study the interaction between H_2O molecules and ceria octahedral [111] facets with oxygen vacancies.

Resumen

Existen muchos métodos para producir hidrógeno a partir de fuentes fósiles no renovables, pero estos métodos tienen un impacto ambiental negativo a través de emisiones de contaminantes y/o gases de efecto invernadero. Por tanto, actualmente se están buscando métodos alternativos y respetuosos con el medio ambiente. Los dos métodos sostenibles principales para producir hidrógeno a partir de recursos renovables son los procesos fotocatalíticos y termocatalíticos. Este trabajo se centra en el estudio de estos procesos sobre TiO_2 y CeO_2, respectivamente.

Aunque el desarrollo de la investigación fotocatalítica con el uso de fotocatalizadores semiconductores no tiene más de unos 40 años, este campo de conocimiento está ganando cada vez más interés, tanto de la ciencia como de la industria. La descomposición fotocatalítica del agua o la desintoxicación fotocatalítica de las aguas residuales industriales es actualmente objeto de investigación en muchos centros. Como se explica en la **Introducción**, el potencial uso de la radiación solar como fuente de energía primaria en procesos fotocatalíticos es una ventaja incuestionable de este método. Desafortunadamente, la investigación de nuevos fotocatalizadores activos en radiación visible, que se ha estado realizando durante años, ha dado lugar a un progreso mediocre en este campo. Todavía hay escasez de fotocatalizadores eficaces, especialmente para la descomposición fotocatalítica del agua. En condiciones estrictamente anaeróbicas, los rendimientos cuánticos son muy bajos. Por lo tanto, el trabajo en muchos laboratorios se centra en aumentar la eficiencia fotocatalítica de los fotocatalizadores probados, preparar nuevos fotocatalizadores o diseñar sistemas híbridos. El **Compendio de artículos** describe la preparación de catalizadores para la

producción fotocatalítica de hidrógeno. Para ello, se prepararon catalizadores basados en materiales de carbono (grafeno reducido/carbón activado) y dióxido de titanio dopado con nanopartículas metálicas (Au/Pt) (**Objetivo 1**). Además, se investigó el uso de microrreactores de silicio macroporoso para fotogenerar hidrógeno después de recubrir los microcanales con fotocatalizadores de Au/TiO_2 y Pt/TiO_2 (**Objetivo 2**).

El desarrollo de tecnologías solares para convertir CO_2 en combustible se ha convertido en un gran desafío energético, ya que completa el ciclo antropogénico del carbono y conduce a la producción de combustibles de transporte sostenibles a escala mundial. Sin embargo, la conversión baja, la selectividad deficiente o la eficiencia energética baja de los enfoques actuales dificultan su aplicación industrial. La sección **Anexo** presenta la descomposición termoquímica de CO_2 (un proceso análogo a la descomposición del agua en hidrógeno) con diferentes formas de catalizador de óxido de cerio dopado con metales (Pt, Au, Ni, Ru, Pd). Además, se ha estudiado la influencia del método de preparación del catalizador (molienda de bolas vs. impregnación húmeda a sequedad incipiente) (**Objetivos 3, 4 y 5**). Para comprender mejor el mecanismo de funcionamiento del catalizador de óxido de cerio, se han realizado simulaciones de dinámica molecular de catalizadors immersos en con moléculas de agua (**Objetivo 6).** En el último capítulo explicaré las **Conclusiones** de esta tesis doctoral.

En general, los objetivos específicos de esta tesis son:

Objetivo 1: Sintetizar y caracterizar compuestos de dióxido de titanio-carbono como fotocatalizadores para producir hidrógeno a partir de mezclas de agua y alcohol.

Objetivo 2: Explorar el uso de estructuras macroporosas de silicio para fotogenerar hidrógeno después de recubrir los microcanales con fotocatalizadores de Au/TiO_2 y Pt/TiO_2.

Objetivo 3: Sintetizar y caracterizar ceria con nanoformas exponiendo diferentes planos cristalográficos para la conversión termoquímica de CO_2.

Objetivo 4: Estudiar la influencia de nanopartículas metálicas (Au, Ni, Pd, Pt, Ru) sobre ceria nanoformada para la conversión termoquímica de CO_2.

Objetivo 5: Estudiar la influencia de los métodos de preparación de catalizadores mediante impregnación húmeda a sequedad incipiente (IWI) y molienda de bolas (BM).

Objetivo 6: Utilizar la dinámica molecular para estudiar la interacción entre las moléculas de H_2O y las caras [111] de la ceria con vacantes de oxígeno.

Resum

Hi ha molts mètodes per produir hidrogen a partir de fonts fòssils no renovables, però aquests mètodes tenen un impacte ambiental negatiu a través d'emissions de contaminants i/o gasos d'efecte hivernacle. Per tant, es busquen mètodes alternatius i respectuosos amb el medi ambient. Els dos mètodes sostenibles principals per produir hidrogen a partir de recursos renovables són els processos fotocatalítics i termocatalítics. Aquest treball se centra en l'estudi d'aquests processos sobre TiO_2 i CeO_2, respectivament.

Tot i que el desenvolupament de la investigació fotocatalítica amb l'ús de fotocatalitzadors semiconductors no té més d'uns 40 anys, aquest camp de coneixement està guanyant cada cop més interès, tant de la ciència com de la indústria. La descomposició fotocatalítica de l'aigua o la desintoxicació fotocatalítica de les aigües residuals industrials és actualment objecte de recerca a molts centres. Com s'explica al **Introducció**, el potencial ús de la radiació solar com a font d'energia primària en processos fotocatalítics és un avantatge inqüestionable d'aquest mètode. Malauradament, la investigació de nous fotocatalitzadors actius en radiació visible, que s'ha fet durant anys, ha donat lloc a un progrés mediocre en aquest camp. Encara hi ha escassetat de fotocatalitzadors eficaços, especialment per a la descomposició fotocatalítica de l'aigua. En condicions estrictament anaeròbiques, els rendiments quàntics són molt baixos. Per tant, el treball a molts laboratoris se centra en augmentar l'eficiència fotocatalítica, preparar nous fotocatalitzadors o dissenyar sistemes híbrids. El **Compendi d'articles** descriu la preparació de catalitzadors per a la producció fotocatalítica d'hidrogen. Per això, s'han preparat catalitzadors basats en materials de

carboni (grafè reduït/carbó activat) i diòxid de titani dopat amb nanopartícules metàl·liques (Au/Pt) (**Objectiu 1**). A més, s'ha investigat l'ús de microreactors de silici macroporós per fotogenerar hidrogen després de recobrir els microcanals amb fotocatalitzadors d'Au/TiO_2 i Pt/TiO_2 (**Objectiu 2**).

El desenvolupament de tecnologies solars per convertir CO_2 en combustible ha esdevingut un gran desafiament energètic, ja que completa el cicle antropogènic del carboni i condueix a la producció de combustibles de transport sostenibles a escala mundial. Tanmateix, la conversió massa baixa, la selectivitat deficient o l'eficiència energètica baixa dels enfocaments actuals en dificulten l'aplicació industrial. L'apartat **Annex** presenta la descomposició termoquímica de CO_2 (un procés anàleg a la descomposició de l'aigua en hidrogen) en diferents formes de catalitzador d'òxid de ceri dopat amb metalls (Pt, Au, Ni, Ru, Pd). A més, s'ha estudiat la influència del mètode de preparació del catalitzador (mòlta de boles vs. impregnació humida a sequedat incipient) (**Objectius 3, 4 i 5**). Per comprendre millor el mecanisme de funcionament del catalitzador d'òxid de ceri, s'han realitzat simulacions de dinàmica molecular entre molècules d'aigua i la superfície de la cèria. (**Objectiu 6**). En el darrer capítol explicaré les **Conclusions** d'aquesta tesi doctoral.

En general, els objectius específics d'aquesta tesi són:

Objectiu 1: Sintetitzar i caracteritzar compostos de diòxid de titani-carboni com a fotocatalitzadors per produir hidrogen a partir de barreges d'aigua/alcohol.

Objectiu 2: Explorar l'ús d'estructures macroporoses de silici per fotogenerar hidrogen després de recobrir els microcanals amb fotocatalitzadors d'Au/TiO_2 i Pt/TiO_2.

Objectiu 3: Sintetitzar i caracteritzar cèria amb diferents formes exposant diferents plànols cristal·logràfics per a la conversió termoquímica de CO_2.

Objectiu 4: Estudiar la influència de nanopartícules metàl·liques (Au, Ni, Pd, Pt, Ru) a la cèria per a la conversió termoquímica de CO_2.

Objectiu 5: Estudiar la influència dels mètodes de preparació de catalitzadors mitjançant impregnació humida a sequedat incipient (IWI) i mòlta de boles (BM).

Objectiu 6: Utilitzar la dinàmica molecular per estudiar la interacció entre les molècules d'H_2O i les cares [111] de la cèria amb vacants d'oxigen.

Introduction

Introduction:

1. Global problems with gas emission and renewable energy

The development of civilization on our planet has long been associated with the use of mediocre resources, including mined energy resources. These raw materials have become the basis for world energy production, initially in the form of heat and later in the form of electricity. The industrial revolution that started in the 18th century used energy obtained from coal. Furthermore, at the turn of the 19th and 20th centuries, the use of crude oil allowed for the initiation of the development of the automotive industry, the development of which continues to this day. After the end of the II World War, natural gas began to be widely used as an energy raw material in the energy industry and the chemical industry.

In the second half of the twentieth century, along with the development of science, nuclear energy gained recognition. Perceived as highly prospective, it was at the same time treated as a kind of threat. One of the factors that contributed to such approach was undoubtedly the Chernobyl disaster. Nevertheless, scientists are still striving for new, safer, and cost-effective ways to produce energy.

In recent years, there has been an increasing emphasis on the use of clean energy from renewable sources [1]. Newer and newer technologies are being developed, ones which are more technically efficient and more economically profitable. At the same time, new problems are emerging regarding the use of renewable energy, such as the economics of obtaining this energy, the need to provide reserve sources based on conventional energy and the lack of substantial amounts when it comes to reducing greenhouse gas emissions through the use of renewable energy. One could speak of success if, by the middle of the 21st century, 30-35% of global energy production came from renewable energy.

In the 21st century, over 2 billion people still do not have access to energy, which constitutes a significant problem. The low level of technology in the areas affected does not allow the use of the opportunities offered by water, wind, or sun. People from these areas mainly use biomass energy, but it is impossible everywhere. There are areas on

Earth with a high biomass deficit, which is not only true for desert and steppe areas but also where the resources are insufficient and need to be imported from elsewhere.

The next global problem is the global influence of energy on the greenhouse effect. CO_2 emissions caused by burning fossils are the main contributor to the most discussed issue of the decade, with 35.2 Gt being emitted in 2017 [2]. Even though there have been substantial investments and a decrease in energy prices by renewables in the last few years, fossil fuels will continue to serve as an indispensable player in the global energy landscape[3]. Hence, it is expected that the relevance of fossil fuels in primary energy will continue to a significant extent in the near future. It is reported that one of the significant sources of carbon dioxide emissions is power plants, followed by the transportation sector.

In a recent report by International Energy Agency (IEA), the estimated global energy demand grew by 2.1% in 2017, twice the growth rate compared to the previous year. The demand of fossil fuels such as natural gas grew by an unprecedented value of 3% followed by oil which rose by 1.6%. It is also important to mention that the electricity demand increased by 3.1%. Even though renewables have seen the highest growth which accounted for 1/4th of global energy demand in 2017, overall 70% of global energy demand was met by fossil-based fuels, out of which natural gas share was 22% [4]. Therefore, the demand for hydrocarbons as primary fuel will continue to grow as shown in Figure 1. This will eventually lead to an increase in carbon dioxide emissions unless measures of fast transition are not adopted [5].

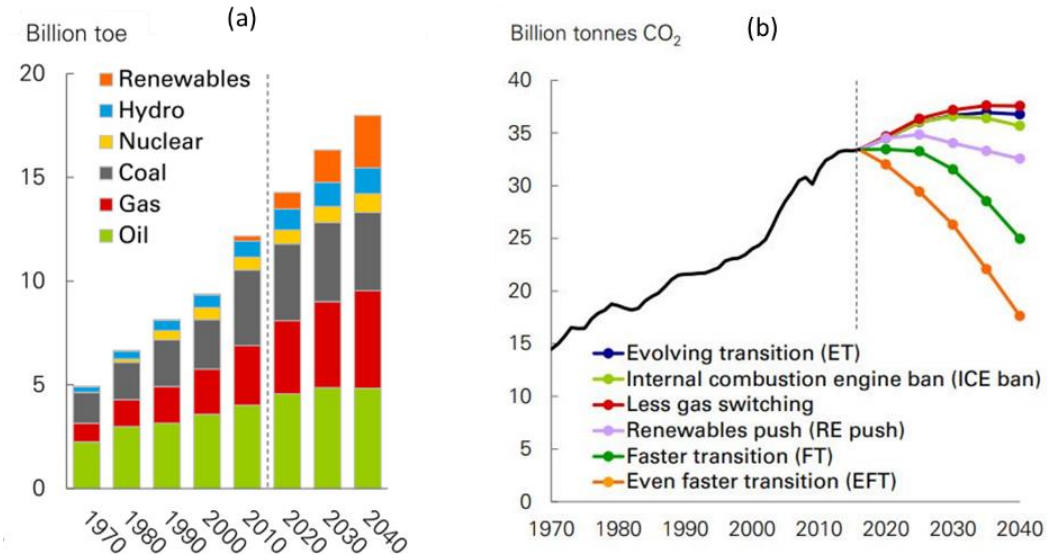

Figure 1. Primary energy sources (a); CO_2 emission forecast with different scenarios (b) [3].

In the recent report of the International Panel on Climate Change (IPCC), the goal of restricting the global warming rise of 2°C to 1.5°C by 2040 has been posted as mandatory, which paves the path for making a difference. This leads to a global call to make some stringent efforts to rewrite energy policies in order to reduce the usage of fossil fuels further [6], otherwise consequences will be irreversible in terms of ecological imbalance and environmental damage. Primarily apart from renewable energy based power production, there was an extensive drive for carbon capture and sequestration (CCS) based power plants and a call for retrofitting the existing power plants to adopt CCS. Adopting CCS based power generation systems would not solve the problem as the amount of CO_2 generated from them is so huge that it is not possible to store all of it in a depleted oil well or geological formations which also have safety implications in a long-term basis. Other alternatives such as the use of CO_2 in enhanced oil recovery also has limitations as the recovery rates are as low as 10% [7].

In this perspective, efforts to sequestrate CO_2 emissions should proceed together with a policy of re-utilization of the high amount of recovered CO_2. In terms of re-utilization, one possibility is to produce synthetic fuels from carbon dioxide emissions. Syngas is considered the target fuel because there is a large availability of CO_2 and H_2O from the

flue gases of carbon capture-based power plants, available for its production. Secondly, the syngas serves as the feedstock for multiple chemical productions such as methanol, dimethyl ether (DME), ethanol, to just name a few [8]. The downstream possibility of usage of syngas is shown in Figure 2. Currently, syngas is produced commercially using biomass, natural gas, and coal.. The natural gas to syngas by steam reforming, partial oxidation, autothermal reforming, and two-step reforming are the well-known technologies to produce syngas [9].

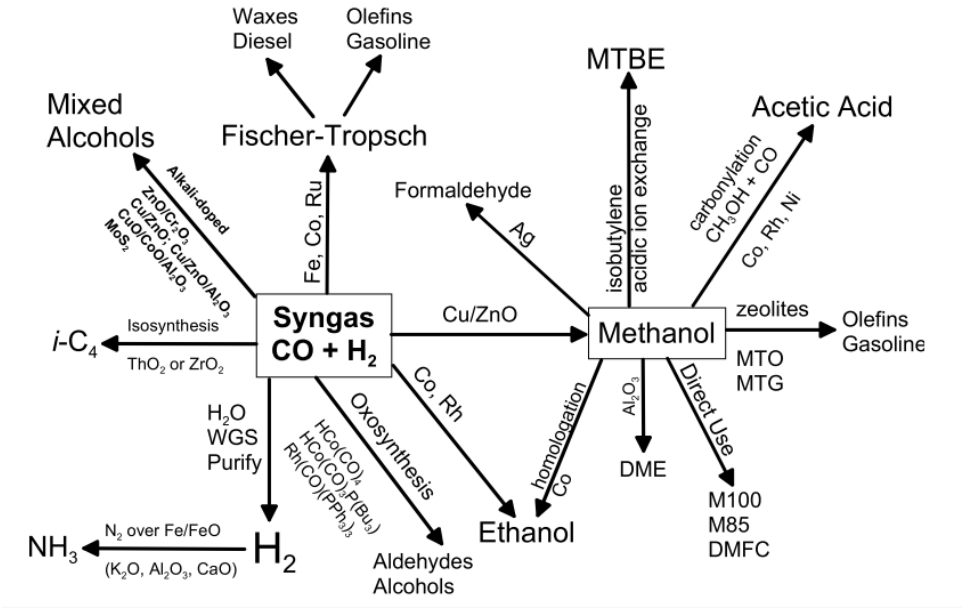

Figure 2. Syngas as feedstock for different chemical products [8].

Since the reforming reactions for syngas production are endothermic in nature and require external heat, their combination with solar energy is an attractive option to improve such processes [10]. What makes solar energy even more attractive to the production of fuels or chemicals, is the fact that solar energy is readily available almost everywhere. When a fuel (syngas, H_2, or any chemical based fuel) is produced by combining solar energy, it is termed solar fuel [11,12].

Conversion of solar energy and CO_2 by thermochemical processes to produce solar fuels was initially investigated to produce hydrogen as it was considered as the fuel of the future. Further processing can lead to the production of methanol, gasoline diesel, and kerosene, which are the liquid hydrocarbon feedstock for chemical processes,

contributing to a sustainable circular economy in the fuel and power industry as shown in Figure 3 [13]. Therefore, solar fuels considered as carbon neutral if they are produced from waste gas (a mixture of H_2O and CO_2), represent a viable way of storing intermittent renewable energy.

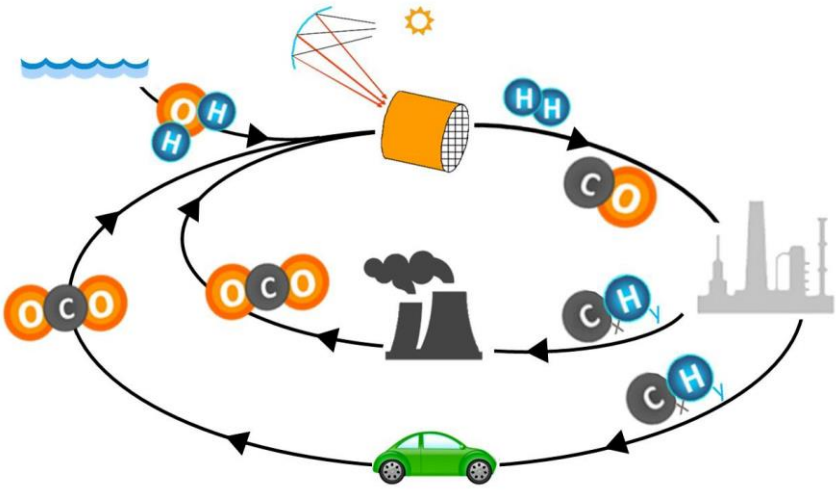

Figure 3. Circular economy by solar fuels from renewable energy. CO_2 and H_2O are captured from power plants and fed to a solar thermochemical process and converted to hydrocarbons in chemical plants [12].

Nowadays, the interest in engineering, the nanometric scale, the dimensions, morphology and the faces of individual particles are focused on controlling the surface chemistry of metallic nanomaterials or oxides, essential components in catalytic processes [14]. The catalytic processes allow to carry out chemical transformations more quickly and selectively towards the desired products, thus increasing the yield and reducing their cost. That is why catalysis's current objective is to develop and optimize new catalysts through an integral design of nanomaterials (structure, morphology, dimensions, chemical composition, etc.). To make a rational catalyst design, it is necessary to know very well their active centreses, which are the sites where chemical reactions really take place. It is essential to first understand the influence of the parameters that can alter the chemical response of these catalysts, such as the method of synthesis, pretreatments, etc. Nanomaterials have specific properties that are not expressed in bulk materials, such as a larger surface exposed by volume unit. In recent years the study for its application in catalysis has experienced unprecedented growth due to the development of advanced

characterization techniques and the combination of theory and experimental design in bottom up of heterogeneous catalysts.

The recent advances in the controlled synthesis and characterisation of materials on the nanoscale, in combination with the insights from developments in surface science over the past few decades, have resulted in a spectacular improvement in our understanding of how catalysis works on a molecular level and how catalysts can hence be rationally designed towards their desired functionality. It is frequently claimed that catalysis has always been a ‘nanoscience’. Although this statement is certainly true, it misses the crucial aspect that catalysts were more ‘accidental’ nanomaterials than rationally designed as such and it is this capability to rationally design functional materials – and catalysts in particular – that has recently allowed the transition of catalysis from a ‘black art’ to a science [15].

2. Hydrogen as a fuel for the future

Hydrogen is the cleanest energy carrier among all popular fuels available without polluting the natural environment.It is also important that hydrogen belongs to the most occurring of elements found in nature. In free form, it occurs only in volcanic gases and in the upper atmosphere. In addition to this, hydrogen occurs on Earth, the most important in chemical compounds, including water and organics, from which living organisms are built.

Paracelsus was the first to release hydrogen in the 17th century using acetic acid on iron and called it "plan air" when released. Then Henry Cavendish, an English chemist, in 1976, by treating metals with sulfuric acid, proved the existence of gas and proved that it is an independent substance and that the product of its combustion was water. However, he did not relate the fact that it is a component of water.

In 1898, the British J. Dewar liquefied and collected hydrogen. The shed's heat is around -252.2°C, while the transition to a solid-state takes place at -259.2°C. However, the first practical use of hydrogen dates back to 1783, when J. Charles launched a hydrogen-filled balloon in Paris for the first time.

Hydrogen has three naturally occurring isotopes denoted ^{1}H, ^{2}H, and ^{3}H. Hydrogen is the lightest element found in nature. It is colourless, odourless and tasteless. In the case of chemical properties, hydrogen is considered a unique element due to the ability to form compounds by donating or attaching an electron.

It is worth noting that hydrogen has a very high calorific value of 33.3 kWh/kg. Table 1 compares it to other types of fuel, and the highest value characterizes it.

Table 1. Calorific values of fuels.

Fuel	Calorific value [kWh/kg]
Hydrogen	33.3
Methane	13.9
Propane	12.9
Natural gas	12.2
Gasoline	12.0
Petroleum	11.6
Bituminous coal	7.7
Brown coal	5.6

In addition, hydrogen is a very active chemical and flammable. Burned in the atmosphere of the surrounding air, it only creates water and heat (see equation 1), which makes it the "cleanest fuel".

$$H_{2(gas)} + 1/2\ O_{2(gas)} \rightarrow H_2O_{(liquid)} + 286\ kJ\ mol^{-1}$$ Equation (1) [16]

It is predicted that hydrogen will become the fuel of the future, which will be an alternative to conventional non-infinite fuels. An important factor for hydrogen to replace current energy carriers is the development of cheap, fast, and efficient hydrogen production technology. Hydrogen is an energy carrier that can be made and transformed into energy in a variety of ways. It is worth paying attention to its advantages and disadvantages as a transport fuel, which are presented in Table 2 [17,18].

Table 2. Hydrogen as a transportation fuel: advantages vs. disadvantages.

Hydrogen as a transportation fuel	
Advantages	**Disadvantages**
Most abundant element	Not found free in nature
Produced from primary energy sources	Low ignition energy
Wide flammability range	Low density
High diffusivity	Currently expensive
Water vapor is a major oxidation product	
Most versatile fuel	
High energy yield	

Currently, there are several methods by which hydrogen can be produced. They are presented in Table 3.

Table 3. Methods of hydrogen production.

Method	**Process**	**Implementation**
Solar	Splitting of water using heat: $2H_2O_{(liquid)} \rightarrow 2H_{2\,(gas)} + O_{2(gas)}$	Not common use due to cost of renewable energy sources
Electrolysis of water	Electric current passed through water: $2H_2O_{(liquid)} \rightarrow 2H_{2\,(gas)} + O_{2(gas)}$	Not in widespread use due to cost of electricity
Steam reforming of methane gas	Reaction at high temperature: $CH_{4(gas)} + H_2O_{(gas)} \rightarrow CO_{(gas)} + 3H_{2(gas)}$ reaction at lower temperature: $CO_{(gas)} + H_2O_{(gas)} \rightarrow CO_{2(gas)} + H_{2(gas)}$	Current major source of hydrogen
Hydrogen from coal (gasification)	Reaction at high temperature: Coal+ $H_2O_{(gas)} + O_{2(gas)} \rightarrow$ syngas Reaction at lower temperature: Syngas= $H_2 + CO$	Current major source of hydrogen

The hydrogen production technology is developing very dynamically, but to achieve commercial success, researchers are trying to solve the most important problem of obtaining and storing hydrogen. Hydrogen as a source of automotive fuel is certainly promising as it would be environmentally-harmless. This idea is an object of interest and research both on the part of the automotive industry and the world of science [19].

3. Solar hydrogen production

The use of solar energy to produce hydrogen can be done by two processes: electrolysis of water using electricity generated by solar energy and direct solar splitting of water.

Direct separation of solar water refers to any process in which solar energy is directly used to produce hydrogen from water without going through an intermediate stage of electrolysis. Examples include:

- Photoelectrochemical water splitting - this technique uses semiconductor electrodes in a photoelectrochemical cell to convert light energy into hydrogen chemical energy. There are basically two types of photoelectrochemical systems - one that uses semiconductors or dyes, and the other uses dissolved metal complexes.
- Photocatalysis - is the process of initiating and accelerating a chemical reaction under the influence of light (UV, solar, infrared) in the presence of a catalyst.
- Photobiological - they rely on the production of hydrogen from biological systems with the help of sunlight. Under the right conditions, some algae and bacteria can produce hydrogen. The pigments in algae absorb energy from the sun, and the enzymes in the cell act as catalysts, splitting water into its hydrogen and oxygen components.
- High-temperature thermochemical cycles - these cycles use the Sun's heat to produce hydrogen by splitting water using thermochemical steps.

Recent studies have shown that H_2 production using sunlight-driven approaches is potentially competitive compared to traditional methods based on non-renewable resources [20,21, 22].

3.1. Photocatalytic method

Energy received from solar sources can be used in the process of photocatalysis and photoelectrochemical methods of hydrogen production. In photocatalytic hydrogen production, the photocatalyst particles prepared from the semiconductor material start to generate electrons and holes through an induced energy gap in the conduction and valence bands. These formed carriers drive the reduction and oxidation reactions. Alternatively, in photoelectrochemical hydrogen production, electrodes with a semiconductor coating can be placed in an electrolyte solution in an electrochemical cell, where the electrolyte solution carries the accepted electrons from the semiconductor electrode, while the Fermi level of the semiconductor material is lower than the reduction potential of the electrolyte [23]. The mechanism of the photocatalytic decomposition of water is shown in Figure 4. There are several pathways that electrons and holes can follow, the first two are related to charge transfer and the rest to recombination:

1. Semiconductor can donate electrons on the surface to reduce the electron acceptor (lane 1);

2. The hole may migrate to the surface to oxidize donor species (lane 2);

3. Recombination of electrons and holes can take place in the material (path 3) or on the surface (path 4). The last step is chemical reactions at the surface (redox reactions). General conditions process sequentially. In the first stage, the photocatalyst adsorbs radiation energy greater than its forbidden band to generate electron-hole pairs with potentials sufficient to decompose water. The second step is charge separation and migration to reaction sites on the surface.

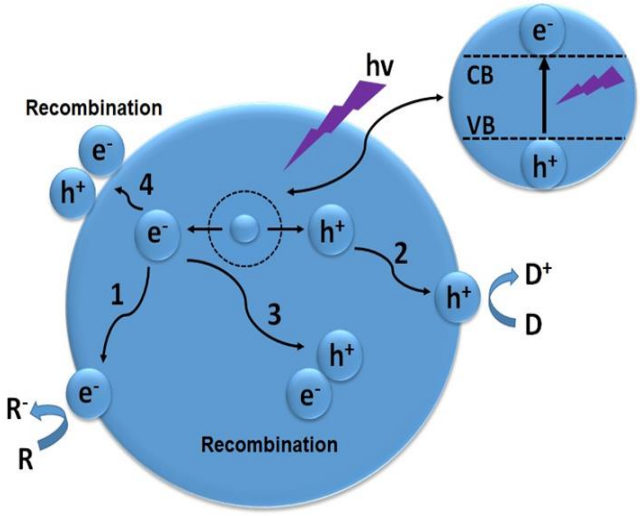

Figure 4. Schematic representation of processes related to photocatalytic generation, migration and recombination of electron-hole pairs [24].

The photocatalytic hydrogen production using semiconductor materials has attracted interest due to its high potential to produce pure hydrogen by splitting water using solar energy. In 1972, Fujishima and Honda [25] started a new trend in hydrogen production based on TiO_2 photocatalysts. Since then, research into several photoactive materials and their properties, characteristics, and applications for splitting water under UV light and visible light has gained attention and importance. Zamfirescu et al. [26] began comprehensive studies of several photoelectrochemical and photocatalytic systems. Acar et al. [27] selected photocatalysts based on TiO_2, which were compared in terms of the hydrogen production rate per unit area and per unit mass of the photocatalyst. On a weight basis, the highest hydrogen production rate was for Au-TiO_2 catalyst, with 7200 µmol H_2/h g. In turn, the hydrogen production rate calculated per area was highest for Au-CdS with 472.3 µmol H_2/h m^2, while Sb_2TiO_5 exhibited the lowest rate of 0.33 µmol H_2/h m^2. Ni et al. [28] reviewed the achievements of photocatalytic hydrogen production using TiO_2 and found that introducing dyes increases the activation of TiO_2 under UV light. Fujishima et al. [29] examined the surface-bound to TiO_2 and concluded that in addition to the natural properties of the sample, the method of preparation, handling, storage, chemical, and physical properties are all important for understanding the behaviour of the

material during the experiments. Moon et al. [30], using the sol-gel method to obtain boron-doped TiO_2 powders, found that the photocatalytic activity of TiO_2 increased by boron modification. Recently, much attention has been paid to semiconductor materials and carbon materials. Since the generation and transport of electrons are easier, the life of the generated electron-hole pairs is longer. Nguyen et al. [31] investigated the photocatalytic properties of TiO_2–carbon nanotubes nanohybrid materials and showed that the photocatalytic activity was better than those of pure TiO_2 and carbon nanotubes. There are many review articles on photoreactors and photocells for water separation as the design of the reactor is important for increasing efficiency.

3.2. Thermochemical cycles

Thermochemical solar cycles are becoming one of the possibilities of producing clean energy. The main disadvantages of solar water thermolysis justify the possibility of lowering the temperature. One option is to use metal oxides in thermochemical cycles. In this type of process, water is the main raw material, and the main products are oxygen and hydrogen [32] (Figure 5).

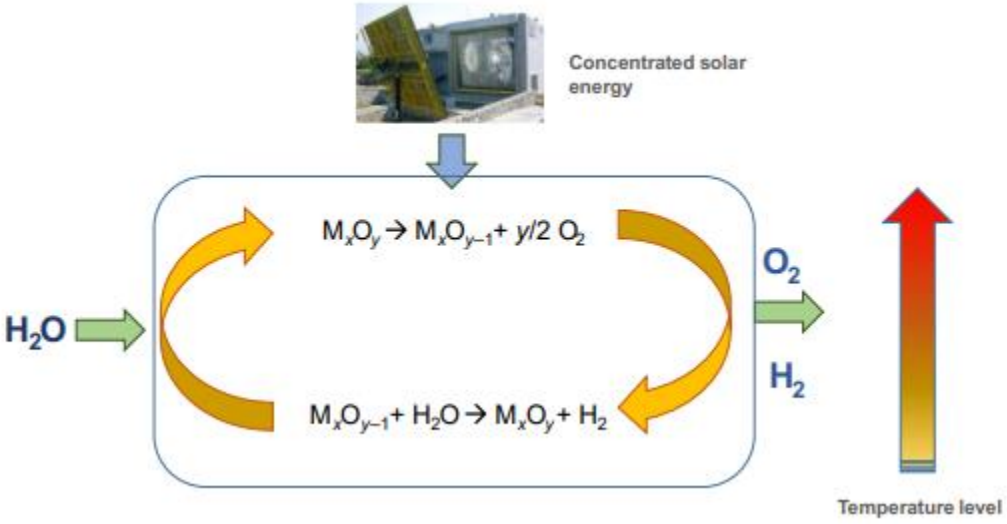

Figure 5. Diagram of a two-stage thermochemical solar cycle [33].

At the end of the 1960s, studies of thermochemical processes began with the results of the Energy Depot project. The main focus of this project was the production of fuels such as hydrogen, hydrazine and ammonia using waste heat from nuclear reactors as a source of energy. The results of the project were not satisfactory. Despite this, they continued research on hydrogen production using other energy sources, such as solar energy [34]. Nowadays, more than 350 thermochemical cycles have been studied for producing hydrogen with high efficiency [35]. There are two subcategories of cycles: the first is multi-stage and the second is two-stage. Thermochemical multi-stage cycles are solar processes that require three or more stages to obtain hydrogen, with a maximum temperature of around 900°C. Multistage cycles are rarely studied using solar energy due to the complexity of the process, which includes a large number of separation steps, difficulties in recovering materials and heat loss [32]. In contrast, two-stage thermochemical cycles of metal oxides are highly effective and simple, which make them meaningful for hydrogen production.

The first step in these cycles is the reduction of the metal oxide at high temperatures, where oxygen is released and the metal oxide is reduced to a lower valence state. The next stage is the process of producing hydrogen at low temperature, where the oxidation of previously reduced metals takes place by taking oxygen from the water. In this last step, the metal oxide is regenerated, establishing a cyclic process where the metal oxide is reused in the first step [36]:

$$M_xO_y \rightarrow M_xO_{y-1} + y/2\ O_2 \qquad \text{Equation (2)}$$

$$M_xO_{y-1} + H_2O \rightarrow M_xO_y + H_2 \qquad \text{Equation (3)}$$

As a result of metal oxide regeneration, the resultant reaction in this type of process is the splitting of water:

$$H_2O \rightarrow H_2 + ½\ O_2 \qquad \text{Equation (4)}$$

Two-stage thermochemical cycles can be divided into two categories, namely: non-volatile and volatile cycles. In the case of a non-volatile cycle, the reduced metal oxide remains in the solid phase and the reduction of materials is either stoichiometric or non-stoichiometric. In stoichiometric cycles, the crystal structure of the metal oxide changes,

while in non-stoichiometric cycles, the metal oxide is partially reduced. Otherwise, the volatile cycles show a transition from the solid phase to the gas phase of the reduced material because the reduction temperature is higher than the metal oxide evaporation temperature [37]. In recent years, a significant number of these cycles have been studied, and most research efforts have been focused on the study of the following redox pairs: Fe_3O_4 /FeO, ZnO/Zn, and especially CeO_2/Ce_2O_3 [38].

4. Titanium dioxide

There are several titanium minerals on Earth, among others rutile (TiO_2), ilmenite ($FeTiO_3$), titanite ($CaTiSiO_5$) and leucoxene ($CaTi(SiO_4)O$) [40]. One of the most popular semiconductors is titanium dioxide, which has found use in many industrial sectors. It has been used in the production of titanium white as an ingredient of paints or building materials. Along with the progress of research related to the activity of TiO_2 in UV and UV-Vis light, its use was also started due to its photocatalytic properties. One of the most interesting applications is the participation of TiO_2 in photocatalytic water remediation, photocatalytic hydrogen production, and in medicine in cancer therapies.

Titanium (IV) oxide has amphoteric properties. In reaction with concentrated sulfuric acid, it forms titanyl sulfate, while when fused with hydroxides, carbonates or other metal oxides, it turns into titanates. This compound is characterized by high mechanical strength, high photochemical stability and is practically insoluble. Three polymorphs of TiO_2 can be distinguished: anatase and rutile with a tetragonal structure, and brookite with a rhombic structure [39].

Under natural conditions, each of the titanium ions is bonded to the six oxygen ions that form the corners of the octahedron. The mutual arrangement of the octahedrons in the lattice of each polymorph is different, as shown in Figure 6 [43].

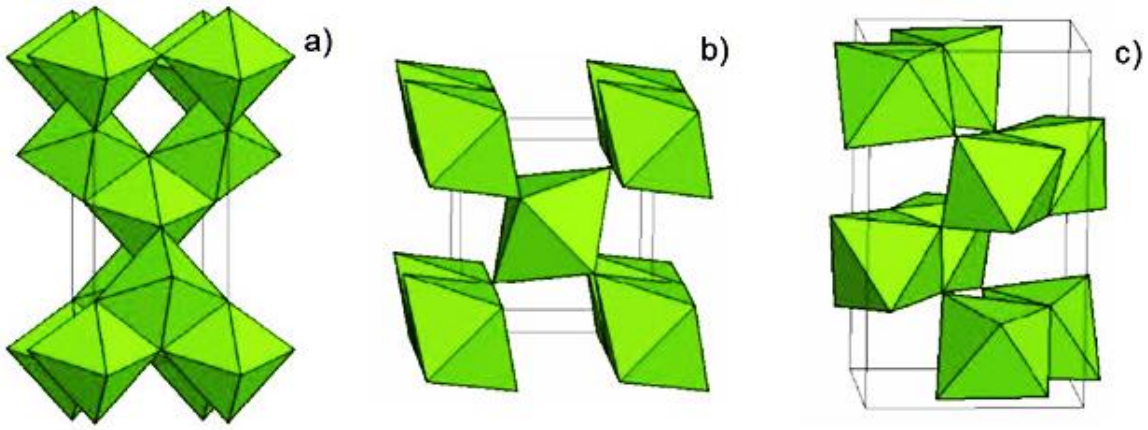

Figure 6. Diagram of the arrangement of titanium-oxygen octahedrons in anatase (a), rutile (b), and brookite (c).

Table 4. Physicochemical properties of polymorphs of titanium (IV) oxide.

Properties	Anatase	Rutile	Brookite
Crystallographic system	tetragonal	tetragonal	rhombic
Ti coordination number	6	6	6
Refractive index	2.554	2.616	2.700
Mohs hardness	5.5-6.0	6.0-6.5	5.5-6.0
Density [g/cm^3]	3.90	4.27	4.14
Bond length Ti-O [Å]	1.95	1.94	-
Thermal stability [°C]	400-800	>1500	>800
Band gap energy [eV]	3.26	3.02	2.96

TiO_2 belongs to the group of n-type semiconductors. The position of the valence band in the photocatalyst is similar for all forms of titanium dioxide. Different values of the band gap energy are related to the location of the lower edge of the conduction band, which occupies a different level for each polymorph [40]. Figure 7 shows the location of the bands for selected semiconductors [41].

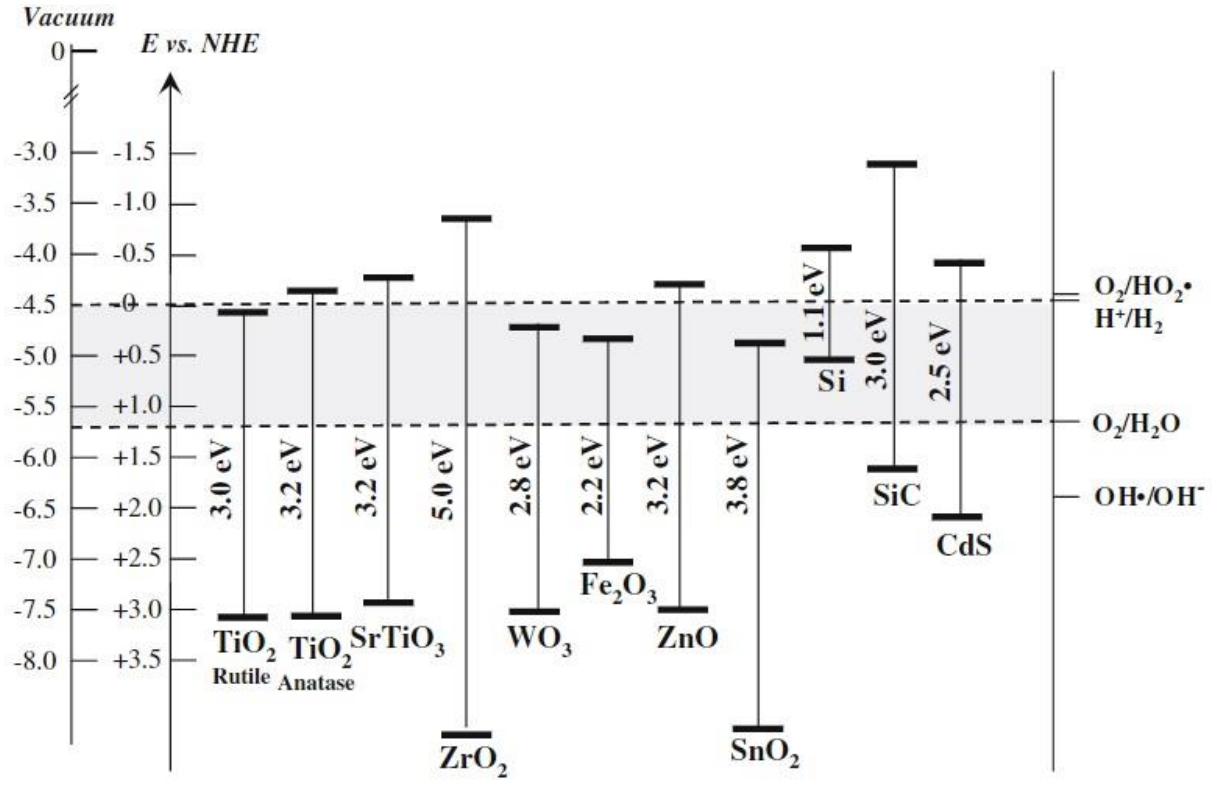

Figure 7. Location of the valence and conductivity bands for selected semiconductors. The energy scales are referenced against the vacuum level or the normal hydrogen electrode [42].

Long et al. [43] reported that the TiO_2 valence band is made of hybridized oxygen orbital (2p orbital) and titanium (3d orbital). The conduction band is primarily the titanium 3d orbital, while the share of oxygen 2p orbitals is only in the upper part of this band. Paxton and Thien-Nga [44] additionally found that, in the case of rutile, titanium 3d orbitals have an electronic configuration marked by distortions in the octahedral surrounding of the Ti^{4+} atom.

These authors also found that the change of conductivity from n to p is possible under high temperature conditions (> 1000°C) and high oxygen partial pressure. Lowering the oxygen partial pressure causes a significant increase in the concentration of oxygen vacancies, and thermodynamically stable Magnéli phases are formed [45].

The photocatalytic activity of TiO_2 is influenced not only by the type of polymorph, but also by physicochemical properties such as the degree of surface hydroxylation, the size and the type of pores, the specific surface area, the size and degree of agglomeration of the

photocatalyst particles, as well as the degree of crystallization and the number of defects in the crystal structure [46]. The efficiency of the photocatalysts is significantly influenced by the size of the energy gap, the rate of recombination of e^-–h+ pairs, and the number of hydroxyl groups on the TiO_2 surface.

Many researchers have proven that anatase has a much higher photoactivity compared to rutile [47,48]. Importantly, large specific surface areas usually result in the presence of many structural defects, resulting in fast recombination of pairs of charge carriers. The number of OH^- groups on the surface of the photocatalyst that trap the generated holes reduces the degree of recombination [41,49].

In the case of rutile, it has a much smaller number of active sites and a lower degree of surface hydroxylation [39] as well as faster recombination of electrons and holes. Inagaki et al. [47] and Grzechulska-Damszel et al. [50] found that the temperature of the transition from anatase to rutile had a significant effect on the reduction of the catalytic activity of rutile.

Basca et al. [51] and Ohno et al. [52, 53] investigated the mutual influence of both phases on the photoactivity of TiO_2. They stated that the photocatalysts with mixtures of anatase (70-75%) and rutile (30- 25%) showed much higher activity than pure anatase. They concluded that the high photocatalytic activity was due to a synergistic effect. This effect is often referred to in the case of the commercial titanium dioxide P25 (80% anatase, 20% rutile) which has been informally accepted as reference material. Ohtani [54] has a different opinion on this subject, claiming that the high photocatalytic activity of P25 has nothing to do with the synergistic effect, and the titanium dioxide P25 itself is a mixture of all three phases: anatase, rutile and amorphous.

The size of the active surface depends on several factors: the amount and particle size of the amorphous and crystalline phases and also the time and temperature at which the amorphous phase is obtained. To obtain titanium dioxide with a large specific surface area, it is recommended to use annealing/calcination temperatures in the range of 120–500°C and a short exposure time due to the possibility of grain sintering. Porter et al. [55] and Reddy et al. [56] stated that preparation at lower calcination temperatures has a beneficial effect on photocatalytic activity due to obtaining materials with a larger active

surface. Whereas Górska et al. [57] calcined and obtained TiO_2 in the temperature range 350–750°C. They proved that as a result of an increase in the calcination temperature, the specific surface area decreased, but the pore size increased. The materials calcined at the lowest temperatures used, ie, 350°C – 450°C, were characterized by the highest photocatalytic activity.

The size of the crystallites is important for photocatalytic activity. The smaller the crystallites the greater the specific surface area and the more active sites on the surface of the photocatalyst. The size of the crystallites influences the effect of the hypsochromic shift of the absorption band. This effect is related to the quantum effect in crystalline semiconductors, resulting in the effective band gap being broadened [45]. Mills et al. [58] found that the use of nanomaterials increases the oxidation-reduction potential of e^-- h+ pairs, because the migration path of charge carriers to the semiconductor surface will be shorter. Therefore, the amount of e^-- h+ pairs on the surface are greater, which significantly affects the photocatalytic efficiency. Inagaki et al. [47] found that as a result of an increase in calcination temperature, the size of crystallites also increases, while the number of structural defects decreases. In the low temperature range, the crystallite size changes, while for high temperatures the number of defects is so small that it does not significantly affect the particle size. Górska et al. [57] and Yu et al. [59], also investigated the effect of calcination temperature on the size of crystallites and the size of the specific surface area.

In order to improve the photocatalytic properties of TiO_2, various types of metals or non-metal ions are introduced into the oxide structure. The valence of the introduced ions significantly influences the activity of TiO_2. If they are metal ions with the same charge as the Ti ion in the crystal, the final effect is a change in the interactions between metal atoms. On the other hand, when TiO_2 was doped with Ce^{4+} ions, it was proved that the recombination of the charge carriers was faster, which reduced the photoactivity [60]. The introduction of metal ions into the structure of titanium dioxide with a valence lower than Ti^{4+} (Y^{3+}, La^{3+}, Nd^{3+}, Pd^{2+}) promotes the change in the gap size and the reduction of the concentration of point defects. It is then referred to as an acceptor impurity, which causes

the appearance of a new energy state near the edge of the photocatalyst's valence band. As a consequence, the process of recombination of e^-- h+ pairs is extended.

Nitrogen, boron, fluorine, phosphorus, iodine, sulfur and carbon are mentioned among the non-metals that improve the photoactivity of TiO_2, especially in the range of visible light [61,62, 63]. Titanium atoms can be replaced by atoms of another element, oxygen atoms or surface hydroxyl groups, as well as embedded internally in the TiO_2 structure. It is important that the modification of TiO_2 with non-metals may result in the appearance of new energy states and oxygen vacancies and a narrowing of the energy gap. Introducing carbon or phosphorus into the structure of titanium dioxide leads to the creation of new energy bands, which are located outside the TiO_2 band gap. The presence of another element in the structure of TiO_2 may have an impact on changes in its phase composition, increasing the temperature of the transition of anatase into rutile [47,64] or it may also affect the size of crystallites [64].

Recently, graphene has become one of the most frequently used materials in the process of obtaining nanocomposites due to its two-dimensional surface properties and highly developed specific surface. The high quality of graphene matrices enables electron transfer without charge scattering effect [65]. The titanium dioxide is deposited on the surface of the graphene matrices. As a result of direct contact, there is a mutual interaction between the d orbital in titanium dioxide and the π orbital in graphene, resulting in a new d-π bond between titanium dioxide and graphene. This causes the orbitals to overlap, causes a synergistic effect, and improves the activity of the nanocomposite [66] (Figure 8).

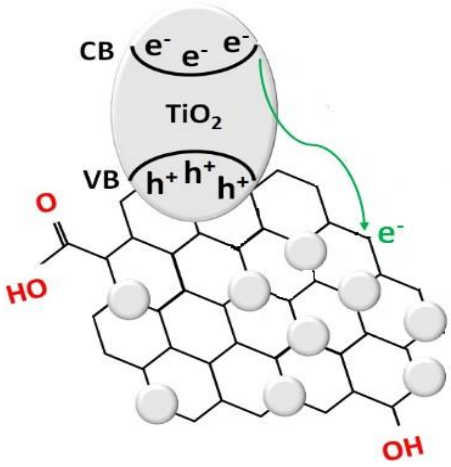

Figure 8. Scheme of the TiO_2-graphene nanocomposite.

There are many methods for creating composites based on titanium dioxide and graphene. Lambert et al. [67] obtained composites as a result of the TiF_4 hydrolysis process in the presence of graphene oxide. As a result, they obtained crystals of titanium dioxide (anatase) deposited on the graphene surface. Williams et al. [68] obtained nanocomposites by chemically oxidizing graphene to graphene oxide. In the presence of UV radiation and ethanol, the formed electron holes contributed to the formation of ethylene radicals, and the released electrons are accumulated in titanium dioxide particles. Then there is a reaction of free electrons with the plane of graphene oxide to reduce the appropriate functional groups, consequently leading to obtaining a reduced form of graphene oxide. Another method of obtaining composites is presented by Meng et al. [69] First, they prepared graphene sheets by oxidizing graphite using the Hummer method. They used the method of applying graphene coatings layer by layer and the titanium dioxide precursor in the form of tetraisopropanol. Finally, they obtained the nanocomposite titanium dioxide-graphene.

Composite materials containing TiO_2 and graphene may demonstrate increased photocatalytic activity due to very good mobility of electrons in the excited state, which hinders electron-hole recombination. There are many reports in the literature on various photocatalysts based on reduced graphene oxide (rGO) with TiO_2, CdS, WO_3, $BiVO_4$, ZnO [70,71,72,73,74,75,76]. Particular attention is paid to the graphene-TiO_2 nanocomposite.

Sun et al. [77] synthesized graphene/TiO_2 nanocomposites by simply covering the functionalized graphene with P25 nanoparticles by heterogeneous coagulation. Mou et al. [78] reported N-doped graphene (NGR) composite photocatalysts (NGR/TiO_2) for solar energy conversion. Liu et al. [79] develop a facile method to synthesize TiO_2–graphene composites with different exposed crystal facets for hydrogen production. Liu H., et al. [80] prepared RGO/TiO_2 nanocomposites which were synthesized by a straightforward procedure using $TiCl_3$ as both reducing agent to reduce graphene oxide (GO) and the precursor of TiO_2 for photocatalytic hydrogen production. The photocatalytic effect of reduced graphene oxide, despite many studies, is still the subject of debate because of the complexity of the rGO structure (hybridized atoms, variety of functional groups, defects, etc.).

The methods of titanium dioxide modification also include the use of activated carbon. The most common method of combining titanium dioxide and activated carbon is mechanical mixing. This preparation is a cheap method due to the lack of the use of complex equipment in the preparation of photocatalysts, and at the same time, it is not complicated. Moreover, the obtained composites are characterized by relatively high activity.

Lin et al. [81] prepared a composite based on titanium dioxide and carbon using the sol-gel method and found that coating titanium dioxide with a layer of carbon contributes to a significant improvement in the photocatalytic properties of the tested composites. Moreover, they proved that covering the surface of titanium dioxide with the use of carbon contributes to the use of visible radiation in the process of titanium dioxide activation, which was also confirmed by Yun et al. [82] examining composites prepared by impregnation.

The main advantage of covering the surface of titanium dioxide with carbon is inhibiting the transition of titanium dioxide from the anatase form to the rutile form. In addition, the advantages include the possibility of using radiation in the visible range in the TiO_2 excitation process due to the shift of the absorption maximum towards visible light [83], inhibition of the phase transition from anatase to rutile form as a result of increasing the

temperature of the transformation, and slowing down recombination of e^-- h+ pairs as a result of aeration of excited charges [84, 85].

5. Cerium dioxide

The recently high level of scientific research on cerium oxide emphasizes the importance of CeO_2 as a catalyst or catalyst carrier.

The crystalline structure of cerium oxide is cubic, with a face-centered cubic structure with a space group of Fm3m and a lattice constant of 5.410 Å (figure 9) [86]. Ceria is a member of the lanthanide group. It is one of the most abundant rare earth metals, about 0.0046% by mass present in the Earth's crust [87].

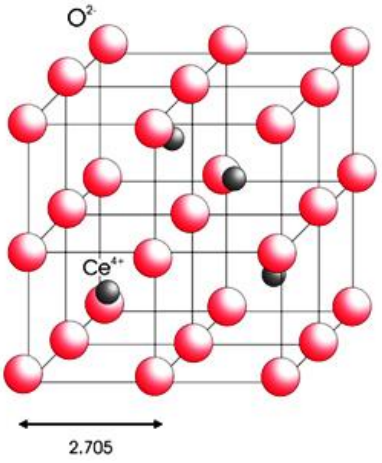

Figure 9. Cubic structure of cerium oxide [88].

Due to its characteristic redox properties, it is easy to transform between Ce^{4+}/Ce^{3+} (equation 5). Quick elimination or formation of oxygen vacancies is widely used in various industries (low-temperature water-gas shift (WGS), elimination of toxic automobile exhaust gases, etc. [89]).

$$CeO_2 \rightarrow CeO_{2-x} + \frac{x}{2} O_2 \qquad \text{Equation (5)}$$

Cerium oxide has the electronic configuration $4f^2 5d^0 6s^1$ and has two valence states: cerium (III) and cerium (IV). The catalytic activity of cerium dioxide is regulated by its

ability to absorb/release oxygen. This process depends on the temperature in the surrounding atmosphere and the partial pressure of oxygen

Cerium dioxide has three low-index crystallographic planes, namely (100), (110), and (111). Theoretical calculations showed that the most stable surface and the highest energy for oxygen vacancy formation is (111) [90]. The plane (110) is a stoichiometrically neutral plane in which the anions and cations are proportional and do not cause the formation of a dipole moment [91]. The least stable plane is (100), which results from superficial flaws that enable the compensation of charges [92].

In recent years, the study of various shapes of cerium oxide has gained importance. The atomic structure of different shapes of cerium oxide can be determined by electron microscopy. Figure 10 shows transmission electron microscopy (TEM) images of different shapes of cerium oxide [93].

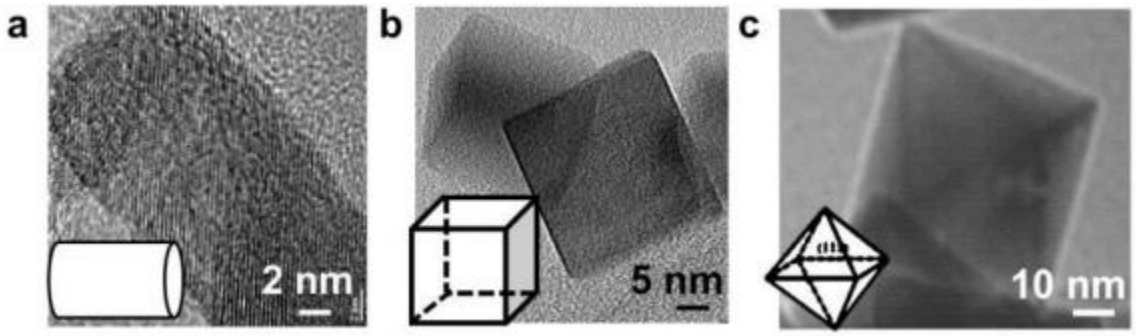

Figure 10. Typical TEM images of various morphologies of CeO_2 nanomaterials (a) rod, (b) cube, and (c) octahedron [92].

As previously mentioned, the structure of nanoctahedrons is the most stable of all. Then there is a cubic structure and finally the rods [94]. The shape plays an important role in lowering the reduction temperature. Thus, it is important to control the shape of the cerium oxide as well as to add metal nanoparticles for the sake of a combination of properties that can have the effect of lowering the reduction temperature to improve catalytic activity. Li et al. studied the improvement of catalytic efficiency using hydrothermal synthesis for CeO_2 rods [95]. In turn, Yan et al. obtained nanomaterials based on cerium oxide, in which its group was able to demonstrate that by using the principle of coordination chemistry, it

is possible to influence the morphology of metal oxides, as well as cerium oxide nanocrystals and to control parameters such as particle size, morphology, surface, texture [96, 97]. This proves that a series of active cerium oxide-based catalysts with the desired properties and controlled oxygen vacancies can be obtained.

In 2006, Abanades and Flamanta [98] studied cerium dioxide for the thermochemical splitting of water. In 2010, Chueh et al. [99] Used cerium dioxide as a material for solar thermochemical CO_2 splitting. From that moment on, studies of the cerium oxide for thermochemical cycles boosted [100].

The cycle for splitting CO_2 by cerium dioxide has two stages. The first step is the solar thermal reduction of CeO_2 in an inert atmosphere and low oxygen vapor pressure to obtain an oxygen-deficient non-stoichiometric cerium oxide. Then, a second step involves the non-solar oxidation of CeO_{2-x} back to CeO_2, which will take O_2 directly from H_2O/CO_2. The process is visualized in figure 11. Catalyst performance is determined by the temperature and the partial pressure of oxygen and also depends on the degree of non-stoichiometry. Cerium oxide, while maintaining its fluorite structure, is able to contain large amounts of non-stoichiometric oxygen [101].

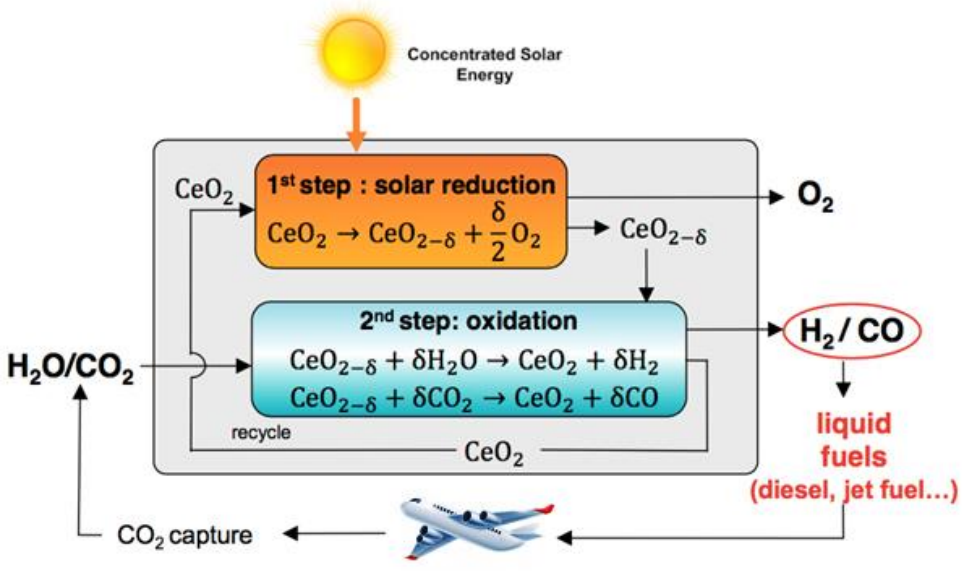

Figure 11. The two-step thermochemical redox process for the splitting of CO_2 using ceria [102].

6. Molecular dynamics as a tool to understand experimental results. Molecular dynamics: theory and methods

Molecular Dynamics is a method based on the atomic description of substances involved in the studied process. This means that all phenomena occurring in the described solids, liquids, or gases are modeled through molecular interactions. Due to this assumption, Molecular Dynamics is an intermediate method between quantum mechanics and mesoscopic methods that neglect the atomic structure of substances, binding atoms into larger, clustered sets [103].

Using Molecular Dynamics, to study the occurring phenomenon, one should create atomic models of substances and then describe the system's dynamics using the proposed interatomic interactions. The model of substance molecules means the determination ofthe data on the spatial arrangement of atoms, their masses, and the location and value of electric charges in the molecule. Depending on the studied process and the atomic form of the substance, when building a molecule model, we can use a simplified model that will contain the most important information about its structure; features important from the point of view of the studied case. . Due to the frequent lack of experimental data on the scale on which our research is conducted, the choice of the most important features is determined by the compliance of the behavior of the modeled substance with the experimental data on the macroscopic scale.

The most important step in the simulation of molecular dynamics is describing the atomic interactions of a molecular system, the so-called force field [104]. The force field is constructed to cover all relevant molecular interactions that will model molecular behaviour. In this case the Force-field was determined from the Morse potential into parameters consistent with Buckingham’s potential. The Lennard Jones potential was used for water molecules.

The next step in particle modeling using the Molecular Dynamics method is determining the interactions between individual atoms that make up their interaction. These interactions are divided into various types depending on the nature of the model under

study and the substances participating in it. The most commonly modeled types of inter-atomic forces are: electrostatic, van der Waals and chemical bonds.

To the particles, short-range van der Waals interatomic forces are used to describe the dynamics of the particle system. To describe these interactions, many types of potentials were created, e.g. Born-Mayer, Buckingham (figure 12), Morse potential or combinations of different potentials and their parameterization [105, 106].

In the presented work, the Buckingham potential, commonly used in numerical simulations, was used:

$$\varphi_{12}(r) = A\exp(-Br) - \frac{C}{r^6} \qquad \text{Equation (6)}$$

Here, *A*, *B* and *C* are constants. The two terms on the right-hand side constitute a repulsion and an attraction, because their first derivatives with respect to *r* are negative and positive, respectively [107].

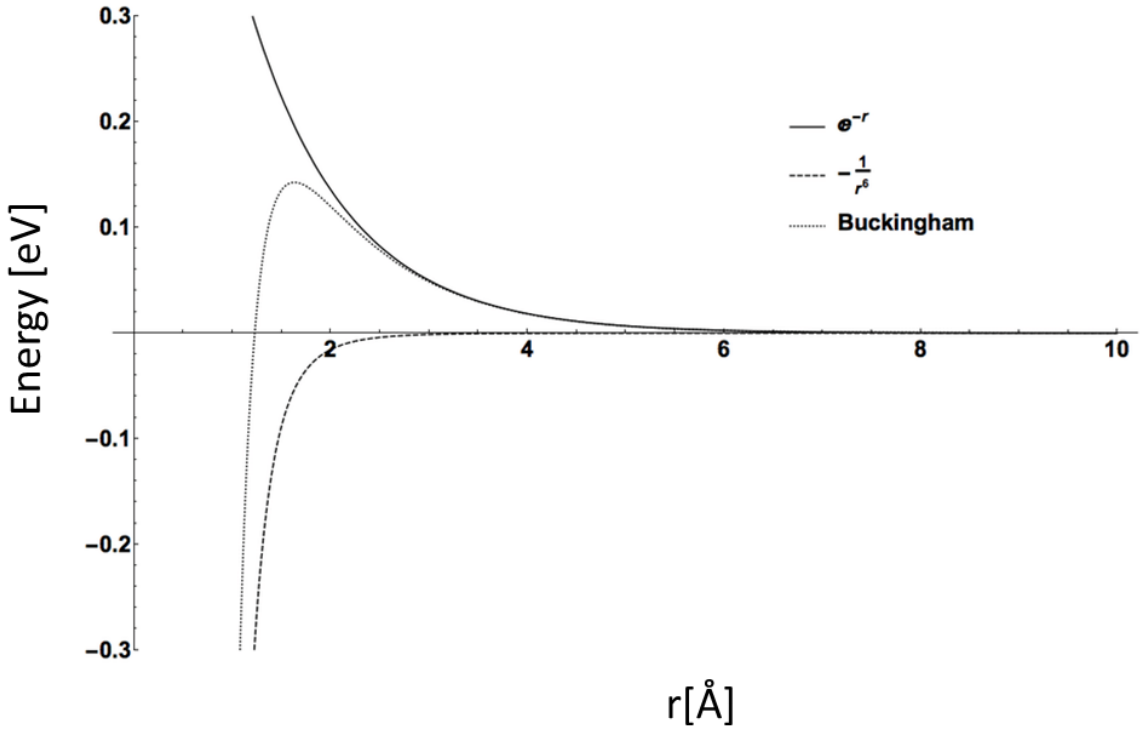

Figure 12. Exemplary plot of the Buckingham potential.

Molecular dynamics simulations calculate the movement of atoms in light of positions, velocities, forces and orientations over time. Thus, MD creates a series of configurations based on the initial configuration and speed. A set of numerical integration algorithms are used to calculate the equations of motion. This integration is done in a way that pressure, temperature or both can be kept constant. In the case of simulations carried out in this work, the temperature was 300 K and the pressure was 0.1 MPa and were checked to be constant in the time of 200 ns during all simulation time.

References

[1] Brendow K., Golbal and Regional Coal Demand Perspectives to 2030 and Beyond Sustainable Global Energy Development: The Case of Coal. Part I: Global Analysis. Chapter 6. WEC, London, 2004.

[2] I.E.A. IEA, Global Energy & CO2 Status Report 2017, 2018. https://www.iea.org/publications/freepublications/publication/GECO2017.pdf.

[3] C. Le Quéré, R.M. Andrew, P. Friedlingstein, S. Sitch, J. Hauck, J. Pongratz, P.A. Pickers, J.I. Korsbakken, G.P. Peters, J.G. Canadell, Global Carbon Budget 2018, Earth Syst. Sci. Data. 2018, 10 2141–2194. doi.org/10.5194/essd-10-2141-2018.

[4] I.E.A. IEA, Global Energy & CO2 Status Report 2017, 2018. https://www.iea.org/publications/freepublications/publication/GECO2017.pdf.

[5] BP Energy Economics, 2018 BP Energy Outlook 2018 BP Energy Outlook, 2018. doi.org/10.1088/1757-899X/342/1/012091.

[6] IPCC, IPCC special report on global warming of 1.5°C, 2019. https://www.ipcc.ch/sr15/

[7] G. Liu, J.A. Sorensen, J.R. Braunberger, R. Klenner, J. Ge, C.D. Gorecki, E.N. Steadman, J.A. Harju, CO2-Based Enhanced Oil Recovery from Unconventional Reservoirs: A Case Study of the Bakken Formation, SPE Unconv. Resour. Conf. 2014, 7. doi.org/10.2118/168979-MS.

[8] P.L. Spath, D.C. Dayton, Preliminary Screening -- Technical and Economic Assessment of Synthesis Gas to Fuels and Chemicals with Emphasis on the Potential for Biomass-Derived Syngas, 2003. doi.org/10.2172/15006100.

[9] D.R. Simbeck, A.D. Karp, R.L. Dickenson, Syngas production for gas-to-liquids applications: Technologies, issues and outlook. 1998. https://web.anl.gov/PCS/acsfuel/preprint archive/Files/Merge/Vol-45_1-0003.pdf.

[10] E.J. Sheu, E.M.A. Mokheimer, A.F. Ghoniem, A review of solar methane reforming systems, Int. J. Hydrogen Energy. 2015, 40, 12929–12955. doi.org/10.1016/j.ijhydene.2015.08.005.

[11] B. Bulfin, J. Vieten, C. Agrafiotis, M. Roeb, C. Sattler, Applications and limitations of two step metal oxide thermochemical redox cycles; A review, J. Mater. Chem. A. 2017, 5, 18951–18966. doi.org/10.1039/c7ta05025a.

[12] C. Graves, S.D. Ebbesen, M. Mogensen, K.S. Lackner, Sustainable hydrocarbon fuels by recycling CO2 and H2O with renewable or nuclear energy, Renew. Sustain. Energy Rev. 2011, 15, 1–23. doi.org/10.1016/j.rser.2010.07.014.

[13] A.G. Konstandopoulos, C. Pagkoura, D. Dimitrakis, S. Lorentzou, G. Karagiannakis, Solar hydrogen production, in: Prod. Hydrog. from Renew. Resour. 2015, 283–311. doi.org/10.1007/978-94-017-7330-0_10

[14] Z. Zhou, N. Tian, J. Li, I. Broadwell & S. Sun, ChemSoc Rev Nanomaterials of high surface energy with exceptional properties in catalysis and energy storage. Chem. Soc. Rev. 2011, 40, 4167–4185. doi.org/10.1039/C0CS00176G

[15] R. Schlögl, Theory in Heterogeneous Catalysis; an Experimentalist's View. Cattech, 2001, 5, 146–170. doi.org/10.1023/A:1014012505414

[16] N. Armaroli and V. Balzani, The Hydrogen Issue, ChemSusChem, 2011, 4, 21-36. doi.org/10.1002/cssc.201000182

[17] W. Dougherty, S. Kartha, C. Rajan, M. Lazarus, A. Bailie, B. Runkle, A. Fenel, Greenhouse gas reduction benefits and costs of a large-scale transition to hydrogen in the USA. Energy Policy 2008.

[18] Committee on Alternativees and Startegies for Future Hydrogen Production and Use, National research Council. The Hydrogen Economy: Opportunities, Costs, Barriers, and R&D Needs. Washington, D.C., The National Academy Press. 2004.

[19] N. A. Kelly, T.L. Gibson, D.B. Ouwerkerk, A solar-powered, high-efficiency hydrogen fueling system using high-pressure electrolysis of water: Design and initial results. Int. J. of Hydrogen Energy. 2008, 33, 2747-2764. doi.org/10.1016/j.ijhydene.2008.03.036

[20] A. Boretti, J. Nayfeh, A. Al-Maaitah, Hydrogen Production by Solar Thermochemical Water-Splitting Cycle via a Beam Down Concentrator, Front. Energy Res.,2021, doi.org/10.3389/fenrg.2021.666191

[21] M.A. Khan, I. Al-Shankiti, A. Ziani, H. Idriss, Demonstration of green hydrogen production using solar energy at 28% efficiency and evaluation of its economic viability, Sustainable Enery & Fuels, 2021, 4, doi.org/10.1039/D0SE01761B

[22] J. F. Wilson, S.S. Srinivasan, B.M. Moore, L. Henderson, Hydrogen Production Using Solar Energy, Journal of Undergraduate Research in Physis, 2013. doi.org/10.1051/e3sconf/20186100005

[23] H. Takashi, J. Kubota, K. Domen. Recent advances in semiconductors for photocatalytic and photoelectrochemical water splitting. Chemical Soc.Rev. 2014, 43, 7520-7535. doi.org/10.1039/C3CS60378D

[24] A. L. Linsebigler , G. Lu, J. T. Yates, Photocatalysis on TiO2 Surfaces Principles, Mechanisms, and Selected Results, Chem. Rev. 1995, 95, 735-758. doi.org/10.1021/cr00035a013

[25] A. Fujishima, H. Kenichi, "Electrochemical Photolysis of Water at a Semiconductor Electrode." Nature, 1972, 238.5358, 37–38. doi.org/10.1038/238037a0

[26] C. Zamfirescu, G. N. Naterer, I. Dincer. Solar Light–Based Hydrogen Production Systems. Encyclopedia of Energy Engineering and Technology-Four Volume Set. CRC Press, 2014, 1722-1744. ISBN 9781351237734

[27] A. Canan, I. Dincer, and G.F. Naterer. Review of photocatalytic water- splitting methods for sustainable hydrogen production. International Journal of Energy Research. 2016, 40, 1449-1473. doi.org/10.1002/er.3549

[28] Ni, Meng, et al. A review and recent developments in photocatalytic water splitting using TiO2 for hydrogen production. Renewable and Sustainable Energy Reviews. 2007, 11 401-425. doi.org/10.1016/j.rser.2005.01.009

[29] A. Fujishima, X. Zhang, D. A. Tryk. TiO2 photocatalysis and related surface phenomena. Surface science reports. 2008, 63, 515-582. doi.org/10.1016/j.surfrep.2008.10.001

[30] M. Sang-Chul, et al. Photocatalytic production of hydrogen from water using TiO2 and B/TiO2. Catalysis Today. 2000, 58, 125-132. doi.org/10.1016/S0920-5861(00)00247-9

[31] K. C. Nguyen, M. Phan Ngoc, M. Van Nguyen, Enhanced photocatalytic activity of nanohybrids TiO_2/CNTs materials. Materials Letters. 2016, 165, 247-251. doi.org/10.1016/j.matlet.2015.12.004

[32] S. Abanades, P. Charvin, G. Flamant, P. Neveu, Screening of water-splitting thermochemical cycles potentially attractive for hydrogen production by concentrated solar energy, Energy 2006, doi.org/10.1016/j.energy.2005.11.002.

[33] H.I. Villafán-Vidales, C.A. Arancibia-Bulnes, P.J. Valades-Pelayo, H. Romero-Paredes, A.K. Cuentas-Gallegos, C.E. Arreola-Ramos, Hydrogen from solar thermal energy. Solar Hydrogen Production. 2019, 319–363. doi:10.1016/b978-0-12-814853-2.00010-2

[34] J.E. Funk, Thermochemical hydrogen production: past and present, Int. J. Hydrogen Energy 2001, doi.org/10.1016/S0360-3199(00)00062-8.

[35] J.R. Scheffe, A. Steinfeld, Oxygen exchange materials for solar thermochemical splitting of H2O and CO2: a review, Mater. Today 2014, doi.org/10.1016/j.mattod.2014.04.025.

[36] C. Agrafiotis, M. Roeb, C. Sattler, A review on solar thermal syngas production via redox pair-based water/carbon dioxide splitting thermochemical cycles, Renew. Sustain. Energy Rev. 2015, doi.org/10.1016/j.rser.2014.09.039.

[37] R.J. Carrillo, J.R. Scheffe, Advances and trends in redox materials for solar thermochemical fuel production, Solar Energy 2017, doi.org/10.1016/j.solener.2017.05.032.

[38] B. Bulfin, J. Vieten, C. Agrafiotis, M. Roeb, C. Sattler, Applications and limitations of two step metal oxide thermochemical redox cycles; a review, J. Mater. Chem. A 2017, doi.org/10.1039/ C7TA05025A.

[39] J.M. Hermann, Heterogeneous photocatalysis: fundamentals and applications to the removal of various types of aqueous pollutants**,** Catal. Today, 1999, 53, 115-129. doi.org/10.1016/S0920-5861(99)00107-8

[40] S. Banerjee, J. Gopal, P. Muraleedharan, A.K. Tyagi,B. Raj, Physics and chemistry of photocatalytic titanium dioxide: visualization of bactericidal activity using atomic force microscopy**,** Current Sci. 2006, 90, 1378-1383.

[41] A.L. Linsebigler, G. Lu, J. Yates, Photocatalysis on TiO2 Surfaces: Principles, Mechanisms, and Selected Results, Chem. Rev., 1995, 95, 735-758. doi.org/10.1021/cr00035a013

[42] W. Choi, Pure and Modified TiO2 Photocatalysts and Their Environmental Applications, Catalysis Surveys from Asia 10(1), doi: 10.1007/s10563-006-9000-2

[43] M. Long, W. Cai, Z. Wang, G. Liu, First-principles calculation of N:H codoping effect on energy gap narrowing of TiO2,Appl. Phys. Lett. 2007, 90, 171909. https://doi.org/10.1063/1.2731707

[44] A.T. Paxton, L. Thien-Nga, Electronic structure of reduced titanium dioxide, Phys. Rev. B, 1998, 57, 1579. doi.org/10.1103/PhysRevB.57.1579

[45] T. Kasza, Badanie właściwości fotokatalitycznych i charakterystyka fizykochemiczna nanokrystalicznych filmów TiO2 na podłożu ceramicznym, Rozprawa doktorska, Kraków 2007

[46] O.O. Prieto-Mahaney, N. Murakami, R. Abe, B. Ohtani, Correlation between Photocatalytic Activities and Structural and Physical Properties of Titanium(IV) Oxide Powders, Chem. Lett. 2009, 38, 238. doi.org/10.1246/cl.2009.238

[47] M. Inagaki, R. Nonaka, B. Tryba, A.W. Morawski, Dependence of photocatalytic activity of anatase powders on their crystallinity, Chemosphere, 2006, 64, 437. doi.org/10.1016/j.chemosphere.2005.11.052

[48] Y.F. Li , Z.P. Liu, Particle Size, Shape and Activity for Photocatalysis on Titania Anatase Nanoparticles in Aqueous Surroundings**,** J. Am. Chem. Soc. 2011, 133, 15743. doi.org/10.1021/ja206153v

[49] M.R. Hoffmann, S.T. Martin, W. Choi, D.W. Bahnemann, Environmental Applications of Semiconductor Photocatalysis, Chem. Rev. 1995, 95, 69-96. doi.org/10.1021/cr00033a004

[50] J. Grzechulska-Damszel, A.W. Morawski, B. Grzmil, Thermally modified titania photocatalysts for phenol removal from water, Inter. J. Photoenergy 2006,1, 96398. doi.org/10.1155/IJP/2006/96398

[51] R.R. Basca, J. Kiwi, Effect of rutile phase on the photocatalytic properties of nanocrystalline titania during the degradation of p-coumaric acid, Appl. Catal. B 1998, 16, 19-29. doi.org/10.1016/S0926-3373(97)00058-1

[52] T. Ohno, K. Tokieda, S. Higashida, M. Matsumura, Synergism between rutile and anatase TiO2 particles in photocatalytic oxidation of naphthalene, Appl. Catal. A, 2003, 244, 383-391. doi.org/10.1246/cl.2003.364

[53] T. Ohno, K. Sarukawa, T. Tokieda, M.J. Matsumura, Morphology of a TiO_2 Photocatalyst (Degussa, P-25) Consisting of Anatase and Rutile Crystalline Phases, J. Catal. 2001, 203, 82-86. doi.org/10.1006/jcat.2001.3316

[54] B. Ohtani, O.O. Prieto-Mahaney, D. Li, R. Abe, What is Degussa (Evonik) P25? Crystalline composition analysis, reconstruction from isolated pure particles and photocatalytic activity test**,** J. Photochem. Photobiol. A, 2010, 216, 179-182. doi.org/10.1016/j.jphotochem.2010.07.024

[55] J. F. Porter, Y. Li, C.K. Cahn, The effect of calcination on the microstructural characteristics and photoreactivity of Degussa P-25 TiO2, J. Mater. Sci. 1999,34, 1523-1531. doi:10.1023/A:1004560129347

[56] K.M. Reddy, C.V.G. Reddy, S.V. Manorama, Preparation, characterization, and spectral studies on nanocrystalline anatase TiO2, J. Solid State Chem. 2001, 158, 180-186. doi.org/10.1006/jssc.2001.9090

[57] P. Górska, A. Zaleska, E. Kowalska, T. Klimczuk, J. Sobczak, E. Skwarek, W. Janusz, J. Hupla, TiO_2 photoactivity in vis and UV light: The influence of calcination temperature and surface properties, Appl. Catal B 84 (2008) 440-447. doi.org/10.1016/j.apcatb.2008.04.028

[58] A. Mills, S. Le Hunte, An overview of semiconductor photocatalysis, J. Photochem. Photobiol., A, 1997, 108, 1-35. doi.org/10.1016/S1010-6030(97)00118-4

[59] J. Yu, W. Wang, B. Cheng, B. Huang, X. Zhang, Preparation and photocatalytic activity of multi-modally macro/mesoporous titania, Res. Chem. Intermed. 2009, 35, 653-665. doi.org/10.1007/s11164-009-0107-8

[60] J. Lin, J.C. Yu, An investigation on photocatalytic activities of mixed TiO2-rare earth oxides for the oxidation of acetone in air, J. Photochem. Photobiol. A 1998,116, 63-67. doi.org/10.1016/S1010-6030(98)00289-5

[61] T. Ohno, T. Mitsui, M. Matsumura, Photocatalytic Activity of S-doped TiO_2 Photocatalyst under Visible Light, Chem. Lett. 2003, 32, 364. doi.org/10.1246/cl.2003.364

[62] A. Zaleska, J.W. Sobczak, E. Grabowska, J. Hupka, Preparation and photocatalytic activity of boron-modified TiO2 under UV and visible light, Appl. Catal. B, 2007, 78, 92-100. doi.org/10.1016/j.apcatb.2007.09.005

[63] L. Korosi, I. Dekany, Preparation and investigation of structural and photocatalytic properties of phosphate modified titanium dioxide, Colloids Surf. A, 2006, 280, 146. doi.org/10.1016/j.colsurfa.2006.01.052

[64] M. Janus, M. Inagaki, B. Tryba, M. Toyoda, A.W. Morawski, New preparation of a carbon-TiO2 photocatalyst by carbonization of n-hexane deposited on TiO2, Appl. Catal. B, 2006, 63, 272. doi.org/10.1016/j.apcatb.2004.03.011

[65] P. V. Kamat, Graphene-Based nanoarchitectures. Anchoring Semiconductor and Metal nanoparticles on a Two-Dimensional Carbon Support, J. Phys. Chem. Lett. 2010, 1, 2, 520-527. doi.org/10.1021/jz900265j

[66] D. Zhao, G. Sheng, C. Chen, X. Wang, Enhanced photocatalytic degradation of methylene blue under visible irradiation on grapehe-TiO2 dyade structure, Appl. Catal. B 2012, 303, 111-112. doi.org/10.1016/j.apcatb.2011.10.012

[67] T. N. Lambert, C. A. Chavez, B. Hernandez- Schanchez, P. Lu, N. S. Bell, A. Ambrosini, Synthesis and Characterization of Titania−Graphene Nanocomposites**,** J. Phys. Chem. C., 2009, 113, 19812-19823. doi.org/10.1021/jp905456f

[68] G. Williams, B. Seger, P.V. Kamat, TiO2-graphene nanocomposites. UV-assisted photocatalytic reduction of graphene oxide, ACS Nano, 2008, 2, 1487-1491. doi.org/10.1021/nn800251f

[69] X. Meng, D. Geng, J. Liu, R. Li, X. Sun, Controllable synthesis of graphene-based titanium dioxide nanocomposites by atomic layer deposition, Nanotechnology, 2011, 22, 165602. doi.org/10.1088/0957-4484/22/16/165602

[70] Q. Xiang, J. Yu, M. Jaroniec, Synergetic effect of MoS_2 and graphene as cocatalysts for enhanced photocatalytic H_2 production activity of TiO_2 nanoparticles. J. Am. Chem. Soc. 134 (2012) 6575–6578. doi.org/10.1021/ja302846n

[71] W. Fan, Q. Lai, Q. Zhang, Y. Wang, Nanocomposites of TiO_2 and reduced graphene oxide as efficient photocatalysts for hydrogen evolution. J. Phys. Chem. C, 115 (2011) 10694–10701. doi.org/10.1021/jp2008804

[72] Q. Xiang, J. Yu, M. Jaroniec, Graphene-based semiconductor photocatalysts, Chem. Soc. Rev., 41 (2012) 782–796, doi.org/10.1039/C1CS15172J

[73] M. Higashi, R. Abe, T. Takata, and K. Domen, Photocatalytic Overall Water Splitting under Visible Light Using $ATaO_2N$ (A = Ca, Sr, Ba) and WO_3in a IO_3^-/I^-Shuttle Redox Mediated System, Chem. Mater., 21 8 (2009) 1543-1549, doi.org/10.1021/cm803145n

[74] Y. Wang, W. Wang, H. Mao, Y. Lu, J. Lu, J. Huang, Z. Ye, B. Liu, Electrostatic self-assembly of $BiVO_4$-reduced graphene oxide nanocomposites for highly efficient visible light photocatalytic activities, ACS Appl. Mater. Inter. 6 (2014) 12698–12706, doi.org/10.1021/am502700p

[75] A. Iwase, Y. Ishiguro, A. Kudo, R. Amal, Reduced graphene oxide as a solid-state electron mediator in Z-scheme photocatalytic water splitting under visible light, J. Am. Chem. Soc., 133 (2011) 11054-11057, doi.org/10.1021/ja203296z

[76] M. J. Sampaio, C. G. Silva, R. R. N. Marques, A. M. T. Silva, and J. L. Faria, Carbon nanotube–TiO_2 thin films for photocatalytic applications, Catal. Today, 161 1 (2011) 91-96, doi.org/10.1016/j.cattod.2010.11.081

[77]S. Sun L. Gao, Y. Liu, Enhanced dye-sensitized solar cell using$grapheneeTiO_2$ photoanode prepared by heterogeneous coagulation, Appl Phys Lett., 96 (2010) 083113, doi.org/10.1063/1.3318466

[78] Z. Mou, Y. Wiu, J. Sun, P. Yang, Y. Du, Ch. Lu, TiO_2 Nanoparticles-functionalized N-doped graphene with superior interfacial contact and enhanced charge separation for photocatalytic hydrogen generation, ACS Appl. Mater. Inter., 6 (2014) 13798–13806, doi.org/10.1021/am503244w

[79] L. Liu, Z. Liu, A. Liu, X. Gu, Ch. Ge, F. Gao, L. Dong, Engineering the TiO_2-graphene interface to enhance photocatalytic H_2 production, ChemSusChem, 7 (2014) 618-626, doi.org/10.1002/cssc.201300941

[80] H. Li, X. Cui, A hydrothermal route for constructing reduced graphene oxide/TiO_2 nanocomposites: Enhanced photocatalytic activity for hydrogen evolution, Int. J. Hydrogen Energy 39 (2014) 19877–19886, doi.org/10.1016/j.ijhydene.2014.10.010

[81] L. Lin, W. Lin, Y.X. Zhu, B.Y Zao, Y. C. Xie, Y. He, Y.F. Zhu, Uniform carbon-covered titania and its photocatalytic property, J. Mol. Catal. A.: Chem., 2005, 236, 46-53. doi.org/10.1016/j.molcata.2005.04.028

[82] S.M. Yun, K. Palanivelu, Y. H. Kim, P.H. Kang, Y.S. Lee, Preparation and characterization of carbon covered TiO2 using sucrose for solar photodegradation, Ind. Eng. Chem., 2008, 14, 667-671. doi.org/10.1016/j.jiec.2008.02.010

[83] S. Sakthivel, H. Kisch, Daylight Photocatalysis by Carbon-Modified Titanium Dioxide, Angew. Chem. Int. Ed. 2003,42, 4908-4911. doi.org/10.1002/anie.200351577

[84] M. Anpo, Utilization of TiO_2 photocatalysts in green chemistry, Pure Appl. Chem., 2000, 72, 1265-1270. doi.org/10.1351/pac200072071265

[85] R. Leary, A. Westwood, Carbonaceous nanomaterials for the enhancement of TiO_2 photocatalysis**,** Carbon, 2011, 49, 741-772. doi.org/10.1016/j.carbon.2010.10.010

[86] C. Suryanarayana, Mechanical alloying and milling. Prog. Mater. Sci. 2001, 46,1, 1- 184. doi.org/10.1016/S0079-6425(99)00010-9

[87] G. Barcari, Metal. Nanoparticles and Nanoalloys; Wilcoxon, J., Johnston, R.L., Eds.; Elsevier: Amsterdam, The Netherland, 2012, 213–247.

[88] Development of Generalized KMC Code to Study Defect Mobility in Ceramic Materials towards Nuclear Fuel Applications, Aaron Oaks, Date: May 11, 2010.

[89] A.T. Bell, The impact of nanoscience on heterogeneous catalysis. Science, 2003, 299, 1688-1691. doi.org/10.1126/science.1083671

[90] J.P. Holgado, R. Alvarez, G. Munuera, Study of CeO2 XPS spectra by factor analysis: reduction of CeO2. Appl Surf Sci., 2000, 161, 3 and 4, 301-315. doi.org/10.1016/S0169-4332(99)00577-2

[91] C. Hu, Q. Zhu, L. Chen, R. Wu, CuO–CeO2 binary oxide nanoplates: Synthesis, characterization, and catalytic performance for benzene oxidation. Mater. Res. Bull., 2009, 44: 2174–2180. doi.org/10.1016/j.materresbull.2009.08.016

[92] G. Avgouropoulos, T. Ioannides, Effect of synthesis parameters on catalytic properties of CuO-CeO2. Appl. Catal. B Environ., 2006, 67, 1-11. doi.org/10.1016/j.apcatb.2006.04.005

[93] F. de Groot, A. Kotani, Core level spectroscopy of solids, CRC Press, Boca Raton, 2008, 147. ISBN 978-0-8493-9071-5.

[94] X. Sun, C. Gong, G. Lv, F. Bin, C. Song, C. Effect of Ce/Zr molar ratio on the performance of Cu–Cex–Zr1−x/TiO2 catalyst for selective catalytic reduction of NOx with NH3 in diesel exhaust. Mater. Res. Bull., 2014, 60, 341–347. doi.org/10.1016/j.materresbull.2014.09.014

[95] K. Zhou, X. Wang, X. Sun, Q. Peng, Y. Li, Enhanced catalytic activity of ceria nanorods from well-defined reactive crystal planes. J. Catal., 2005, 229, 206–212. doi.org/10.1016/j.jcat.2004.11.004

[96] R. Rangel, P. Bartolo-Pérez,E. Martínez, X.A. Trejo-Cruz, G. Díaz, D.H. Galván, Catalytic activity and X-ray photoelectron spectroscopy performance of Bi2MoxW(1−x)O6 solid-solutions. Catal. Sci. Technol., 2012, 2, 847-852. doi.org/10.1039/C2CY00506A

[97] J. Ch. Jung, H. Lee,H. Kim, Y.M. Chung, T.J. Kim, S.J. Lee, S.H. Oh, Y.S. Kim I.K. Song, Effect of Oxygen Capacity and Oxygen Mobility of Pure Bismuth Molybdate and Multicomponent Bismuth Molybdate on their Catalytic Performance in the Oxidative Dehydrogenation of *n*-Butene to 1,3-Butadiene, Catal. Lett. 2008, 124, 262–267. doi.org/10.1007/s10562-008-9450-4

[98] S. Abanades, G. Flamant, Thermochemical hydrogen production from a two-step solar-driven water-splitting cycle based on cerium oxides. *Solar Energy* 80, 2006, 1611–1623. doi.org/10.1016/j.solener.2005.12.00

[99] W.C. Chueh, S.M. Haile, A thermochemical study of ceria: exploiting an old material for new modes of energy conversion and CO_2 mitigation. *Phil. Trans. R. Soc. A*. 2010, 368, 3269–3294. doi.org/10.1098/rsta.2010.011

[100] R.R. Bhosale, G. Takalkar, P. Sutar, A. Kumar, F. al Momani, M. Khraisheh, A decade of ceria based solar thermochemical H_2O/CO_2 splitting cycle. *Int. J. Hydro. Energy* 2019, 44, 34–60. doi.org/10.1016/j.ijhydene.2018.04.080

[101] M. Mogensen, N.M. Sammes, G.A. Tompsett, Physical, chemical and electrochemical properties of pure and doped ceria. *Solid State Ionics*. 2000, 129, 63–94. doi.org/10.1016/S0167-2738(99)00318-5

[102] R. C. Pullar, R. M. Npvias, A. P.F. Caetano, M. A. Barreiros, S. Abanades, F. A. Costa Oliveira, A Review of Solar Thermochemical CO2 splitting using ceria-Based Ceramics With Designed Morphologies and Microstructures, Front. Chem, 2019, 7, 601. doi.org/10.3389/fchem.2019.00601.

[103] N. Formin, C. Fuentes, J.B. Saulnier, J.L. Tuhault, "Tissue blood flux monitoring by laser speckle photography" Laser Physics, 2001, 11,1-5.

[104] J.W. Ponder, D.A. Case, Force fields for protein simulations. Adv. Prot. Chem. 2003, 66:27-85. ISBN: 9780122673511.

[105] D. Frenkel, B. Smit "Understanding Molecular Simulation" Academic Press, 2002.

[106] M.P. Allen, D.J. Tildesley, "Computer simulation of liquids" Clarendon Press, Oxford, 1987. ISBN 0470-20812-0.

[107] R.A. Buckingham, The Classical Equation of State of Gaseous Helium, Neon and Argon. Proceedings of the Royal Society A: Mathematical, Physical and Engineering Sciences, 1938, 168(933), 264–283. doi.org/10.1098/rspa.1938.0173.

Compendium of articles:

1. J. Serafin, L. Soler, D. Vega, Á. Rodríguez, J. Llorca; ,,Macroporous silicon coated with M/TiO_2 (M= Au, Pt) as a highly efficient photoreactor for hydrogen production", Chemical Engineering Journal 2020, 393, 124701

2. J. Serafin, M. Ouzzine, J. Sreńscek-Nazzal, J. Llorca; ,,Photocatalytic hydrogen production from alcohol aqueous solutions over TiO_2-activated carbon composites decorated with Au and Pt'', Journal of Photochemistry and Photobiology A: Chemistry 2022, 425, 113726

3. J. Serafin, E. Kusiak-Nejman, A. Wanag, A.W. Morawski, J. Llorca; ,,Hydrogen photoproduction on TiO_2-reduced graphene oxide hybrid materials from water-ethanol mixture", Journal of Photochemistry and Photobiology A: Chemistry, 2021, 418, 113406

Chemical Engineering Journal 393 (2020) 124701

Contents lists available at ScienceDirect

Chemical Engineering Journal

journal homepage: www.elsevier.com/locate/cej

Macroporous silicon coated with M/TiO_2 (M = Au,Pt) as a highly efficient photoreactor for hydrogen production

Jarosław Serafin[a], Lluís Soler[a], Didac Vega[b], Ángel Rodríguez[b], Jordi Llorca[a,*]

[a] Institute of Energy Technologies, Department of Chemical Engineering and Barcelona Research Center in Multiscale Science and Engineering, Universitat Politècnica de Catalunya, EEBE, Eduard Maristany 10-14, 08019 Barcelona, Spain

[b] Department of Electronic Engineering, Universitat Politècnica de Catalunya, Jordi Girona 31, 08031 Barcelona, Spain

HIGHLIGHTS

- Macroporous silicon has been functionalized with M/TiO_2 photocatalysts.
- Outstanding hydrogen production rates of 212 μmol h^{-1} $cm^{-3}_{reactor}$ are obtained.
- High specific surface area per volume and enhanced light exploitation is reached.

GRAPHICAL ABSTRACT

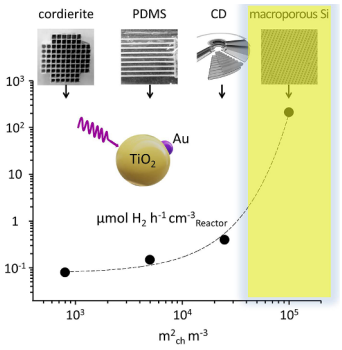

ARTICLE INFO

Keywords:
Hydrogen
Photocatalysis
Photoreactor
Microreactor
Macroporous silicon

ABSTRACT

Macroporous silicon disks containing ordered channels of 2 μm side and 0.2 mm length (9×10^6 channels cm^{-2}) have been functionalized with a thin layer of Au/TiO_2 and Pt/TiO_2 photocatalysts and tested in the photoproduction of hydrogen using UV light from water-ethanol mixtures in gas phase. An outstanding hydrogen production rate of 212 μmol h^{-1} $cm^{-3}_{reactor}$ is demonstrated, which is three orders of magnitude higher than those achieved in conventional photoreactors. According to the simulation results, the fabulous hydrogen production rates obtained with the macroporous silicon photocatalytic structures are ascribed to an extraordinary high specific surface area per volume unit and to an enhanced light exploitation. This new microphotoreactor concept could boost the production of solar hydrogen for on-site and portable applications.

1. Introduction

The photoproduction of hydrogen takes place under mild conditions and represents one of the most desired routes to obtain renewable hydrogen towards a more sustainable world [1–3]. However, the hydrogen photoproduction rates reported so far are too low for practical application and a strong effort is being pursued actively to develop more efficient photocatalysts and photocatalytic structures [4–9]. Whereas there is an impressive number of works related to the design of photocatalytic materials to increase the efficiency of the photoprocess, less attention has been paid to the proper design of photocatalytic devices [10–12]. Obviously, no matter how good a photocatalyst is, if a proper mass and photon transfer to the photocatalyst is not attained, the overall hydrogen yield will be strongly limited. Therefore, both the

* Corresponding author.
E-mail address: jordi.llorca@upc.edu (J. Llorca).

https://doi.org/10.1016/j.cej.2020.124701
Received 6 October 2019; Received in revised form 29 February 2020; Accepted 6 March 2020
Available online 07 March 2020

photocatalyst and the photoreactor are equally important to guarantee a suitable operation. Several solutions have been proposed to optimize both mass and photon transfer. Diminishing the distance between the photon source and the photocatalyst is a common strategy to increase efficiency. Also, the immobilization of the photocatalyst on a solid surface has been attempted as a possible solution to the light opacity limitation occurring in slurry photoreactors (as well as a facile separation of the photocatalyst from the reaction media), although this can aggravate mass transfer. So far, several solutions have been proposed to simultaneously enhance both mass and photon transfer in photoreactors aimed at producing hydrogen under dynamic conditions. Taboada et al. introduced optical fibers inside the channels of a cordierite monolith coated with a photocatalyst and substantially increased the photoproduction rate of hydrogen with respect to conventional slurry photoreators [13]. Castedo et al. developed planar photoreactors with silicone channels coated with a photocatalyst by additive manufacturing tools and tested them in the photogeneration of hydrogen under UV and under direct exposure to sunlight, obtaining promising results to achieve effective numbering up while keeping manufacturing costs low [14,15]. In an attempt at miniaturization, Sans et al. coated the grooves of a commercial compact disk (CD) with a photocatalyst by an electrophoretic method and built a photonanoreactor, which showed an extraordinary hydrogen photoproduction rates on a volume basis [16]. As a new turn of the screw, here we have explored the use of macroporous silicon to photogenerate hydrogen after coating the microchannels with Au/TiO_2 and Pt/TiO_2 photocatalysts. The small dimensions of the microchannels (2 μm) and their large aspect ratio (length/side = 100) facilitate mass transfer, while the optical properties of macroporous silicon enhance the exploitation of light. With this new type of photoreactor device we open the possibility of producing solar hydrogen at the microscale for small applications.

2. Materials and methods

2.1. Macroporous silicon preparation

Photoassisted electrochemical etching [17] was used to prepare silicon micromonoliths with straight, parallel channels of 2 μm side over ⟨1 0 0⟩ n-type float-zone silicon. Before electrochemical etching, silicon was first pre-structured by lithography and tetramethylammonium hydroxide was used to create a square array of inverted pyramids toward the bulk of the Si wafer and defined the positions of pore growth. The electrochemical etching was carried out at 288 K in HF solution, using TritonX-100 surfactant as a wetting agent, at a constant potential of 2 V. The backside of the Si wafer was illuminated through an array of LEDs with an 880 nm peak emission wavelength. A schematic representation of the process is shown in Fig. 1. After the electrochemical etching, the sample was oxidized in O_2 at 1373 K for 30 min. The oxide layer on the backside was removed, and the remaining backside silicon was etched off in tetramethylammonium hydroxide at 358 K until the pore tips were reached. The resulting structures were silicon micromonoliths with pores (channels) of 2 μm side opened at both sides and arranged in a square lattice with a periodicity of 4 μm.

2.2. Photocatalyst preparation

The microchannels of the macroporous silicon structures were coated with TiO_2 following literature methods [18–20]. Briefly, the macroporous silicon was first oxidized under dry oxygen at 1373 K for 30 min to develop a thin layer of SiO_2 at the surface of the microchannels. This is the blank sample in this work and it is labeled as SiO_2/Si. Then, titanium(IV) isopropoxide (Alfa Aesar) was forced to pass through the microchannels of the macroporous silicon structure by applying a pressure difference of ca. 75 kPa under an Ar atmosphere. With this method, the hydroxyl groups of SiO_2 reacted with the titanium precursor to form surface titanium alkoxide groups, which were subsequently calcined at 723 K (1 K min^{-1}) for 4 h to form a compact TiO_2 layer over SiO_2 [20]. This sample is labeled as TiO_2/SiO_2/Si.

The TiO_2/SiO_2/Si structure was decorated separately with Au and Pt. Preformed Au nanoparticles encapsulated with dodecanethiol monolayer shells and suspended in toluene (4.4 mg_{Au} mL^{-1}) were used to decorate TiO_2 with gold, whereas an aqueous solution of $(NH_3)_4Pt(NO_3)_2$ (0.5 M) was used to decorate TiO_2 with platinum. Gold nanoparticles were synthesized according to the two-phase Brust method [21] and measured 2.2 ± 0.3 nm as prepared [22]. 150 μL of the metal suspension (Au nanoparticles) or metal solution ($[(NH_3)_4Pt]^{2+}$) were forced to pass through the microchannels of the macroporous silicon coated with TiO_2 by applying a pressure difference of ca. 75 kPa. The resulting photocatalytic structures were calcined at 673 K (2 K min^{-1}) for 2 h. In the case of Au decoration, this treatment eliminated the dodecanethiol shell and assured a strong contact between Au and the TiO_2 support, as reported previously [23]. The sample doped with Pt was activated under hydrogen (10% H_2 in Ar) at 673 K (2 K min^{-1}) for 4 h as reported elsewhere [24] to attain a strong interaction between Pt and the TiO_2 support. These photocatalytic structures are labeled as Au/TiO_2/SiO_2/Si and Pt/TiO_2/SiO_2/Si. A postmortem chemical analysis by ICP indicated that the Au and Pt loadings were 0.91 wt% Au and 0.77 wt% Pt with respect to TiO_2.

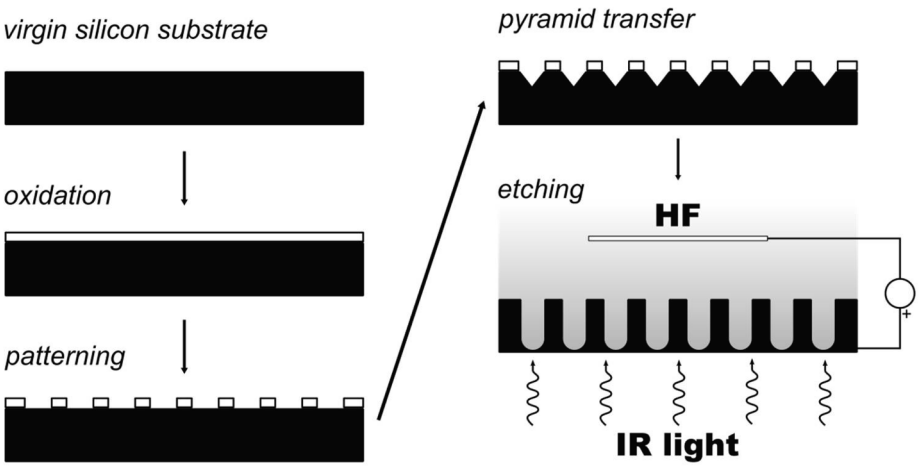

Fig. 1. Scheme of the method used for the preparation of the macroporous silicon structures.

2.3. Characterization

Field Emission Scanning Electron Microscopy (FESEM) images were recorded at 5 kV using a Zeiss Neon40 Crossbeam Station instrument equipped with a field emission source. Raman spectroscopy was performed over the range of 50 to 800 cm^{-1} on a Renishaw inVia Qontor confocal Raman microscope using a laser excitation source of 532 nm directed through a Leica DM2700 M microscope to the sample after which the scattered light is collected and directed to a spectrometer with a 2400 lines mm^{-1} grating with a resolution of 1 cm^{-1}. The metal content of the samples was determined by Inductively Coupled Plasma-Optical Emission Spectrometry (ICP-OES) using a Perkin Elmer Optima 3200RL instrument.

2.4. Photocatalytic tests

The photocatalytic tests were performed at 25, 40 and 60 °C and atmospheric pressure in a tubular glass photoreactor [25,26]. Ethanol was either synthetic (PanReac Applichem) or commercial bioethanol (Bioetanol de la Mancha, S.L.; 5 ppm S, 1 ppm Cl, 0.4 ppm P). An argon stream was bubbled through a Drechsel bottle containing a liquid mixture of ethanol-water in order to obtain a gaseous reactant mixture of EtOH:H_2O = 1:10 (molar), which was directly introduced in the photoreactor and forced to pass through the channels of the photocatalytic macroporous silicon structure. The temperature was monitored with a K-type thermocouple in direct contact with the macroporous silicon disks. An UV-light source (from SACOPA, S.A.U.) consisting of four LEDs emitting at 365 ± 5 nm was aligned to a synthetic quartz glass cylindrical lens to transmit the light to the sample. An irradiance of 80 mW cm^{-2} at the position of the sample was measured with a UVA sensor (model PMA 2110, Solar Light Co.), which registers the UV radiation within a spectral response of 320–400 nm, connected to a radiometer (model PMA2200, Solar Light Co.). The outlet of the photoreactor was connected to a micro gas chromatograph (Varian CP-4900) equipped with MS 5 Å, Plot U and Stabilwax columns for a complete analysis of the photoreaction products, which were monitored on-line every 4 min. Photocatalytic tests were conducted initially over the Au/TiO_2/SiO_2/Si sample at gas hourly space velocity (GHSV) values between 50,000 and 400,000 h^{-1} and no mass transfer limitations were observed. Therefore, a GHSV = 100,000 h^{-1} (0.036 s contact time) was selected to carry out the photocatalytic tests.

2.5. Modeling

It should be noted that macroporous silicon absorbs and scatters light differently according to the pore geometry. Simulations of different macroporous silicon structures were performed considering the simplified geometry shown in Fig. 2, which consists of a single pore coated with a silicon dioxide layer on top of which a layer of titanium dioxide is deposited. The pore is embedded in a silicon substrate and in vacuum ($\varepsilon_{air} \approx \varepsilon_0 = 1$) for the electromagnetic simulations. The beginning of the pore has a tapered section to take into account the inverted pyramid nucleation points present in the fabricated samples.

Table 1
Volume fraction (unitless) for different simulated macroporous structures.

Periodicity (nm)	Pore diameter (nm)	SiO_2 thickness (nm)	TiO_2 thickness (nm)				
			50	100	150	200	300
700	500	50	0.127	0.222	–	0.315	–
		100	0.110	0.187	0.233	–	–
2000	1500	50	0.055	0.106	–	0.196	0.270
		100	0.053	0.101	–	0.187	0.257
4000	2000	50	0.019	0.036	–	0.069	0.097
		100	0.018	0.035	–	0.066	0.094

3. Results and discussion

3.1. Modeling

Several geometrical variations were considered to study and optimize light absorption and, consequently, reaction efficiency. Table 1 summarizes the geometries considered and their corresponding volume fraction. The volume fraction (VF) is defined as the volume ratio of the occupied volume of TiO_2 with respect to the unitary cell volume and it is calculated based on geometrical constrains and taking into account that the thermally grown silicon oxide consumes 46% of its thickness from the silicon substrate: $VF = \pi t_{TiO_2}(D_{pore} - 2t_{SiO_2}[1 - 0.46] - t_{TiO_2})/a^2$, where a is the macroporous silicon periodicity, D_{pore} is the pore diameter, t_{SiO_2} is the silicon oxide layer thickness, and t_{TiO_2} is the titanium oxide layer thickness.

The simulations modelled the initial 6 μm of the pores due to computational constraints, but the data collected was enough to obtain the electrical field strength profile along the pore and to obtain the light reflectance and transmittance coefficients for each geometry (Fig. 3). Periodical boundary conditions were used on the +XZ −XZ +YZ and −YZ external planes of the simulation cell (plane orientation is shown in Fig. 2). The excitation was a planar wave propagated along the +Z direction with a Gaussian temporal pulse centered at λ_0 = 365nm. SiO_2 was found to be lossless at the work wavelength while losses were taken into account for the silicon substrate and the TiO_2 layer. The values used were $n_{SiO_2} = 1.475$, $n_{TiO_2} = 2.879 - j0.01769$, and $n_{Si} = 6.367 - j2.527$, where n_x is the complex refractive index of material x at the central wavelength λ_0, and j is the imaginary unit.

From the transmitted intensity data shown in Fig. 3 (the non-shadowed region), a parabolic function was used as the absorption factor in the well-known Beer-Lambert law to fit the profiles: $I = I_0\exp(a_0 + a_1 l + a_2 l^2)$. The parameter of interest is the linear term a_1 as it represents the expected absorption behaviour for large depths. This

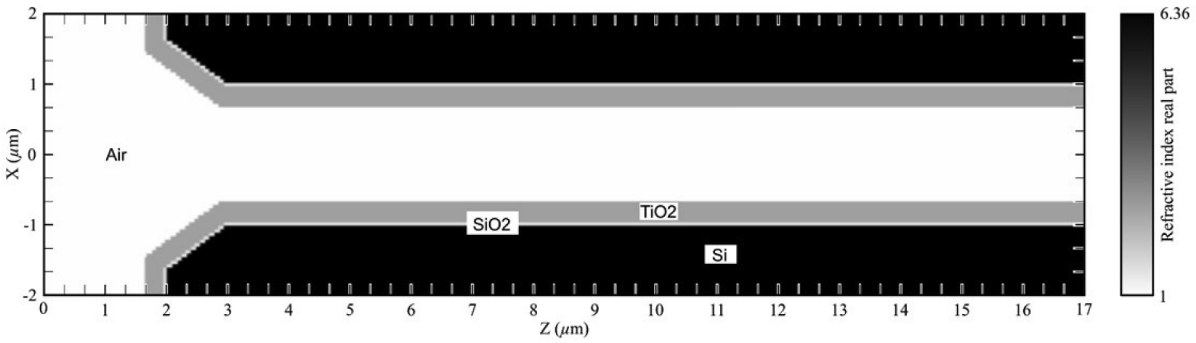

Fig. 2. Theoretical model cross section of the macroporous silicon structure. Dimensions are in microns, the color scale is the real part of the refractive index of the material.

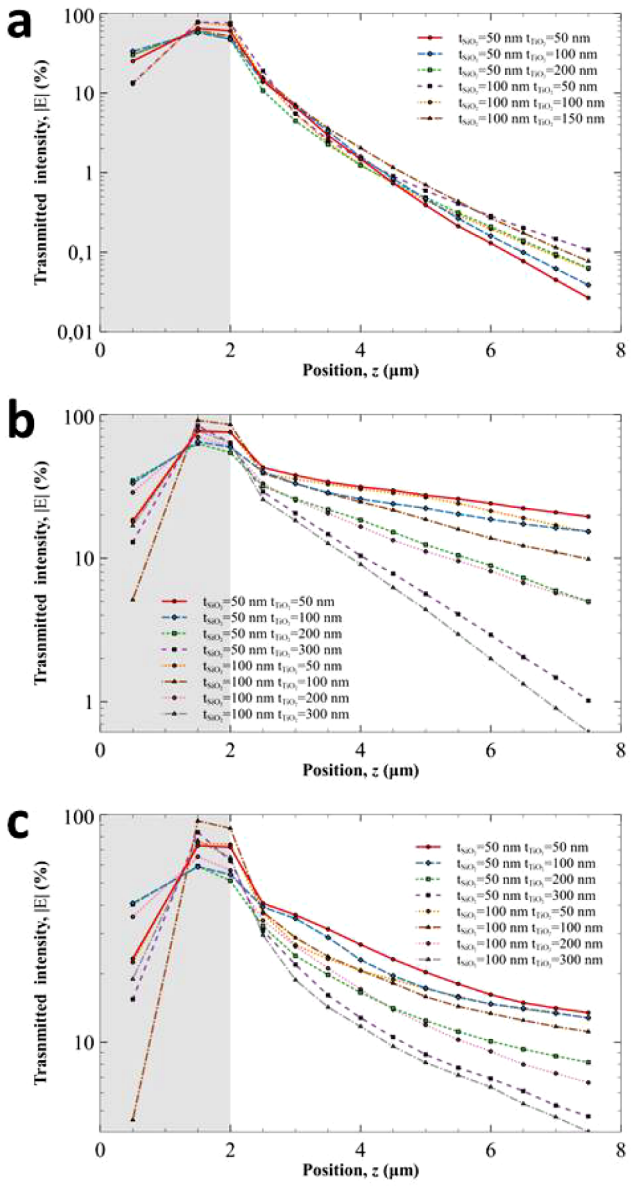

Fig. 3. Electric field profile for structures with a periodicity of 700 nm (a), 2 μm (b) and 4 μm (c).

is shown in Fig. 4, where the linear term a_1 is plotted against the TiO_2 volume fraction (see Section 3.1 and Table 1). From this it can be seen that the thickness of the silicon oxide layer has little effect. Nevertheless, as explained in Section 2.2, SiO_2 is formed at the expense of silicon and, therefore, a thicker layer of silicon oxide slightly reduces the light absorption of the substrate. For the large pitch structures (2 and 4 μm) this effect is negligible, but it is more noticeable as the pore pitch reduces (700 nm). The expected trend of larger light absorption with increasing the thickness of the TiO_2 layer is observed in Fig. 4. It is obvious that the samples with a periodicity of 700 nm have very large light absorption. However, the 2 μm periodicity samples show overall less absorption than the larger 4 μm structures. This is attributed to the smaller amount of silicon substrate left for the former and to the very high absorption of light at the first micron, so any further propagation will be almost meaningless.

The reflectance for each studied structure (see Table 1) is obtained directly from the simulated values and it is summarized in Table 2. The reflectance values were calculated as the obtained field strength at position $z = 0.5\mu m$ minus the source field, and depend on the periodicity of the macroporous silicon structure as well as the thicknesses of the SiO_2 and TiO_2 layers inside the microchannels. Taking into account the values of light absorption and reflectance, it is concluded that the optimal structures where the excitation light reach deep into the channels, therefore maximizing efficiency, are those with a periodicity of 2 μm and 4 μm. Current technological limitations in fabrication make the 4 μm structure more suitable, and this is the one used in our experiments.

3.2. Characterization of the macroporous silicon photocatalytic structures

Fig. 5 corresponds to low-magnification FESEM images of the macroporous silicon structure. A perfect square lattice arrangement of channels of 2 μm side and 200 μm length with a pitch distance of 4 μm is observed, which yields a channel density of 9×10^6 channels cm^{-2} and a specific contact area of 5×10^5 m^2_{ch} m^{-3} ('ch' stands for channels).

As deduced from FESEM images recorded in individual microchannels, the macroporous silicon structures were successfully coated by a SiO_2 layer of about 50 nm in thickness (Fig. 6a and b) and by a continuous thin layer of TiO_2 (Fig. 6c and d) of about 300 nm. A high magnification image of the TiO_2 layer is depicted in Fig. 7a and shows a homogeneous distribution of nanoparticles of about 5 nm in size. The Raman spectra recorded on the TiO_2 layer showed bands at 143, 197, 398, 513 and 639 cm^{-1} (Fig. 7b), which corresponds to the anatase polymorph of TiO_2, in accordance to the calcination temperature used during the preparation of the TiO_2 coating (723 K) [25]. In addition, a signal at 520 cm^{-1} corresponds to the Raman active mode of the silicon substrate. The Au and Pt nanoparticles supported on TiO_2 were imaged directly inside the microchannels using backscattered electrons (Figs. 6d, 7b and c); most of them measure between 4 and 8 nm.

3.3. Photocatalytic experiments

The macroporous silicon photocatalytic structures were tested in the photogeneration of hydrogen at atmospheric pressure using different gaseous EtOH:H_2O mixtures (from 0 to 100% EtOH, molar) and temperatures (from 25 to 60 °C) at a gas hourly space velocity of GHSV = 100,000 h^{-1}. For comparative purposes, the steady-state hydrogen photoproduction rates obtained at 25 °C and EtOH:H_2O = 1:10 (molar) are shown in Fig. 8. The blank experiment conducted over the macroporous silicon structure without photocatalyst, SiO_2/Si, produced a negligible amount of hydrogen (0.025 μmol H_2 h^{-1}). After depositing the layer of the semiconductor TiO_2 over the microchannels of the macroporous silicon structure (sample TiO_2/SiO_2/Si) the photoactivity increased up to about 0.1 μmol H_2 h^{-1}, as expected from the photocatalytic properties of anatase [4]. When either Au or Pt nanoparticles were anchored on the surface of the TiO_2 layer, the photoproduction of hydrogen boosted notably, in accordance to previous reports, where the enhancement of the hydrogen formation rate is ascribed to the electron-acceptor characteristics of the metal nanoparticles, which accommodate the electrons from the conduction band of TiO_2 upon irradiation with light with a higher energy than the TiO_2 bandgap [27,28]. The mechanism of hydrogen formation from water-ethanol mixtures on M/TiO_2 photocatalysts with UV light has been discussed extensively in the literature and it is not treated here [4,27]. Hydrogen photoproduction rates of 4.8 and 4.2 μmol H_2 h^{-1} were recorded on the photocatalytic structures Au/TiO_2/SiO_2/Si and Pt/TiO_2/SiO_2/Si, respectively. The hydrogen production was fast upon light irradiation and the hydrogen photoproduction rates were very stable over time (see inset in Fig. 8). The only products of the photoreaction detected were hydrogen and acetaldehyde in equimolar amount, which originated by the oxidation of ethanol by the holes in the valence band of the photocatalyst.

Similar photocatalytic tests were performed over the Au/TiO_2/SiO_2/Si photocatalytic structure varying the composition of the

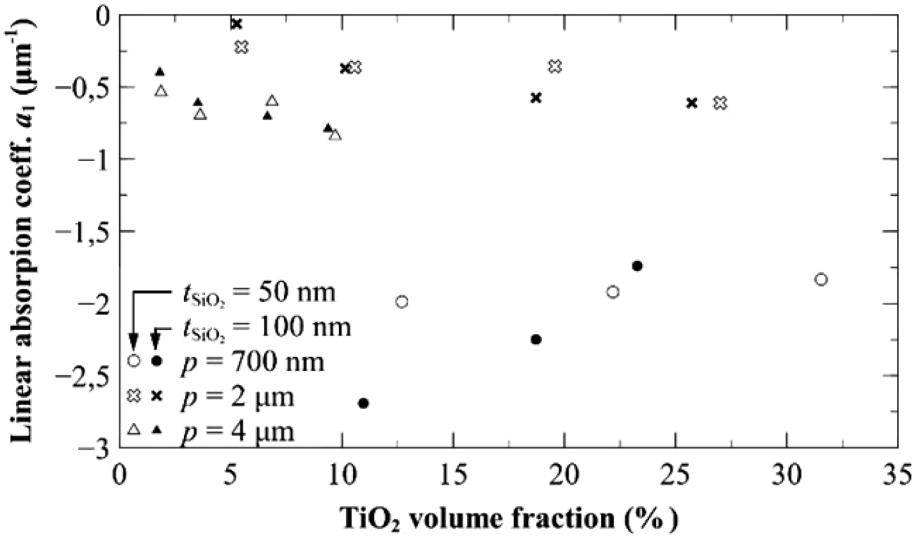

Fig. 4. Linear absorption coefficient with respect to the amount of TiO_2 present in the structures.

EtOH:H_2O mixture from 0 to 100% EtOH (molar), and the best photoproduction of hydrogen was obtained at 10% EtOH (0.4 μmol H_2 h^{-1} for 100% H_2O, 0.8 μmol H_2 h^{-1} for 5% EtOH and 2.8 μmol H_2 h^{-1} for 100% EtOH). The photocatalytic structure Pt/TiO_2/SiO_2/Si was also tested with commercial bioethanol (10% molar) under the same conditions. Interestingly, the photoproduction of hydrogen increased from 4.2 to 5.8 μmol H_2 h^{-1}. Taking into account the presence of Sulphur compounds, aldehydes, polyols and carboxylic acids, among others, in commercial bioethanol, it is not possible to unambiguously ascribe the observed effect on the photoproduction of hydrogen to a given compound. The adsorption strength of the different organic molecules and that of the resulting oxidation products can compete and conduct to different hydrogen photoproduction rates. It is remarkable that the photocatalytic structure loaded with Pt is robust for the photoproduction of hydrogen from commercial bioethanol.

The photocatalytic performance of the macroporous structures Au/TiO_2/SiO_2/Si and Pt/TiO_2/SiO_2/Si were tested at different temperatures. Fig. 9a shows the hydrogen photoproduction rates obtained from 25 to 60 °C. The photoproduction of hydrogen increased with temperature, reaching values of 11.7 and 8.8 μmol H_2 h^{-1} at 60 °C for Au/TiO_2/SiO_2/Si and Pt/TiO_2/SiO_2/Si, respectively. The corresponding Arrhenius plots are shown in Fig. 9b, and the activation energy values obtained are 21.0 kJ mol^{-1} for Au/TiO_2/SiO_2/Si and 17.4 kJ mol^{-1} for Pt/TiO_2/SiO_2/Si. These values are in accordance with previous reports of similar photocatalysts [14,15].

3.4. Hydrogen production rates on a reactor volume basis compared to other photocatalytic devices

The comparison of the photocatalytic performance between different photoreactor geometries is not simple because numerous parameters are involved, mainly related to photon delivery and mass transfer, which ultimately determine the photocatalytic efficiency. For

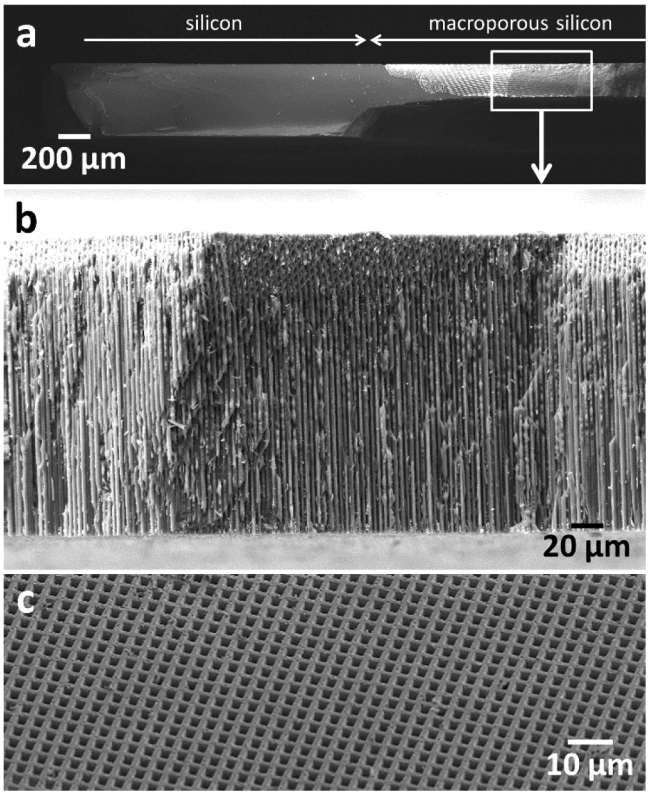

Fig. 5. FESEM images of the macroporous silicon structure in profile view (a, b) and frontal view (c).

Table 2
Calculated reflectance (in %) for each geometry.

Periodicity (nm)	t_{SiO_2}(nm)	50				100				
	t_{TiO_2}(nm)	50	100	200	300	50	100	150	200	300
700		25.2	33.5	30.2	–	13.4	13.1	30.4	–	–
2000		18.0	33.3	34.7	12.9	18.5	5.13	–	28.7	16.8
4000		23.3	40.8	40.4	15.4	22.5	4.56	–	35.6	19.0

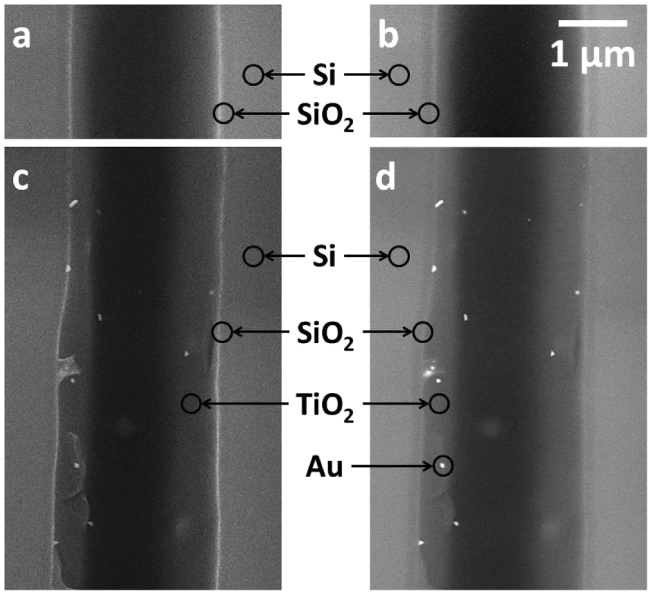

Fig. 6. FESEM images of a single microchannel of sample SiO_2/Si recorded with secondary electrons (a) and backscattered electrons (b), and of sample $Au/TiO_2/SiO_2/Si$ recorded with secondary electrons (c) and backscattered electrons (d).

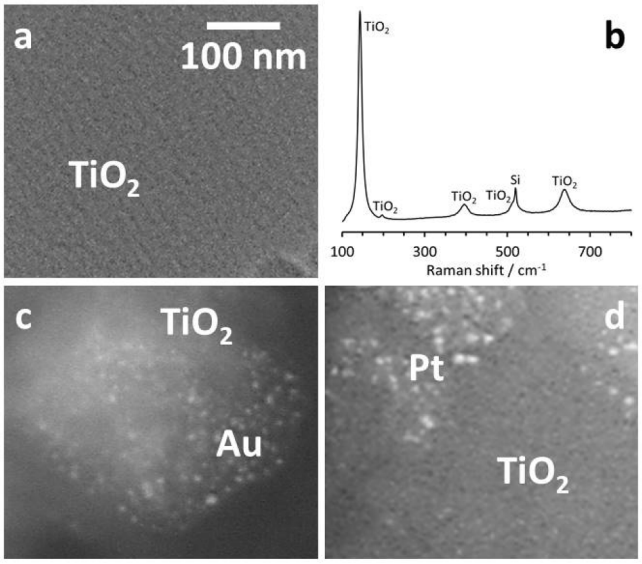

Fig. 7. FESEM image of the TiO_2 layer of $TiO_2/SiO_2/Si$ (a) and its corresponding Raman spectrum (b), and FESEM images of the M/TiO_2 coatings on the microchannels of samples $Au/TiO_2/SiO_2/Si$ (c) and $Pt/TiO_2/SiO_2/Si$ (d) recorded at the same magnification of image (a).

that reason, here we have used the hydrogen production rates on a reactor volume basis as an accurate assessment of the efficiency of a photocatalytic device. We have compared the hydrogen production rates on a reactor volume basis of different photocatalytic wall reactors, where the same Au/TiO_2 photocatalyst has been fixed on their walls and the same light source has been used. These are a classical cordierite honeycomb [13], a PDMS microreactor [14,15], a CD microreactor [16] and the macroporous silicon structure presented in this work. For a proper comparison we have used the hydrogen production rates obtained under similar reaction conditions, that is, atmospheric pressure and 25 °C using a gaseous EtOH:H_2O mixture (10% EtOH, molar) and an irradiance of ca. 80 mW cm^{-2}.

The hydrogen production rates as a function of the photoreactor

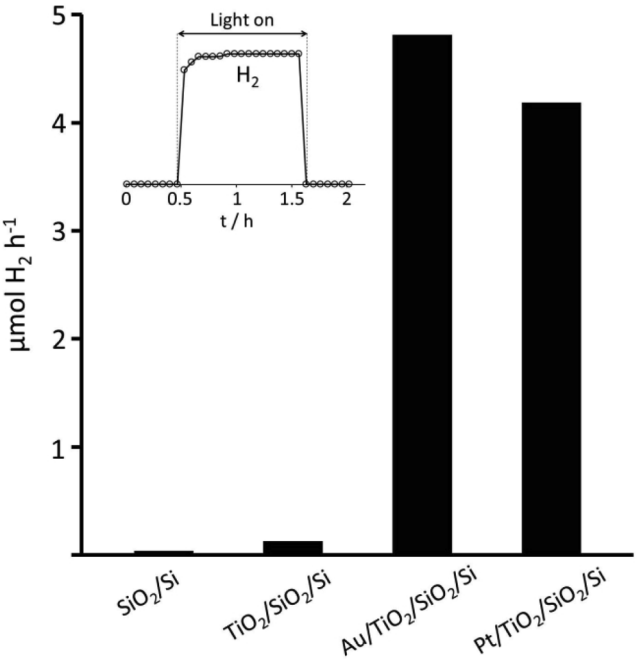

Fig. 8. Hydrogen photoproduction rates recorded over the macroporous silicon structure SiO_2/Si (blank experiment) and photocatalytic structures $TiO_2/SiO_2/Si$, $Au/TiO_2/SiO_2/Si$ and $Pt/TiO_2/SiO_2/Si$ at 25 °C, 10% EtOH (molar) in H_2O and 0.036 s contact time (GHSV = 100,000 h^{-1}). The inset shows the fast response and stable hydrogen photoproduction obtained over the photocatalytic structure $Au/TiO_2/SiO_2/Si$ upon light illumination.

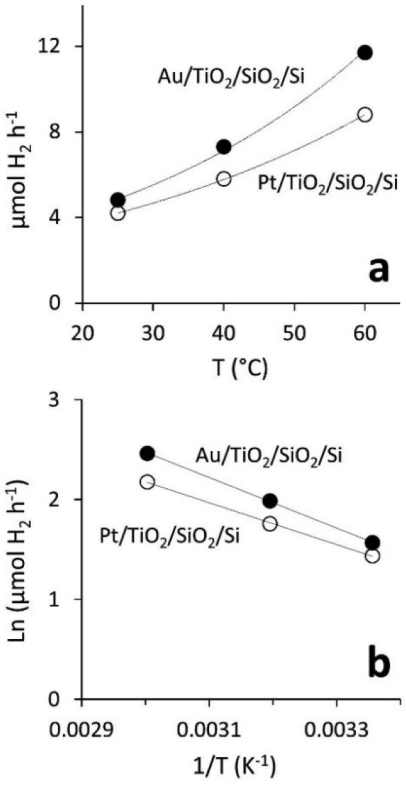

Fig. 9. Hydrogen photoproduction rates recorded over the macroporous photocatalytic structures $Au/TiO_2/SiO_2/Si$ and $Pt/TiO_2/SiO_2/Si$ at different temperatures (a) and the corresponding Arrhenius plots (b). Experimental conditions: atmospheric pressure, 10% EtOH (molar) in H_2O and 0.036 s contact time (GHSV = 100,000 h^{-1}).

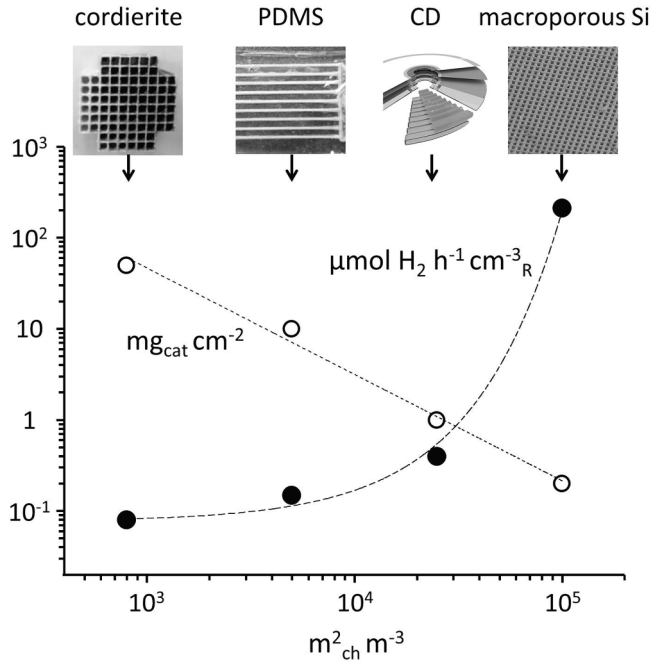

Fig. 10. Comparison of various photocatalytic devices containing channels coated with Au/TiO_2 photocatalyst. The photocatalyst loadings (mg_{cat} cm^{-2}) and hydrogen production rates on a reactor volume basis (μmol H_2 h^{-1} cm_R^{-3}) are plotted against the specific contact area (m^2_{ch} m^{-3}).

volume (μmol H_2 h^{-1} cm_R^{-3}) and the photocatalyst loading normalized to the surface area (mg_{cat} cm^{-2}) are plotted in Fig. 10 against the specific contact area (m^2_{ch} m^{-3}), which is an intrinsic geometrical parameter of the photocatalytic device considered. The hydrogen production rates on a reactor volume basis of the different photocatalytic devices sharply increase when the specific contact area increases. The relationship follows an exponential trend ($y=0.08e^{8Â·10^{-5}x}$) and the hydrogen production rate on a reactor volume basis increases three orders of magnitude when increasing the specific contact area from 10^4 to 10^5 m^2_{ch} m^{-3}. Therefore, the fabulous rate of hydrogen production on a reactor volume basis recorded with the macroporous silicon photocatalytic device (212 μmol H_2 h^{-1} cm_R^{-3}) is directly related to its high specific contact area (10^5 m^2_{ch} m^{-3}). On the other hand, there is an inverse trend between the specific contact area and the photocatalyst loading normalized to the surface area; the larger the specific contact area the lower the photocatalyst loading. The correlation follows a power trend $y = 1.5 \times 10^5 x^{-1.17}$ and it is a direct consequence of the number and size of the channels in the different photocatalytic devices. As the number of channels increases and their diameter decreases, there is more contact area available and the thickness of the photocatalyst layer progressively decreases. However, this does not result in a decrease of the photocatalytic performance because it is well-known that effective photon absorption takes place only in the first micrometers of the photocatalyst coating [13]. Therefore, given the outstanding specific contact area exhibited by the macroporous silicon photocatalytic structure, more photocatalyst is exposed to photons, which ultimately yield a remarkable high photoproduction of hydrogen.

In our experiments (periodicity 4 μm, t_{SiO_2}~50 nm and t_{TiO_2} ~ 300 nm) the reflectance is calculated to be 15.4% (Table 2); this indicates that 84–85% of the impinging light gets absorbed in the microchannels of the macroporous silicon structure. Assuming that all absorbed light is useful to excite the TiO_2 layer and participates in the photocatalytic process, the apparent quantum efficiency (AQE) for the photogeneration of hydrogen of the macroporous silicon photocatalytic structures can be determined [29,30]. Considering that only one photon is required for the liberation of one hydrogen molecule [31,32], the AQE is calculated from the ratio of the amount of H_2 (r_{H2}, 4.8 and 4.2 μmol H_2 h^{-1} for $Au/TiO_2/SiO_2/Si$ and $Pt/TiO_2/SiO_2/Si$ at room temperature) and the amount of photons absorbed by the macroporous silicon photocatalytic structure (N_λ) using the equation $AQE = (r_{H2}/N_\lambda) \times 100$. The photon flux (μmol photons m^{-2} s^{-1}) can be calculated from the irradiance at the position of the sample (I, 800 W m^{-2}) by using the formula $(I \times \lambda)/(10^3 \times h \times c \times N_A)$, where λ = 365 nm, h is the Planck constant, c is the speed of light and N_A is the Avogadro's number. Taking into account that the area illuminated of the macroporous silicon structure is 0.5 cm^2 and that 85% of the photon flux is absorbed in the microchannels, N_λ is calculated to be 370 μmol photons h^{-1}. Therefore, the AQE value is about 1–2%. This value compares well with those reported in the literature for M/TiO_2 photocatalysts [13–16,33].

4. Conclusions

In photocatalysis, efficiency is determined by the photon delivery and mass transfer characteristics of the photoreactor considered, which in turn depend on geometry constraints. In this work, we have prepared macroporous silicon disks containing ordered channels of 2 μm side and 0.2 mm length and have functionalized them with a thin layer (of about 300 nm in thickness) of Au/TiO_2 and Pt/TiO_2 photocatalysts. A normalized hydrogen production rate three orders of magnitude higher than those achieved so far in any conventional photoreactor has been obtained using water-ethanol mixtures in gas phase. According to simulations, the higher hydrogen production rates obtained with the macroporous silicon structures are ascribed to an extraordinary high specific surface area per volume unit and to an enhanced light exploitation. In addition, less photocatalyst weight is required when using macroporous silicon structures with respect to conventional photoreactors. Temperature has a positive effect on the photoproduction of hydrogen in the range studied (up to 60 °C). The photoproduction of hydrogen is improved slightly when commercial bioethanol is fed to the macroporous silicon structure coated with Pt/TiO_2. Catalytic macroporous silicon disks represent a new type of photoreactor that open the possibility of producing solar hydrogen at the microscale with high efficiency on a reactor volume basis.

Declaration of Competing Interest

The authors declare that they have no known competing financial interests or personal relationships that could have appeared to influence the work reported in this paper.

Acknowledgments

This work has been funded by projects MICINN/FEDER RTI2018-093996-B-C31 and RTI2018-095498-J-I00 and GC 2017 SGR 128. JL is a Serra Húnter Fellow and is grateful to ICREA Academia program.

References

[1] D.G. Nocera, Solar fuels and solar chemicals industry, Acc. Chem. Res. 50 (2017) 616–619.
[2] J. Qi, W. Zhang, R. Cao, Solar-to-hydrogen energy conversion based on water splitting, Adv. Energy Mat. 8 (2018) 1701620.
[3] N. Armaroli, V. Balzani, Solar electricity and solar fuels: status and perspectives in the context of the energy transition, Chem. Eur. J. 22 (2016) 32–57.
[4] M. Murdoch, G.I.N. Waterhouse, M.A. Nadeem, J.B. Metson, M.A. Keane, R.F. Howe, J. Llorca, H. Idriss, The effect of gold loading and particle size on photocatalytic hydrogen production from ethanol over Au/TiO_2 nanoparticles, Nat. Chem. 3 (2011) 489–492.
[5] G.I.N. Waterhouse, A.K. Wahab, M. Al-Oufi, V. Jovic, D.H. Anjum, D. Sun-Waterhouse, J. Llorca, H. Idriss, Hydrogen production by tuning the photonic band gap with the electronic band gap of TiO_2, Sci. Rep. 3 (2013) 2849.
[6] K. Meyer, S. Bashir, J. Llorca, H. Idriss, M. Ranocchiari, J.A. van Bokhoven, Photocatalyzed hydrogen evolution from water by a composite catalyst of NH_2-MIL-125(Ti) and surface nickel(II) species, Chem. Eur. J. 22 (2016) (2016)

13894–13899.
[7] H. Al Ghamdi, K. Katsiev, A.K. Wahab, J. Llorca, H. Idriss, Up-conversion luminescence coupled to plasmonic gold nanorods for light harvesting and hydrogen production, Chem. Commun. 53 (2017) 13051–13054.
[8] T.D. Nguyen-Phan, S. Luo, D. Vovchok, J. Llorca, J. Graciani, J. Fernández, S. Sallis, W. Xu, J. Bai, L.F.J. Piper, D.E. Polyansky, E. Fujita, S.D. Senanayake, D.J. Stacchiola, J.A. Rodriguez, Visible light-driven H_2 production over highly dispersed rutenia on rutile TiO_2 nanorods, ACS Catal. 6 (2016) 407–417.
[9] K.C. Christoforidis, P. Fornasiero, Photocatalytic hydrogen production: a rift into the future energy supply, ChemCatChem 9 (2017) 1523–1544.
[10] A. Kubacka, M. Fernández-García, G. Colón, Advanced nanoarchitectures for solar photocatalytic applications, Chem. Rev. 112 (2012) 1555–1614.
[11] A.A. Ismail, D.W. Bahnemann, Photochemical splitting of water for hydrogen production by photocatalysis: a review, Sol. Energy Mater. Sol. Cells 128 (2014) 85–101.
[12] G. Colón, Towards the hydrogen production by photocatalysis, Appl. Catal. A 518 (2016) 48–59.
[13] E. Taboada, I. Angurell, J. Llorca, Dynamic photocatalytic hydrogen production from ethanol–water mixtures in an optical fiber honeycomb reactor loaded with Au/TiO_2, J. Catal. 309 (2014) 460–467.
[14] A. Castedo, I. Uriz, L. Soler, L.M. Gandía, J. Llorca, Kinetic analysis and CFD simulations of the photocatalytic production of hydrogen in silicone microreactors from water-ethanol mixtures, Appl. Catal. B: Environ. 203 (2017) 210–217.
[15] A. Castedo, A. Casanovas, I. Angurell, L. Soler, J. Llorca, Effect of temperature on the gas-phase photocatalytic $_H2$ generation using microreactors under UVA and sunlight irradiation, Fuel 222 (2018) 327–333.
[16] J. Sans, L. Soler, M. Domínguez, J. Llorca, Transforming a compact disk into a simple and cheap photocatalytic nanoreactor, ACS Omega 3 (2018) 6971–6975.
[17] V. Lehmann, H. Föll, Formation mechanism and properties of electrochemically etched trenches in n-type silicon, J. Electrochem. Soc. 137 (1990) 653–659.
[18] J. Llorca, A. Casanovas, T. Trifonov, A. Rodríguez, R. Alcubilla, First use of macroporous silicon loaded with catalyst film for a chemical reaction: a microreformer for producing hydrogen from ethanol steam reforming, J. Catal. 255 (2018) 228–233.
[19] N.J. Divins, E. López, A. Rodríguez, D. Vega, J. Llorca, Bio-ethanol steam reforming and autothermal reforming in 3-μm channels coated with $RhPd/CeO_2$ for hydrogen generation, Chem. Eng. Process. Process Intensif. 64 (2013) 31–37.
[20] N.J. Divins, E. López, M. Roig, T. Trifonov, A. Rodríguez, F. González de Rivera, L.I. Rodríguez, M. Seco, O. Rossell, J. Llorca, A million-channel CO-PrOx microreactor on a fingertip for fuel cell application, Chem. Eng. J. 167 (2011) 597–602.
[21] M. Brust, M. Walker, D. Bethell, D.J. Schiffrin, R. Whyman, Synthesis of thiol-derivatised gold nanoparticles in a two-phase Liquid-Liquid system, J. Chem. Soc. Chem. Commun. 7 (1994) 801–802.
[22] L. Soler, A. Casanovas, A. Urrich, I. Angurell, J. Llorca, CO oxidation and COPrOx over preformed Au nanoparticles supported over nanoshaped CeO_2, Appl. Catal. B: Environ. 197 (2016) 47–55.
[23] J. Llorca, M. Domínguez, C. Ledesma, R.J. Chimentao, F. Medina, J. Sueiras, I. Angurell, M. Seco, O. Rossell, Propene epoxidation over TiO_2-supported Au-Cu alloy catalysts prepared from thiol-capped nanoparticles, J. Catal. 258 (2008) 187–198.
[24] C. Dessal, L. Martínez, C. Maheu, T. Len, F. Morfin, J.L. Rousset, E. Puzenat, P. Afanasiev, M. Aouine, L. Soler, J. Llorca, L. Piccolo, Influence of Pt particle size and reaction phase on the photocatalytic performances of ultradispersed Pt/TiO_2 catalysts for hydrogen evolution, J. Catal. 375 (2019) 155–163.
[25] L. Martínez, M. Benito, I. Mata, L. Soler, E. Molins, J. Llorca, Preparation and photocatalytic activity of Au/TiO_2 lyogels for hydrogen production, Sustainable Energy Fuels 2 (2018) 2284–2295.
[26] E. Aguiló, L. Soler, A. Casanovas, A.J. Moro, J.C. Lima, L. Rodríguez, J. Llorca, Gold (I)-complex–titania hybrid photocatalyst for hydrogen production, ChemCatChem 9 (2017) 3289–3292.
[27] Z.H.N. Al-Azri, W.-T. Chen, A. Chan, V. Jovic, T. Ina, H. Idriss, G.I.N. Waterhouse, The roles of metal co-catalysts and reaction media in photocatalytic hydrogen production: Performance evaluation of M/TiO_2 photocatalysts (M = Pd, Pt, Au) in different alcohol–water mixtures, J. Catal. 329 (2015) 355–367.
[28] A.S. Hainer, J.S. Hodgins, V. Sandre, M. Vallieres, A.E. Lanterna, J.C. Scaiano, Photocatalytic hydrogen generation using metal-decorated TiO_2: sacrificial donors vs true water splitting, ACS Energy Lett. 3 (2018) 542–545.
[29] T. Maschmeyer, M. Che, Catalytic aspects of light-induced hydrogen generation in water with TiO_2 and other photocatalysts: a simple and practical way towards a normalization? Angew. Chem. Int. Ed. 49 (2010) 1536–1539.
[30] H. Kisch, On the problem of comparing rates or apparent quantum yields in heterogeneous photocatalysis, Angew. Chem. Int. Ed. 49 (2010) 9588–9589.
[31] O.I. Micik, Y. Zhang, K.R. Cromack, A.D. Trifunac, M.C. Thurnauer, Photoinduced hole transfer from TiO_2 to methanol molecules in aqueous solution studied by electron paramagnetic resonance, J. Phys. Chem. 97 (1993) 13284–13288.
[32] A. Yamakata, T. Ishibashi, H. Onishi, Electron- and hole-capture reactions on Pt/TiO_2 photocatalyst exposed to methanol vapor studied with time-resolved infrared absorption spectroscopy, J. Phys. Chem. B 106 (2002) 9122–9125.
[33] W.-T. Chen, A. Chan, D. Sun-Waterhouse, J. Llorca, H. Idriss, G.I.N. Waterhouse, Performance comparison of Ni/TiO_2 and Au/TiO_2 photocatalysts for H_2 production in different alcohol-water mixtures, J. Catal. 367 (2018) 27–42.

Journal of Photochemistry & Photobiology, A: Chemistry 418 (2021) 113406

Contents lists available at ScienceDirect

Journal of Photochemistry & Photobiology, A: Chemistry

journal homepage: www.elsevier.com/locate/jphotochem

Hydrogen photoproduction on TiO_2-reduced graphene oxide hybrid materials from water-ethanol mixture

Jarosław Serafin [a,*], Ewelina Kusiak-Nejman [b,*], Agnieszka Wanag [b], Antoni W. Morawski [b], Jordi Llorca [a]

[a] Institute of Energy Technologies, Department of Chemical Engineering and Barcelona Research Center in Multiscale Science and Engineering, Universitat Politècnica de Catalunya, EEBE, Eduard Maristany 10-14, 08019 Barcelona, Spain

[b] Department of Chemical and Environment Engineering, Faculty of Chemical Technology and Engineering, West Pomeranian University of Technology, Pulaskiego 10, 70-322 Szczecin, Poland

ARTICLE INFO

Keywords:
Hydrogen production
Photocatalysis
Photoreactor
Titanium dioxide
rGO

ABSTRACT

Titanium dioxide mixed with reduced graphene oxide (rGO) has been tested in the photoproduction of hydrogen using UV light from water-ethanol combination in gas phase. The presence of the reduced graphene oxide in TiO_2/rGO nanocomposites affects the physicochemical properties of hybrid materials, thus enhancing the photocatalytic activity. The obtained catalysts have been characterized for physical-chemical properties using X-ray diffraction (XRD), UV–vis spectroscopy, Raman spectroscopy, transmission electron microscopy (TEM)/high-resolution transmission electron microscopy (HRTEM), and Brauner Emmett Teller (BET). The best photocatalyst has been obtained by mixing anatase and rGO (10 wt%) after calcination at 700 °C. This TiO_2-rGO composite exhibited the highest performance with a hydrogen photogeneration rate of 9.5 mmol h^{-1} g^{-1}.

1. Introduction

Nowadays, fossil energy resources are principally used to meet most of the global energy needs. Current energy consumption data suggests that soon, there will be significant problems and challenges related to energy supply and demand. Combustion of fossil fuels provide to emissions of carbon particles, CO_2 and harmful gases such as SO_x and NO_x to the atmosphere [1,2]. Therefore, environmentally friendly fuels, which are both easy to store and cost-effective, are of huge significance for sustainable development [3]. Hydrogen is an perfect candidate as an energy carrier [4]. Currently, various of technologies are used to production of hydrogen. However, only a small group of them can be recognized as environmentally friendly. Hydrogen production by steam reforming of hydrocarbons (natural gas) is a dominant technology, but this technology requires high temperatures (700–1100 °C) and emits large amounts of CO_2 [5]. For this reason, water splitting using light is one of the most interesting advances to hydrogen production. The water separation process can be carried out at an ambient temperature and pressure conditions, and what is most important is environmentally friendly. When higher alcohols are used as sacrificial agents, H_2 production can also be associated with the production of high value products (i.e. acetaldehyde) derived from selective alcohol oxidation [6,7]. Among various semiconductors, TiO_2 has been extensively investigated due to its photosensitivity, chemical and thermal stability, low toxicity, and finally low cost. However, there are some limitations of its applications, it has a large band gap (about 3.2 eV for anatase), which makes it sensitive only to light below 387 nm in the ultraviolet (UV) range, and high recombination rate of electron-hole pairs [8,9]. Attempts have been made to fine tune the conduction band and/or valence band to shorten the band gap [10,11]. Another way to facilitate charge separation is to couple TiO_2 with another conductor. Graphene, as a two-dimensional sp^2 carbon network arranged in a honeycomb structure, is one of the most commonly used materials in recent years for that purpose. It has unique mechanical, optical, electronic and catalytic properties [12,13]. Composite materials containing TiO_2 and graphene may demonstrate increased photocatalytic activity due to very good mobility of electrons in the excited state, which hinders electron-hole recombination. There are many reports in the literature on various photocatalysts based on reduced graphene oxide (rGO) with TiO_2, CdS, WO_3, $BiVO_4$, ZnO [14–20]. Particular attention is focus to the graphene-TiO_2 nanocomposite. Sun et al. [21] synthesized graphene/TiO_2 nanocomposites by simply covering the functionalized graphene with P25

* Corresponding authors.
E-mail addresses: jaroslaw.serafin@upc.edu (J. Serafin), ewelina.kusiak@zut.edu.pl (E. Kusiak-Nejman).

https://doi.org/10.1016/j.jphotochem.2021.113406
Received 2 February 2021; Received in revised form 14 May 2021; Accepted 1 June 2021
Available online 9 June 2021

nanoparticles by heterogeneous coagulation. Li et al. [22] reported a novel Au@CdS/RGO/TiO_2 heterostructure as photoelectrode for photoelectrochemical (PEC) hydrogen generation via splitting water. Moon et al. [23] develop not only organic-electron-donor-free, but also noble-metal-free TiO_2-based photocatalytic system for the generation of H_2O_2; in-situ formation of cobalt phosphate (CoP) was achieved on the reduced graphene oxide (rGO)/TiO_2 composite. Mou et al. [24] reported N-doped graphene (NGR) composite photocatalysts (NGR/TiO_2) for solar energy conversion. Liu et al. [25] develop a facile method to synthesize TiO_2–graphene composites with different exposed crystal facets for hydrogen production. Liu H., et al. [26] prepared RGO/TiO_2 nanocomposites which were synthesized by a straightforward procedure using $TiCl_3$ as both reducing agent to reduce GO and the precursor of TiO_2 for photocatalytic hydrogen production. The photocatalytic effect of reduced graphene oxide, despite many studies, is still the subject of many new studies because of the complexity of the rGO structure (hybridized atoms, variety of functional groups, defects, etc.). The idea of a composite with rGO allows increasing the photocatalytic efficiency because both the specific reaction sites and the photo-corresponding range are improved.

This work shows a facile method to obtain TiO_2–rGO composite photocatalysts by a hydrothermal method and investigation of the effect of calcination temperature on hydrogen's photoproduction. These composites exhibit better hydrogen photoproduction activity than TiO_2.

2. Experimental

2.1. Materials and reagents

Photocatalysts were obtained by mixing reduced graphene oxide and titanium dioxide, which was provided by Grupa Azoty Zakłady Chemiczne "Police" S.A. company (Poland) as a crude titanium dioxide slurry. A solution of ammonia (25%, Avantor Performance Materials Poland S. A.) was added to the crude slurry until pH = 6.8 and dried at 105 °C for 24 h. This material was denoted as starting-TiO_2. The reduced graphene oxide (rGO) was supplied by NANOMATERIALS LS (Poland) and was prepared by a modified Hummer's method. Isopropanol (purity 99.5%) was purchased from Firma Chempur (Poland).

2.2. Synthesis of the photocatalysts

Photocatalysts containing graphene oxide and TiO_2 were synthesized by a hydrothermal method and calcined in Ar to avoid the oxidation of rGO [27,28]. Initially, 2 g of starting-TiO_2 and rGO (10 wt%) were mechanically mixed in a mortar. The material was transferred to an autoclave containing 2 mL of isopropanol. The mixture was heated at 180 °C for 4 h under autogenous pressure. To remove residual alcohol and water, the pressure valve in the reactor was open and the sample was heated for 1 h. Finally, the material was calcined at 300, 500, 700 and 900 °C for 4 h under Ar flow (60 mL/min). The resulting photocatalyst were designed as TiO_2/rGO-10-300, TiO_2/rGO-10-500, TiO_2/rGO-10-700 and TiO_2/rGO-10-900. Reference samples were obtained following exactly the same method, but without rGO (denoted as TiO_2, TiO_2-500 and TiO_2-700 before calcination and after calcination at 500 and 700 °C, respectively).

2.3. Characterization methods

The phase composition and the crystalline structure of the photocatalysts were characterized by X-ray diffraction (XRD) with a PANalytical Empyrean X-ray diffractometer using Cu Kα radiation (λ = 1.54056 Å). The average crystallite size was calculated according to the Scherrer's equation. Titania anatase over rutile ratio was estimated following the method described elsewhere [29]. The identification of anatase and rutile phases was based on JCPDS 01-070-7348 and 01-076-0318 standard cards, respectively. Diffuse absorbance UV–vis spectroscopy was acquired on a JASCO V-650 spectrophotometer equipped with a PIV-756 integrating sphere. Barium sulphate was used as standard. The bandgap (E_g) was determined from Tauc graphs by plotting $[F(R)h\nu]^{1/2}$ as a function of hυ and extrapolating the linear portion to $[F(R)h\nu]^{1/2} = 0$ [30]. The surface area (S_{BET}) and porous structure of the photocatalysts were determined by nitrogen adsorption–desorption measurements at 77 K on a QUADRASORB evo™ Gas Sorption analyzer. Prior to measurements, the samples were degassed at 100 °C for 12 h under vacuum. The surface area (S_{BET}) was calculated by the multipoint Brunauer-Emmett-Teller (BET) method, while the total pore volume (V_{total}) was determined on the basis of the adsorbed N_2 at a relative pressure $p/p_0 = 0.99$. The micropore volume ($V_{microDR}$) was calculated by applying the Dubinin-Radushkevich (DR) equation using adsorption branches of the measured isotherm. The mesopore volume (V_{meso}) was calculated by subtracting micropore volume from the total pore volume. Raman spectra were collected with a Renishaw in Via Qontor confocal Raman microscope equipped with a 532.1 ± 0.3 nm laser with a nominal 100 mW output power directed through a specially adapted Leica DM2700 M microscope (x50 magnification). Spectra were acquired in the two ranges, 50–800 cm^{-1} and 1000–2000 cm^{-1}, with an exposure time of 0.5 s, 1% of maximum laser power and 18 repetitions. Total carbon content was determined using a CN 628 elemental analyzer (LECO Corporation, USA). Transmission electron microscopy analysis (HRTEM and HAADF-STEM) was carried out using a FEI Tecnai F20 electron microscope equipped with a field emission electron gun operating at 200 kV. The samples were prepared by dispersing the powder catalysts in an alcohol suspension; a drop of the dispersion was placed over a grid with a lacey-carbon film.

2.4. Photocatalytic hydrogen production

To perform the photocatalytic tests were use a tubular glass photoreactor (Fig. S1). The analyses were made at 25 °C and atmospheric pressure under dynamic conditions. Gaseous reactant mixture of H2O: EtOH = 9:1 on a molar basis, which was directly introduced in the photoreactor, was obtained with an argon stream (20 mL/min) bubbled through a Drechsel bottle containing a liquid mixture of water–ethanol. The partial pressure of ethanol was 0.30 kPa. An UV light source from SACOPA S.A.U. consisting of four LEDs emitting at 365 ± 5 nm and a synthetic quartz cylindrical lens that transmitted the light to the photocatalyst was used [31,32]. The photocatalyst samples (2 mg) were dispersed in ethanol and ultrasonicated and the resultant suspension was placed onto circular porous cellulose membranes (from Albet-LabScience, pore size 35–40 μm, 80 g/m^2, thickness 0.18 mm). The sizes of membrane surface covered by the photocatalyst was 1.88 cm^{-2}. The impregnated cellulose membranes were dried at 60 °C, weighted to check for the amount of supported photocatalyst and then placed in the photoreactor. The gas hourly space velocity (GHSV) was ca. 100,000 h^{-1}. The irradiance over the sample was 80 ± 2 mW/cm^2 as measured with a UV-A sensor (model PMA 2110, Solar Light Co.), which registered the UV radiation within spectral response 320–400 nm, connected to a radiometer (model PMA2200, Solar Light Co.). The outlet of the photoreactor was directly connected to a Varian CP-4900gas chromatograph (GC) equipped with MS 5 Å, Plot U and Stabilwax columns for a complete analysis of the photoreaction products, which were monitored on-line every 4 min.

The apparent quantum yield (AQY) was calculated using equation:

$$AQY = \frac{2n_{H2}}{n_p}\hat{A}\cdot 100 = \frac{nN_A}{E_T/E_P}\hat{A}\cdot 100$$

where n_{H2} is the number of molecules of H_2 generated and n_p is the number of incident photons reaching the catalyst. The number of incident photons can be calculated by $np = E_T/E_p$, where E_T is the total energy reaching the catalyst and E_p is the energy of a photon.

E_T = PSt, where P (W m^2) is the power density of the incident

monochromatic light, S (m^2) is the irradiation area and t(s) is the duration of the incident light exposure. $E_p = hc/\lambda$, where h is the Planck's constant, c the speed of light and λ (m) is the wavelength of the incident monochromatic light. The number of hydrogen molecules can be calculated as $n_{H2} = nN_A$, where n are H_2 moles evolved during the time of light exposure (t), and N_A is the Avogadro constant [33]. In our case, experimental conditions were: the wavelength of the incident light was λ = 365 nm, the power density of the incident light at the paper surface was P = 80 mW cm^2 and the irradiation area was S = 1.88 cm^2.

3. Results and discussion

3.1. Characterization of the samples

The XRD profiles of the samples prepared in this work are presented in Fig. 1. Table 1 lists the crystalline phase composition and the average crystallite size of anatase and rutile phases.

The sample TiO_2 used as precursor primarily consists of anatase phase (98%) with a negligible fraction of the rutile phase, according to previous reports. The XRD patterns for rGO-modified TiO_2 did not show peaks corresponding to graphene. This has also been observed in our previous works [34–36] and it is related to the small amount of rGO with relatively low diffraction intensity [37] and also to the overlapping of the main rGO peak at 24.2° with that of anatase at 25.4° [38]. The appearance of rutile at the expense of anatase generally occurs at calcination temperatures higher than ca. 500 °C [39]. Above this temperature, a typical anatase-to-rutile phase transition is observed. It is interesting to note that the presence of rGO strongly inhibits the anatase-to-rutile transformation. In particular, the samples calcined at 700 °C in absence and presence of rGO ($TiO_2$700 and TiO_2/rGO-10-700) contain 72% and 16% of rutile phase, respectively (Table 1). Thus, the anatase phase exhibits much higher thermal stability after rGO modification, which is a direct proof of the intimate contact between rGO and TiO_2. Also, 14% of anatase phase is found for TiO_2/rGO-10 calcined at 900 °C, whereas at this temperature the bare TiO_2 anatase phase fully converts to rutile [40]. This behaviour is opposite to that exhibited by TiO_2 samples doped with carbon/graphite, which are strong reducing agents and promote the anatase to rutile transformation via oxygen vacancy and defect formation [41,42]. In addition, the presence of rGO also inhibited the growth of both anatase and rutile crystallites (Table 1), again pointing out to a strong interaction between rGO and TiO_2. Therefore, the rGO flakes restrictTiO_2 phase transformation and sintering.

The morphology of the prepared photocatalysts TiO_2/rGO-10–300 andTiO_2/rGO-10-700 were characterized by TEM and images are shown in Fig. 2. In both samples, HRTEM images showed TiO_2 with lattice spacing of 0.36 nm, which corresponds to the anatase (1 0 1) plane. For theTiO_2/rGO-10-700 TiO_2 sample, lattice spacing of 0.25 nm corresponds to the rutile (1 0 1) plane. These results are in accordance with the XRD data presented in Table 1.

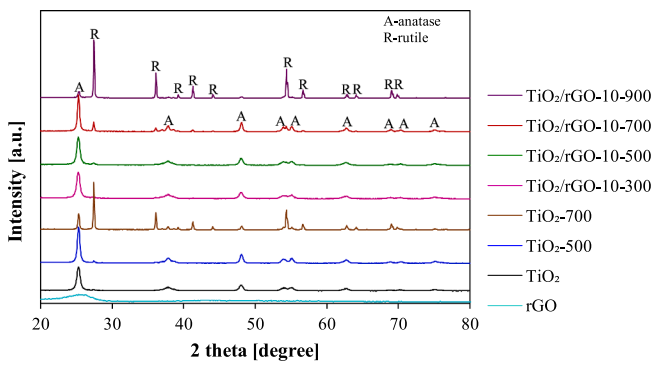

Fig. 1. XRD patterns of the samples prepared in this work.

Table 1
Phase composition and crystallite size (d) of the samples prepared in this work.

Sample	Crystalline phase concentration[%]		Anatase	Rutile
	Anatase	Rutile	d_A [nm]	d_R [nm]
TiO_2	98	2	18	33
TiO_2/rGO-10-300	98	2	19	27
TiO_2-500	98	2	26	47
TiO_2/rGO-10-500	98	2	21	28
TiO_2-700	28	72	58	>100
TiO_2/rGO-10-700	84	16	35	>100
TiO_2/rGO-10-900	14	86	42	>100

The UV–vis absorption spectra of the samples used in this work are presented in Fig. 3 and the corresponding calculated band gap energy values are listed in Table 2. The TiO_2 material is characterized by high absorption in the UV region [43]. TiO_2 samples calcined at 500 and 700 °C show a noticeable shift of the absorption edge into the visible region caused by the anatase-to-rutile transformation [44]; this is particularly evident for TiO_2-700. Photocatalysts modified with rGO exhibit absorption in the visible region. This absorption is caused by both the rGO content and calcination, which caused changes in samples colour. Moreover, it can be observed that the absorption increases with the increase of calcination temperature. After modification with rGO and calcination, photocatalysts changed colour from white for TiO_2-A180 to grey. The highest absorption in the visible region was noticed for the sample TiO_2/rGO-10-900. For this sample, it can also be observed a significant shift in the absorption into the visible region related to a decrease of the energy band-gap value. Estimated band gap values for all tested nanomaterials are listed in Table 2. The band gap energy for TiO_2/rGO-10-900 material is the lowest and reaches 2.95 eV (the band gap varies from 2.95 to 3.28 eV). Both shifts in the absorption into the visible region and narrowing the band gap energy are attributed to the presence of rutile in the photocatalyst [43].

The BET surface area values and pore volumes of the nanomaterials studied in this work are listed in Table 2 as well as their carbon content determined by elemental analysis. All TiO_2-rGO materials exhibit similar carbon content, between 6.5 and 7.2 wt%. It is noted that a mesoporous structure characterizes the photocatalysts. The calcination of TiO_2 generally led to the decrease of the S_{BET} values and total pore volume, as expected. This is strongly related to the increase of crystallite size (see Table 1) [45]. By comparing the results obtained for rGO-decorated photocatalysts and reference TiO_2 samples, it is possible to conclude that rGO modification caused a noticeable increase of the S_{BET} surface area and total pore volume. This observation is attributed to the structural and physical properties of rGO (S_{BET} = 310 m^2/g; V_{total} = 0.32 cm^3/g) [46].

Fig. 4 shows the Raman spectra of the rGO-TiO_2 photocatalysts. In all cases the spectra is dominated by the characteristic signals of anatase (presented in Fig. 4a) and the broad D and G peaks of rGO located at ca. 1300 and 1600 cm^{-1}, respectively (Fig. 4b). The typical modes of anatase could be observed: the $E_{g(1)}$ peak (148 cm^{-1}), $B_{1g(1)}$ peak (394 cm^{-1}), $E_{g(2)}$ peak (637 cm^{-1}), and the A_{1g} + $B_{1g(2)}$ modes centered at 512 cm^{-1}. No rutile peaks are visible due to their low intensity in the Raman spectra with respect to anatase. The two characteristic peaks at about 1328 and 1602 cm^{-1} for the graphitized structures were also observed in the Raman spectrum of the rGO-TiO_2 composites. The values of the G/D intensity ratio range from 0.76 to 0.86, which are characteristic of the high disorder of the rGO structure [47].

3.2. Photoproduction of hydrogen

The samples were tested in the photogeneration of hydrogen at atmospheric pressure using a gas EtOH:H_2O mixture (10% EtOH, molar) at room temperature (25 °C) at a gas hourly space velocity of GHSV = 100,000 h^{-1}. Steady-state normalized hydrogen photogeneration rates

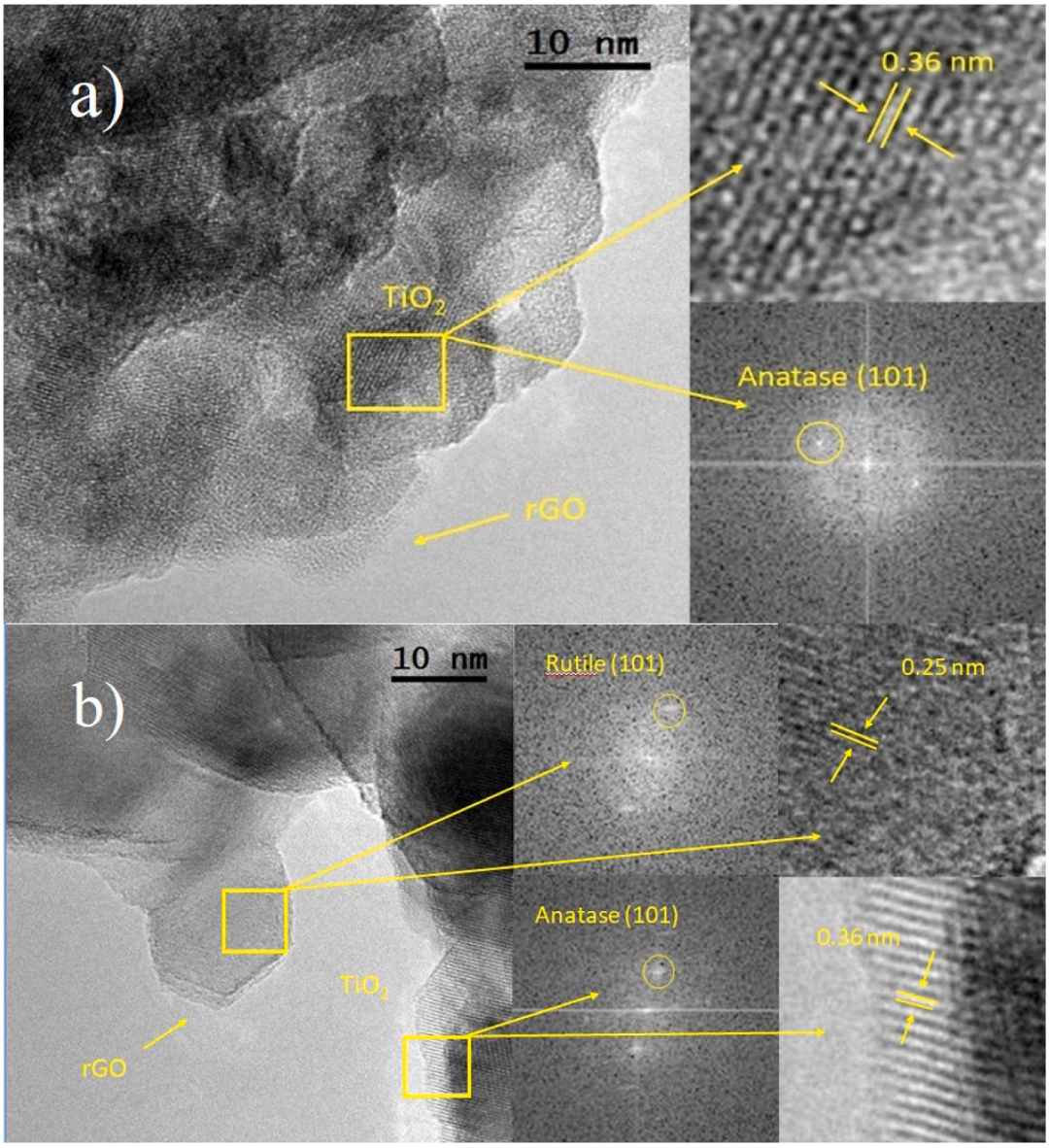

Fig. 2. TEM images of TiO_2/rGO-10-300 (a) andTiO_2/rGO-10-700 (b).

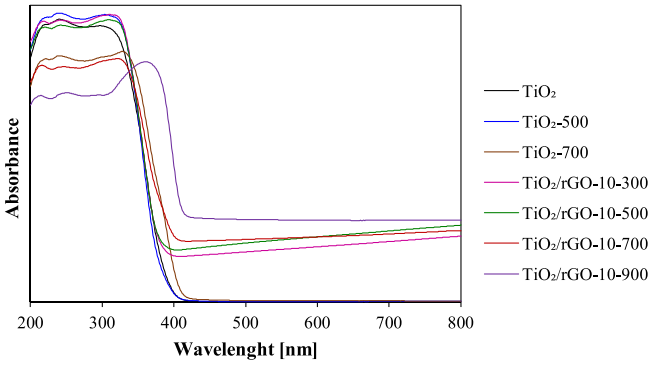

Fig. 3. UV–Vis absorbance spectra of TiO_2 and rGO- TiO_2 photocatalysts.

Table 2
Physical properties, carbon content and calculated band gap values.

Sample code	S_{BET} [m^2/g]	V_{total} [cm^3/g]	V_{micro} [cm^3/g]	V_{meso} [cm^3/g]	Carbon content [wt. %]	Eg [eV]
TiO_2	97	0.40	0.04	0.36	0.6	3.28
TiO_2/rGO-10-300	140	0.35	0.05	0.30	6.5	3.27
TiO_2/rGO-10-500	126	0.38	0.05	0.33	6.7	3.28
TiO_2-500	78	0.23	0.03	0.20	–	3.29
TiO_2/rGO-10-700	91	0.23	0.03	0.20	7.2	3.15
$TiO_2$700	15	0.05	0.004	0.05	–	3.02
TiO_2/rGO-10-900	50	0.12	0.02	0.10	6.6	2.95
rGO	310	0.31	0.12	0.19	–	–

are shown in Fig. 5. It can be easily seen that the photoproduction of hydrogen is higher for the photocatalysts modified with rGO than for reference samples without rGO. The reference samples TiO_2, TiO_2-500 and TiO_2-700 produced smaller amounts of hydrogen comparing with samples modified with rGO; almost an order of magnitude. Therefore, a significant increase in the photogeneration of hydrogen is associated with the combination of titanium dioxide with rGO (Fig. S2).

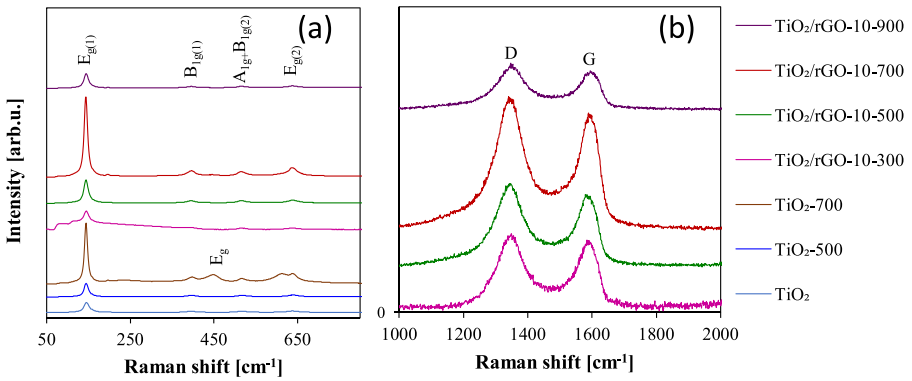

Fig. 4. Raman spectra of rGO-TiO_2 photocatalysts.

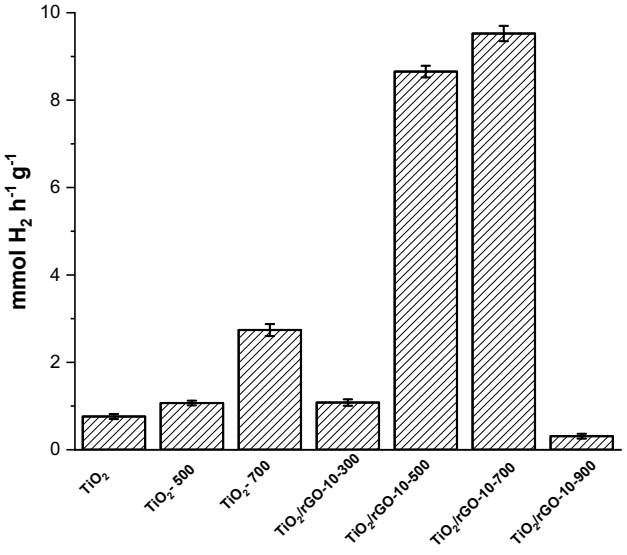

Fig. 5. Hydrogen photoproduction rates recorded at 25 °C, EtOH:H_2O = 1:9 (molar) and GHSV = 100,000 h^{-1} (0.036 s contact time).

Importantly, the production of hydrogen was stable over time. Reduced GO promotes electron mobility and decreases charge carrier recombination rate. The photogenerated electrons migrate from the TiO_2 to rGO, improving the photoactivity [48]. The calcination temperature during the preparation of the photocatalysts has a strong effect on the photoproduction of hydrogen in the rGO-TiO_2 samples. The phase composition of photocatalyst is one of the most crucial parameter that affects photoactivity. It is commonly known that samples consisting mainly of the anatase phase show higher activity than samples contain rutile [49]. Accordingly, the TiO_2-700 and TiO_2/rGO-10-900 samples containing 72 and 86% of rutile, respectively, shows definitely lower hydrogen production. The most substantial effect is observed for TiO_2/rGO-10-700 photocatalyst consisting of 84 and 16% of anatase and rutile, respectively. A similar phase content is encountered in the commercial photocatalyst AEROXIDE® TiO_2 P25, which is considered the standard photocatalyst. It has been demonstrated that such proportion of anatase to rutile is related to better charge carriers separation and higher activity [50]. Both effects, rGO modification and calcination process benefit the photocatalytic efficiency of the material. The apparent quantum yield (AQY) of TiO_2-rGO-700, calculated as described in the Section 2.4, was 2.24%, notably above the 0.18% estimated for pure TiO_2 (Table S1).

The production of hydrogen using titanium dioxide has been the subject of many studies. The summary of recent representative studies described in the literature carried out on TiO_2 composites and the results of this study are shown in Table 3. The catalysts prepared in this work show H_2 photoproduction rates which are among the highest ever reported in the literature, competing only with nitrogen-doped TiO_2-C_3N_4 composites.

The production of hydrogen using titanium dioxide has been the subject of many studies. The summary of recent representative studies described in the literature carried out on TiO_2 composites, and the results of this study are shown in Table 3. One can notice a significant increase in the photoproduction of composite hydrogen to titanium oxide alone. Titanium dioxide without the addition of rGO produced smaller amounts of hydrogen concerning the samples modified with rGO. Similar conclusions get Chen et al. [51] when investigating commercial titanium oxide and titanium oxide doped with Au. Also, Xing et al. [52] under similar conditions achieved hydrogen production for TiO_2 and $NiTiO_3$ / TiO_2: 3 mmol h^{-1} g^{-1}, 11.5 mmol h^{-1} g^{-1}, respectively. The catalysts prepared in this work show H_2 photoproduction rates, one of the highest among ever reported in the literature, competing only with nitrogen-doped TiO_2-C_3N_4 composites.

4. Conclusions

Composites of TiO_2 with 10 wt% of reduced graphene oxide were successfully prepared by a hydrothermal method and calcined at different temperatures under argon. The results revealed that the TiO_2-rGO composite calcinated at 700 °C exhibited the highest performance with a hydrogen photogeneration rate of 9.53 mmol/$h^{-1}g^{-1}$. This represents a novel and useful approach to the design of a new generation of photocatalysts for the photoproduction of hydrogen because the use of TiO_2 is limited by its large band gap and the relatively fast recombination rate of photogenerated electrons and holes. One way to enhance the electron-hole lifetime in TiO_2 is to combine it with rGO and suppress recombinations centers by performing a thermal treatment. The presence of rGO in TiO_2-rGO composites has two strong effects on the thermal treatment with respect to bare TiO_2. Firstly, it hinders sintering of TiO_2; secondly, it hinders the structural transformation of anatase into rutile. These two effects, together with the concomitant electron delocalization induced by rGO in the TiO_2-rGO composites, result in boosted hydrogen photoproduction rates.

CRediT authorship contribution statement

Jarosław Serafin: Conceptualization, Methodology, Investigation, Writing - original draft. **Ewelina Kusiak-Nejman:** Conceptualization, Methodology, Investigation, Writing - original draft. **Agnieszka Wanag:** Methodology, Investigation, Writing - original draft. **Antoni W. Morawski:** Funding acquisition. **Jordi Llorca:** Funding acquisition, Supervision.

Table 3
H_2 production rates reported for titanium dioxide composites in the literature and H_2 production rates obtained in this work.

Catalyst	Light source	Electron donor	Light intensity (mW· cm^{-2})	H_2 production (mmol·h^{-1}·g^{-1})	Ref.
TiO_2/rGO	UV–Vis	Methanol[l]	NA	0.74	[53]
TiO_2/rGO	>320	Methanol[l]	205	NA	[54]
g-C_3N_4/N[a]-TiO_2nanofibres	Xe lamp	Methanol[l]	NA	8.93	[55]
W/N[b]-TiO_2	Vis	Ethanol[l]	NA	0.018	[56]
C[c]-TiO_2/rGO	Xe lamp	Methanol[l]	135	1.5	[57]
C-TiO_2	Xe lamp	TEOA[f,l]	135	0.049	[57]
C-TiO_2-rGO	Xe lamp	TEOA[l]	135	0.066	[57]
TiO_2/G[d]	UV–Vis	Na_2S/Na_2SO_3[l]	80	0.108	[58]
N[e]-TiO_2/N[e]-GO	Hg lamp	Methanol[l]	NA	0.996	[59]
TiO_2 P90	UV	Water-Ethanol[g]	87 ± 0.5	1.5	[51]
Au/P90-BM	UV	Water-Ethanol[g]	87 ± 0.5	49.3	[51]
TiO_2	UV	Water-Ethanol[g]	79.1 ± 0.5	3.0	[52]
$NiTiO_3$/TiO_2	UV	Water-Ethanol[g]	79.1 ± 0.5	11.5	[52]
TiO_2	UV	Water-Ethanol[g]	80	0.76	This study
TiO_2- 500	UV	Water-Ethanol[g]	80	1.07	This study
TiO_2- 700	UV	Water-Ethanol[g]	80	2.74	This study
TiO_2-rGO-10-500	UV	Water-Ethanol[g]	80	8.66	This study
TiO_2-rGO-10-700	UV	Water-Ethanol[g]	80	9.53	This study

[a] g-C_3N_4-graphitic carbon nitride.

[b] W/N-tungsten/nitrogendoped.

[c] C-complex.

[d] G-denotes grapheme.

[e] N-nitrogen doped.

[f] TEOA-triethanolamine.

[g] gas phase.

[l] liquid phase.

Declaration of Competing Interest

The authors declare that they have no known competing financial interests or personal relationships that could have appeared to influence the work reported in this paper.

Acknowledgments

This work has been funded by projects MICINN/FEDER RTI2018-093996-B-C31 and GC 2017 SGR 128. JL is a Serra Húnter Fellow and is grateful to ICREA Academia program. A. W. Morawski is grateful to the National Science Centre (Poland) grant no. DEC-2012/06/A/ST5/00226.

Appendix A. Supplementary data

Supplementary data to this article can be found online at https://doi.org/10.1016/j.jphotochem.2021.113406.

References

[1] J. Serafin, U. Narkiewicz, A.W. Morawski, R.J. Wrobel, B. Michalkiewicz, Highly microporous activated carbons from biomass for CO_2 capture and effective micropores at different conditions, J. CO_2 Util. 18 (2017) 73–79, https://doi.org/10.1016/j.jcou.2017.01.006.

[2] J. Serafin, M. Baca, M. Biegun, E. Mijowska, R.J. Kaleńczuk, J. Sreńscek-Nazzal, B. Michalkiewicz, Direct conversion of biomass to nanoporous activated biocarbons for high CO_2 adsorption and supercapacitor applications, Appl. Surf. Sci. 497 (2019), 143722, https://doi.org/10.1016/j.apsusc.2019.143722.

[3] S. Mao, S. Shen, L. Guo, Nanomaterials for renewable hydrogen production, storage and utilization, Progr. Nat. Sci.: Mater. Int. 22 (2012) 522–534, https://doi.org/10.1016/j.pnsc.2012.12.003.

[4] D. Jing, L. Guo, L. Zhao, X. Zhang, H. Liu, M. Li, S. Shen, G. Liu, X. Hu, Efficient solar hydrogen production by photocatalytic water splitting: from fundamental study to pilot demonstration, Int. J. Hydrogen Energ. 35 (2010) 7087–7097, https://doi.org/10.1016/j.ijhydene.2010.01.030.

[5] P. Häussinger, R. Lohmüller, A. Watson, Hydrogen, 1. Properties and Occurence. Ullmann's Encyclopedia of Industrial Chemistry, 2011.

[6] R. Navarro Yerga, M.C. Álvarez Galván, F. del Valle, J.A. Villoria de la Mano, J. G. Fierro, Water splitting on semiconductor catalysts under visible-light irradiation, ChemSusChem 2 (6) (2009) 471–485, https://doi.org/10.1002/cssc.200900018.

[7] K. Maeda, K. Teramura, D. Lu, T. Takata, N. Saito, Y. Inoue, K. Domen, Photocatalyst releasing hydrogen from water, Nature 440 (7082) (2006) 295, https://doi.org/10.1038/440295a.

[8] H. Chen, C.E. Nanayakkara, V.H. Grassian, Titanium dioxide photocatalysis in atmospheric chemistry, Chem. Rev. 112 (11) (2012) 5919–5948, https://doi.org/10.1021/cr3002092.

[9] L. Wang, T. Sasaki, Titanium oxide nanosheets: graphene analogues with versatile functionalities, Chem. Rev. 114 (19) (2014) 9455–9486, https://doi.org/10.1021/cr400627u.

[10] G.I.N. Waterhouse, A.K. Wahab, M. Al-Oufi, V. Jovic, D.H. Anjum, D. Sun Waterhouse, J. Llorca, H. Idriss, Hydrogen production by tuning the photonic band gap with the electronic band gap of TiO_2, Sci. Rep. (2013) 2849–2853, https://doi.org/10.1038/srep02849.

[11] X. Zheng, S. Meng, J. Chen, J. Wang, J. Xian, Y. Shao, X. Fu, D. Li, Titanium dioxide photonic crystals with enhanced photocatalytic activity: matching photonic band Gaps of TiO_2 to the absorption peaks of dyes, J. Phys. Chem. C 117 (41) (2013) 21263–21273, https://doi.org/10.1021/jp404519j.

[12] A. Cao, Z. Liu, S. Chu, M. Wu, Z. Ye, Z. Cai, Y.L. Chang, S.F. WangQ, H. Gong, Y. F. Liu, A facile one-step method to produce graphene CdS quantum dot nanocomposites as promising optoelectronic materials, Adv. Mater. 22 (2010) 103–106, https://doi.org/10.1002/adma.200901920.

[13] Q. Li, B. Guo, J. Yu, J. Ran, B. Zhang, H. Yan, J.R. Gong, Highly efficient visible-light-driven photocatalytic hydrogen production of CdS-cluster-decorated graphene nanosheets, J. Am. Chem. Soc. 133 (28) (2011) 10878–10884, https://doi.org/10.1021/ja2025454.

[14] Q. Xiang, J. Yu, M. Jaroniec, Synergetic effect of MoS_2 and graphene as cocatalysts for enhanced photocatalytic H_2 production activity of TiO_2 nanoparticles, J. Am. Chem. Soc. 134 (2012) 6575–6578, https://doi.org/10.1021/ja302846n.

[15] W. Fan, Q. Lai, Q. Zhang, Y. Wang, Nanocomposites of TiO_2 and reduced graphene oxide as efficient photocatalysts for hydrogen evolution, J. Phys. Chem. C 115 (2011) 10694–10701, https://doi.org/10.1021/jp2008804.

[16] Q. Xiang, J. Yu, M. Jaroniec, Graphene-based semiconductor photocatalysts, Chem. Soc. Rev. 41 (2012) 782–796, https://doi.org/10.1039/C1CS15172J.

[17] M. Higashi, R. Abe, T. Takata, K. Domen, Photocatalytic overall water splitting under visible light using $ATaO_2N$ (A = Ca, Sr, Ba) and WO_3 in a $IO_3-/I-$shuttle redox mediated system, Chem. Mater. 21 (8) (2009) 1543–1549, https://doi.org/10.1021/cm803145n.
[18] Y. Wang, W. Wang, H. Mao, Y. Lu, J. Lu, J. Huang, Z. Ye, B. Lu, Electrostatic self-assembly of $BiVO_4$-reduced graphene oxide nanocomposites for highly efficient visible light photocatalytic activities, ACS Appl. Mater. Inter. 6 (15) (2014) 12698–12706, https://doi.org/10.1021/am502700p.
[19] A. Iwase, Y. Ishiguro, A. Kudo, R. Amal, Reduced graphene oxide as a solid-state electron mediator in Z-scheme photocatalytic water splitting under visible light, J. Am. Chem. Soc. 133 (2011) 11054–11057, https://doi.org/10.1021/ja203296z.
[20] M.J. Sampaio, C.G. Silva, R.R.N. Marques, A.M.T. Silva, J.L. Faria, Carbon nanotube–TiO_2 thin films for photocatalytic applications, Catal. Today 161 (1) (2011) 91–96, https://doi.org/10.1016/j.cattod.2010.11.081.
[21] S. Sun L. Gao, Y. Liu, Enhanced dye-sensitized solar cell usinggraphenee TiO2 photoanode prepared by heterogeneous coagulation, Appl. Phys. Lett., 96 (2010) 083113, doi.org/10.1063/1.3318466.
[22] W. Fan, X. Yu, H.-C. Lu, H. Bai, C. Zhang, W. Shi, Fabrication of TiO_2/RGO/Cu_2O heterostructure for photoelectrochemical hydrogen production, Appl. Catal. B-Environ. 181 (2016) 7–15, https://doi.org/10.1016/j.apcatb.2015.07.032.
[23] G.-H. Moon, W. Kim, A.D. Bokare, N.-E. Sung, W. Choi, Solar production of H_2O_2 on reduced graphene oxide-TiO_2 hybrid photocatalysts consisting of earth-abundant elements only, Energy Environ. Sci. 7 (12) (2014) 4023–4028, https://doi.org/10.1039/C4EE02757D.
[24] Z. Mou, Y. Wu, J. Sun, P. Yang, Y. Du, C. Lu, TiO_2 Nanoparticles-functionalized N-doped graphene with superior interfacial contact and enhanced charge separation for photocatalytic hydrogen generation, ACS Appl. Mater. Inter. 6 (16) (2014) 13798–13806, https://doi.org/10.1021/am503244w.
[25] L. Liu, Z. Liu, A. Liu, X. Gu, C. Ge, F. Gao, L. Dong, Engineering the TiO_2-graphene interface to enhance photocatalytic H_2 production, ChemSusChem 7 (2) (2014) 618–626, https://doi.org/10.1002/cssc.201300941.
[26] H. Li, X. Cui, A hydrothermal route for constructing reduced graphene oxide/TiO_2 nanocomposites: Enhanced photocatalytic activity for hydrogen evolution, Int. J. Hydrogen Energy 39 (2014) 19877–19886, https://doi.org/10.1016/j.ijhydene.2014.10.010.
[27] H.-H. Chun, W.-K. Jo, Adsorption and photocatalysis of 2-ethyl-1-hexanol over graphene oxide–TiO_2 hybrids post-treated under various thermal conditions, Appl. Catal. B: Environ. 180 (2016) 740–750, https://doi.org/10.1016/j.apcatb.2015.07.021.
[28] Y. Zhang, X. Hou, T. Sun, X. Zhao, Calcination of reduced graphene oxide decorated TiO_2 composites for recovery and reuse in photocatalytic applications, Ceram. Int. 43 (1) (2017) 1150–1159, https://doi.org/10.1016/j.ceramint.2016.10.056.
[29] G. Colón, J.M. Sánchez-España, J.M. Hidalgo, J.A. Novío, Effect of TiO_2 acidic pre-treatment on the photocatalytic properties for phenol degradation, J. Photochem. Photobiol. A: Chem. 179 (2006) 20–27, https://doi.org/10.1016/j.jphotochem.2005.07.007.
[30] D. Chen, L. Zou, S. Li, F. Zheng, Nanospherical like reduced graphene oxide decorated TiO_2 nanoparticles: an advanced catalyst for the hydrogen evolution reaction, Sci. Rep. 6 (2016) 20335, https://doi.org/10.1038/srep20335.
[31] L. Martínez, M. Benito, I. Mata, L. Soler, E. Molins, J. Llorca, Preparation and photocatalytic activity of Au/TiO_2 lyogels for hydrogen production, Sustain. Energ. Fuels 2 (10) (2018) 2284–2295, https://doi.org/10.1039/C8SE00293B.
[32] J. Serafin, L. Soler, D. Vega, A. Rodríguez, J. Llorca, Macroporous silicon coated with M/TiO_2 (M=Au, Pt) as a highly efficient photoreactor for hydrogen production, Chem. Eng. J. 393 (2020), 124701, https://doi.org/10.1016/j.cej.2020.124701.
[33] Y. Li, P. Han, Y. Hou, S. Peng, X. Kuang, Oriented $Zn_mIn_2S_{m+3}$@In_2S_3 heterojunction with hierarchical structure for efficient photocatalytic hydrogen evolution, Appl. Catal., B (2019) 604–611, https://doi.org/10.1016/j.apcatb.2018.11.088.
[34] A.W. Morawski, E. Kusiak-Nejman, A. Wanag, J. Kapica-Kozar, R.J. Wróbel, B. Ohtani, M. Aksienionek, L. Lipińska, Photocatalytic degradation of acetic acid in the presence of visible light-active TiO_2-reduced graphene oxide photocatalysts, Catal. Today 280 (2017) 108–113, https://doi.org/10.1016/j.cattod.2016.05.055.
[35] E. Kusiak-Nejman, A. Wanag, Ł. Kowalczyk, J. Kapica-Kozar, C. Colbeau-Justin, M. G. Méndez-Medrano, A.W. Morawski, Graphene oxide-TiO_2 and reduced graphene oxide-TiO_2 nanocomposites: Insight in charge-carrier lifetime measurements, Catal. Today 287 (2017) 189–195, https://doi.org/10.1016/j.cattod.2016.11.008.
[36] E. Kusiak-Nejman, A. Wanag, Ł. Kowalczyk, M. Zgrzebnicki, B. Tryba, J. Przepiórski, Methylene blue decomposition on TiO2/reduced graphene oxide hybrid photocatalysts obtained by a two-step hydrothermal and calcination synthesis, Catal. Today, 2019, in press, doi.org/10.1016/j.cattod.2019.04.078.
[37] Y. Liu, Hydrothermal synthesis of TiO_2–RGO composites and their improved photocatalytic activity in visible light, RSC Adv. 4 (2014) 36040–36045, https://doi.org/10.1039/C4RA06342B.
[38] X. Rong, F. Qiu, C.h. Zhang, L. Fu, Y. Wang, D. Yang, Preparation, characterization and photocatalytic application of TiO_2-graphene photocatalyst under visible light irradiation, Ceram. Int. 41 (2015) 2502–2510, https://doi.org/10.1016/j.ceramint.2014.10.072.
[39] S. Sheshmani, M. Nayebi, Modification of TiO_2 with graphene oxide and reduced graphene oxide; enhancing photocatalytic activity of TiO_2 for removal of Remazol Black B, Polym. Compos. 40 (2019) 210–216, https://doi.org/10.1002/pc.24630.
[40] A. Ibrahim, W. Mekprasart, W. Pecharapa, Anatase/Rutile TiO_2 composite prepared via sonochemical process and their photocatalytic activity, Mater. Today: Proceedings 4 (2017) 6159–6165, https://doi.org/10.1016/j.matpr.2017.06.110.
[41] D.A.H. Hanaor, C.C. Sorrell, Review of the anatase to rutile phase transformation, J. Mater. Sci. 46 (4) (2011) 855–874, https://doi.org/10.1007/s10853-010-5113-0.
[42] D.A.H. Hanaor, M. Michelazzi, J. Chenu, C. Leonelli, C.C. Sorrell, The effects of firing conditions on the properties of electrophoretically deposited titanium dioxide films on graphite substrates, J. Eur. Ceram. Soc. 31 (2011) 2877–2885, https://doi.org/10.1016/j.jeurceramsoc.2011.07.007.
[43] L.L. Tan, W.J. Ong, S.P. Chai, A.B. Mohamed, Reduced graphene oxide-TiO_2 nanocomposite as a promising visible-light-active photocatalyst for the conversion of carbon dioxide, Nanoscale Res. Lett. 8 (2013) 465, https://doi.org/10.1186/1556-276X-8-465.
[44] D. Reyes-Coronado, G. Rodriguez-Gattorno, M.E. Espinosa-Pesqueira, C. Cab, R. de Coss, G. Oskam, Phase-pure TiO_2 nanoparticles: anatase, brookite and rutile, Nanotechnol. 19 (2008) 145605–145615, https://doi.org/10.1088/0957-4484/19/14/145605.
[45] Y.C. Wong, Y.P. Tan, Y.H. Taufiq-Yap, I. Ramli, Effect of calcination temperatures of CaO/Nb_2O_5 mixed oxides catalysts on biodiesel production, Sains Malays. 43 (2014) 783–790.
[46] M. Kim, W.H. Hong, W. Kim, S.H. Park, W.K. Jo, 2D reduced graphene oxide–titania nanocomposites synthesized under different hydrothermal conditions for treatment of hazardous organic pollutants, Particuology 36 (2018) 165–173, https://doi.org/10.1016/j.partic.2017.05.005.
[47] J. Yu, T. Ma, S. Liu, Enhanced photocatalytic activity of mesoporous TiO_2 aggregates by embedding carbon nanotubes as electron-transfer channel, Phys. Chem. Chem. Phys. 8 (2011) 3491–3501, https://doi.org/10.1039/c0cp01139h.
[48] G. Nagaraju, K. Manjunath, S. Sarkar, E. Gunter, Sergio R. Teixeira, J. Dupont, TiO2–RGO hybrid nanomaterials for enhanced water splitting reaction, Int. J. Hydrog. Energy. 40(36) (2015) 12209-12216, doi.org/10.1016/j.ijhydene.2015.07.094.
[49] J.M. Herrmann, Heterogeneous photocatalysis: fundamentals and application to the removal of various types of aqueous pollutants, Catal. Today 53 (1999) 115–129, https://doi.org/10.1016/S0920-5861(99)00107-8.
[50] W.R. Siah, H.O. Lintang, M. Shamsuddin, L. Yuliati, High photocatalytic activity of mixed anatase-rutile phases on commercial TiO2 nanoparticles, IOP Conf. Ser. Mater. Sci. Eng. 107 (2016) doi: 01200510.1088/1757-899X/107/1/012005.
[51] Y. Chen, L. Soler, C. Xie, X. Vendrell, J. Serafin, D. Crespo, J. Llorca, A straightforward method to prepare supported Au clusters by mechanochemistry and its application in photocatalysis, Appl. Mater. Today 21 (2020) 100873, https://doi.org/10.1016/j.apmt.2020.100873.
[52] C. Xing, Y. Liu, Y.u. Zhang, J. Liu, T. Zhang, P. Tang, J. Arbiol, L. Soler, K. Sivula, N. Guijarro, X. Wang, J. Li, R. Du, Y. Zuo, A. Cabot, J. Llorca, Porous $NiTiO_3$/TiO_2 nanostructures forphotocatatalytic hydrogen evolution, J. Chem. A. 7 (28) (2019) 17053–17059, https://doi.org/10.1039/C9TA04763H.
[53] W. Fan, Q. Lai, Q. Zhang, Y. Wang, nanocomposites of TiO_2 and reduced graphene oxide as efficient photocatalyst for hydrogen evolution, J. Phys. Chem. C 115 (2011) 10694–10701, https://doi.org/10.1021/jp2008804.
[54] H.-I. Kim, G.-H. Moon, D. Monllor-Satoca, Y. Park, W. Choi, Solar photoconversion using graphene/TiO_2 composites: nanographene shell on TiO_2 core versus TiO_2 nanoparticles on graphene sheet, J. Phys. Chem C 116 (1) (2012) 1535–1543, https://doi.org/10.1021/jp209035e.
[55] C. Han, Y. Wang, Y. Lei, B. Wang, N. Wu, Q. Shi, Q. Li, In situ synthesis of graphitic-C3N4 nanosheet hybridized N-doped TiO_2 nanofibers for efficient photocatalytic H2 production and degradation, Nano Res. 8 (4) (2015) 1199–1209, https://doi.org/10.1007/s12274-014-0600-2.
[56] J. Gong, C. Yang, J. Zhang, W. Pu, Origin of photocatalytic activity of W/N-codoped TiO2: H2 production and DFT calculation with GGA +U, Appl. Cat. B: Environ., 152-153 (2014) 73-81, doi:10.106/j.apcatb.2014.01.028.
[57] L. Kuang, W. Zhang, Enhanced hydrogen Production by carbon-doped TiO_2 Decorated with Reduced Graphene Oxide (rGO) under Visible Light Irradiation, ACS Adv. 6 (3) (2016) 2479–2488, https://doi.org/10.1039/C5RA26096E.
[58] X. Zhang, Y. Sun, X. Cui and Z. Jiang, A green and facile synthesis of TiO2/graphene nanocomposites and their photocatalytic activity for hydrogen evolution, Int. J. Hydrogen Energy, 37 (2012) 811-815, doi.org/10.106/j.ijhydene.2011.04.053.
[59] F. Pei, S. Xu, W. Zuo, Z. Zhang, Y. Liu, S. Cao, Effective improvement of photocatalytic hydrogen evolution via a facile in-situ solvothermal N-doping strategy in N-TiO2/N-graphene nanocomposite, 39 (2014) 6845-6852, doi.org/10.1016/j.ijhydene.2014.02.173.

Supplementary Material

for

Hydrogen photoproduction on TiO_2-reduced graphene oxide hybrid materials from water-ethanol mixture

Jarosław Serafin[1*], Ewelina Kusiak-Nejman[2·], Agnieszka Wanag[2], Antoni W. Morawski[2], Jordi Llorca[1]

[1]Institute of Energy Technologies, Department of Chemical Engineering and Barcelona Research Center in Multiscale Science and Engineering, Universitat Politècnica de Catalunya, EEBE, Eduard Maristany 10-14, 08019 Barcelona, Spain

[2]Department of Chemical and Environment Engineering, Faculty of Chemical Technology and Engineering, West Pomeranian University of Technology, Pulaskiego 10, 70-322Szczecin, Poland

Content

[*] Corresponding author

E-mail address: **jaroslaw.serafin@upc.edu** (J. Serafin); **ewelina.kusiak@zut.edu.pl** (E. Kusiak-Nejman)

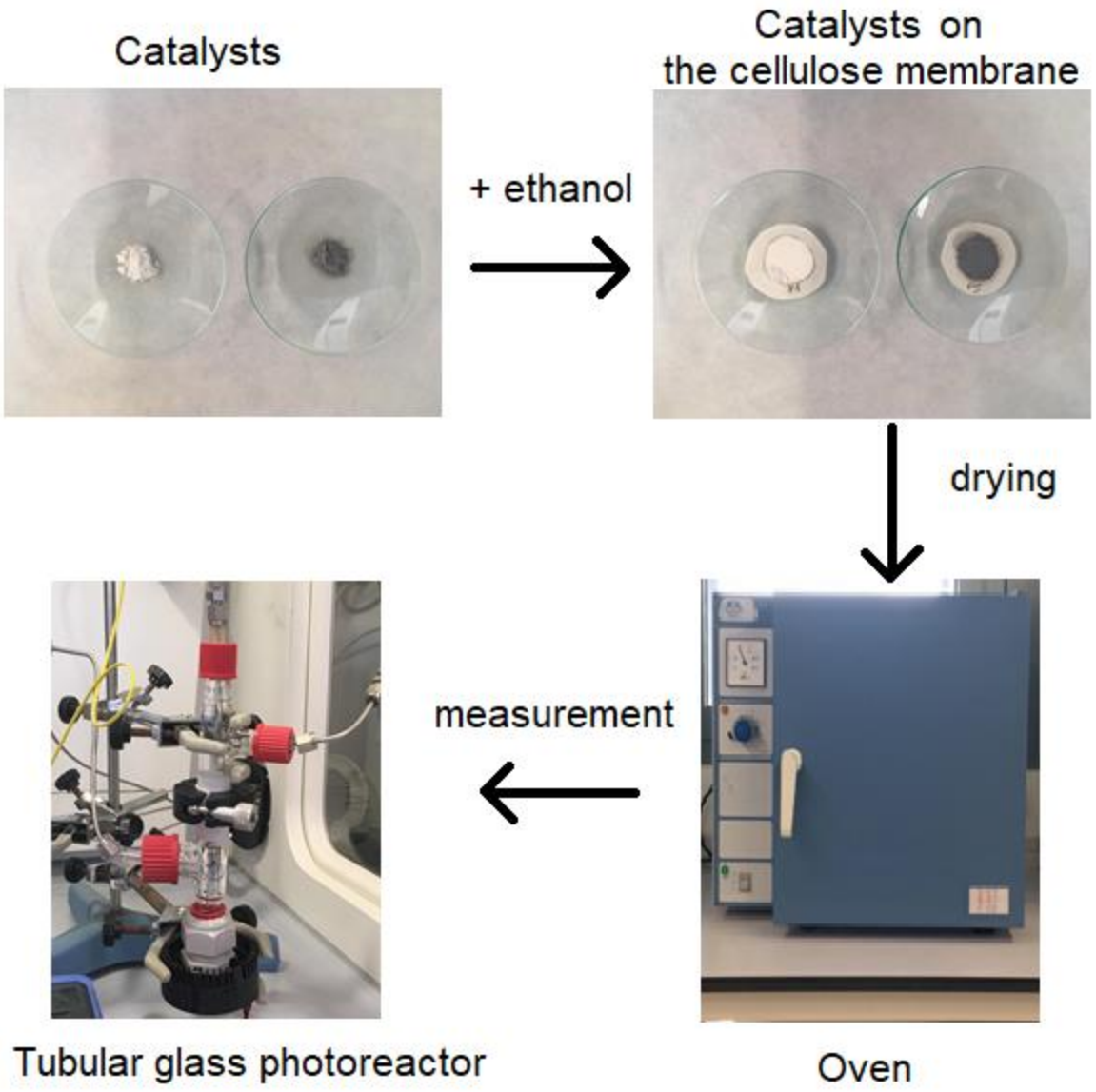

Figure S1. Schematic illustration of the preparation steps of photocatalysts for the photocatalytic tests

Table S1. Apparent quantum yield (AQY) obtained under UV light from the different samples.

Sample	**AQE [%]**
TiO_2	0.18
TiO_2-500	0.25
TiO_2-700	0.65
TiO_2-rGO-300	0.25
TiO_2-rGO-500	2.04
TiO_2-rGO-700	2.24
TiO_2-rGO-900	0.07

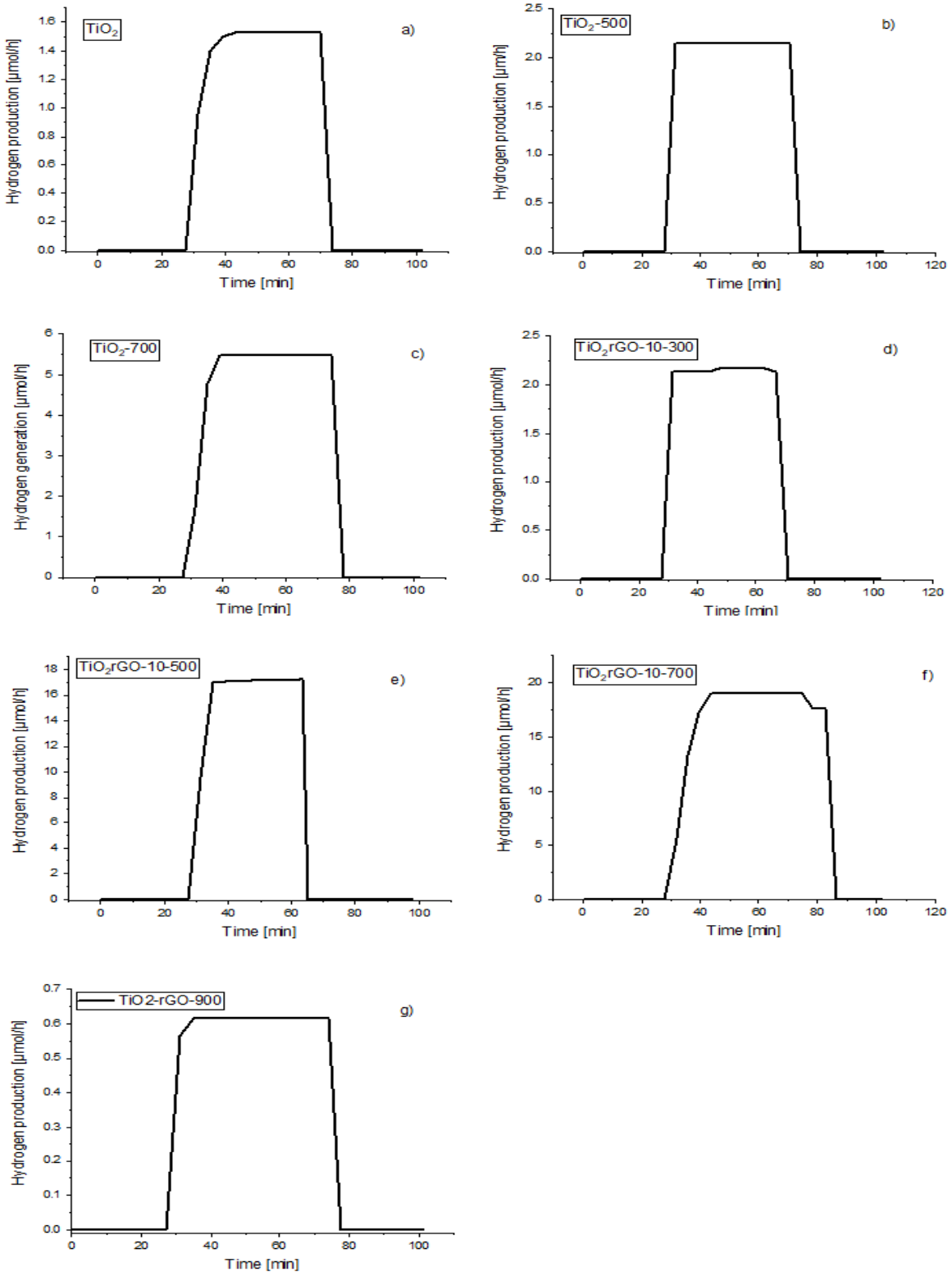

Figure S2. Hydrogen production over time for all catalysts.

Journal of Photochemistry & Photobiology, A: Chemistry 425 (2022) 113726

Contents lists available at ScienceDirect

Journal of Photochemistry & Photobiology, A: Chemistry

journal homepage: www.elsevier.com/locate/jphotochem

Photocatalytic hydrogen production from alcohol aqueous solutions over TiO_2-activated carbon composites decorated with Au and Pt

Jarosław Serafin [a,*], Mohammed Ouzzine [b], Joanna Sreńscek-Nazzal [c], Jordi Llorca [a]

[a] Institute of Energy Technologies, Department of Chemical Engineering and Barcelona Research Center in Multiscale Science and Engineering, Universitat Politècnica de Catalunya, EEBE, Eduard Maristany 16, 08019 Barcelona, Spain
[b] ERSIC Research Group, Department of Chemistry, Polydisciplinary Faculty, University of Sultan Moulay Slimane, Béni-Mellal, Morocco
[c] Department of Catalytic and Sorbent Materials Engineering, Faculty of Chemical Technology and Engineering, West Pomeranian University of Technology in Szczecin, Piastów Ave. 42, 71-065 Szczecin, Poland

ARTICLE INFO

Keywords:
Platinum
Gold
Titanium dioxide
Activated carbon
Composite
Hydrogen
Photocatalysis

ABSTRACT

Nanocomposites based on titanium dioxide loaded with metal nanoparticles (Au and Pt) and activated carbon were synthesized and tested for hydrogen photogeneration in the gas phase using a mixture of alcohol-water (methanol, ethanol, and bioethanol). The photocatalysts were characterized by BET, XRD, Raman spectroscopy, XPS, UV–vis, and transient photocurrent response measurements. The influence of the metal, the ratio of titanium oxide to active carbon, and the type of alcohol used in the reaction mixture on hydrogen photogeneration were investigated. The highest hydrogen photoproduction rate was obtained on the photocatalyst containing a weight ratio of 1:1 of activated carbon:TiO_2 and loaded with 1 wt% Pt, which was also the sample showing the highest transient photocurrent response.

1. Introduction

With increasing global warming and environmental pollution, the development of renewable energy sources is becoming more essential. Hydrogen is one of the most promising clean and sustainable energy carriers and produces only water as a by-product with no greenhouse gas emission [1]. Hydrogen has many attractive properties as an energy carrier such as high energy density (140 MJ/kg) [2].

Hydrogen can be produced from various renewable and non-renewable energy resources such as fossil fuels, especially steam reforming of methane [3], oil/naphtha reforming [4] and coal gasification [5], biomass processing [6], biological sources [7], water electrolysis [8], and photocatalytic routes [9]. The photocatalytic decomposition of alcohols such as methanol and ethanol and their mixtures with water (bioethanol) for the production of hydrogen appears to be one of the practical and low-cost technologies in the hydrogen-based energy system.

Among various semiconductor materials, titanium dioxide (TiO_2) has been widely used in photocatalysis due to its excellent oxidative capacity and chemical inertness, low price, non-toxicity and high efficiency with long-term stability [10,11]. One factor that affects photocatalytic efficiency is the rapid recombination of the electron-holes pairs responsible for the reactivity. In this regard, metal decoration seems to be a promising approach in which the potential improvement of the properties of the catalysts depends on the particular interaction between metal and TiO_2 [10,12,13].

Another factor that affects the photocatalytic activity is the surface area of the photocatalysts. To overcome these problems, much attention has been paid to the development of supported TiO_2 catalysts. Hence, researchers have attempted to support TiO_2 on different types of matrixes such as zeolites [14] and carbon materials such as carbon nanotubes [15], carbon nanofibers [16], and activated carbons (ACs) [12,17]. It has been reported that the presence of activated carbon in contact with TiO_2 helps because of its strong adsorption capacity and because it improves the transfer rate of the interfacial charge and reduces the recombination rate of holes and electrons [12]. Various methods are being used for the preparation of TiO_2-AC photocatalysts, such as chemical vapor deposition (CVD), precipitation, dip-coating, hydrolysis, and sol–gel. It is known that the structure of supported catalysts has a strong influence on the physicochemical properties of TiO_2-AC catalysts, which depends on the preparation method used (i.e., calcination treatment). In this work, we have prepared composite photocatalysts by combining Au/TiO_2 and Pt/TiO_2 with AC and tested their hydrogen photogeneration rate from gaseous methanol–water,

* Corresponding author.
E-mail address: jaroslaw.serafin@upc.edu (J. Serafin).

https://doi.org/10.1016/j.jphotochem.2021.113726
Received 31 August 2021; Received in revised form 29 November 2021; Accepted 9 December 2021
Available online 14 December 2021

ethanol–water and bioethanol mixtures. To the best of our knowledge, little information on the effect of combining AC and TiO_2-supported metal nanoparticles on the photocatalytic hydrogen production from aqueous alcohol solutions has been reported.

2. Material and methods

2.1. Catalysts synthesis

Composite materials were synthesized starting from commercial activated carbon from Gryfscand Company (Poland) and crude titanium dioxide slurry provided by Grupa Azoty Zakłady Chemiczne "Police" S. A. company (Poland). A solution of ammonia (25%, Avantor Performance Materials Poland S.A.) was added to the crude slurry until pH = 6.8, which after that was dried at 378 K for 24 h. The ammonia water solution was used to remove residual sulfuric acid by forming ammonium sulfate, which dissolves easily in water. This material was denoted as starting-TiO_2 and was used as reference in order to evaluate the influence of activated carbon. Nine TiO_2-AC composites were prepared by the sol–gel method. Titanium dioxide and activated carbon were mixed using a VH 8 powder mixer with different TiO_2:AC weight ratios of 0.5:1, 1:1 and 2:1, Then 1% wt. of Pt (Platinum(II) chloride, Alfa Aesar, 99.9%) or Au (Gold(III) acetate (Alfa Aesar, 99.9%)) metal was dispersed in an ethanolic solution under ultrasounds and was added using the incipient wetness impregnation (IWI) method. Also, two samples were prepared with only metal, Au-TiO_2 and Pt-TiO_2, using the same method (IWI). The composites were treated in a muffle furnace at a temperature of 573 K with a step of 2 K/min for a period of 4 h. Materials were labeled as M-x-TiO_2-AC, where "M" corresponds to the metal (Pt or Au), "x" to the weight ratio between TiO_2 and AC.

2.2. Catalysts characterization

The phase composition and the crystalline structure of the photocatalysts were characterized by X-ray diffraction (XRD) with a Bruker D8 diffractometer using Cu Kα radiation (λ = 1.5418 Å, 40 mA, 40 kV). The samples were scanned at 2θ angles ranging from 20 to 80° with a step size of 0.02° and a time constant of 1 s. X-ray photoelectron spectroscopy (XPS) was performed on a SPECS system equipped with a Phoibos 150 MCD-9 detector and an Al anode XR50 source operating at 150 W. CasaXPS program (Casa Software Ltd., UK) was used to evaluate the XPS data (Shirley type background). X-ray fluorescence spectroscopy (XRF) was performed on a Epsilon 3 PANalytical instrument. Scanning electron microscopy (SEM) images were obtained with a Zeiss Neon40 Crossbeam Station instrument equipped with a field emission source operated at 5.0 kV. The free software Fiji was used to measure the particle size distribution. UV–vis reflectance spectroscopy was measured on a Shimadzu UV3600 UV–vis/NIR apparatus. $BaSO_4$ was used as a reference standard. The spectra were recorded at room temperature in air within the range of 220–800 nm. The acquired diffuse reflectance spectra were converted to absorbance through the standard Kubelka-Munk function. The band gap energies (E_g) of the prepared samples were estimated from the UV–vis spectra by Tauc plots. Raman spectroscopy was carried out on a confocal Raman spectrometer (Renishaw in Via Qontor) equipped with a Leica DM2700M micro-scope over the range of 50 to 800 cm^{-1}. The textural characterization of the materials was based on the corresponding N_2 adsorption/desorption isotherms at 77 K, measured on a QUADRASORBevo apparatus. All samples were first degassed in vacuum for 12 h at 383 K before analysis. The BET specific surface area (S_{BET}) was determined from the nitrogen adsorption data within the 0.05–0.20 range of relative pressure. The total pore volume (V_{tot}) was determined on the basis of the adsorbed N_2 at a relative pressure $p/p_o = 0.99$ and the micropore volume (V_{mic}) was calculated by applying the Dubinin-Radushkevich equation using adsorption branches of the measured isotherm.

2.3. Photocatalytic tests

A suspension of 2 ± 0.01 mg of the photocatalyst in ethanol was deposited with a pipette on a cellulose paper (Albet, thickness 0.18 mm, pore size 35–40 μm, 80 $g.m^{-2}$), which was subsequently dried at 333 K for 1 h. Hydrogen photoproduction tests were carried out in continuous mode using a glass tube reactor as reported elsewhere [18,19]. The photoreactor was equipped with a UV light source containing four LEDs emitting at 365 ± 5 nm. A light irradiation of 82 mW cm^{-2} was measured directly with a UVA radiation monitor (Solar Light Co., model PMA 2110, spectral response 320–400 nm) and a radiometer (model PMA2200, Solar Light Co.). The irradiation area was S = 1.88 cm^2 [19]. Alcohol-water mixtures in a molar ratio of 9:1 were introduced into the photoreactor by bubbling Ar (20 mL min^{-1}) through a Drechsel bottle. Alcohols used in the experiment were ethanol from Scharlau, methanol from Fisher Chemical and bioethanol from Bioetanol de la Mancha, S.L. (5 ppm S, 1 ppm Cl, 0.4 ppm P). All experiments were performed at room temperature. The outlet of the photoreactor was monitored on-line with a gas microchromatograph (Agilent 490) equipped with MS 5 Å, Plot U and Stabilwax columns for the complete analysis of the products.

The apparent quantum yield (AQY) was calculated according to equation (1):

$$AQY = \frac{2n_{H2}}{n_p}\cdot 100 = \frac{nN_A}{E_T/E_P}\cdot 100 \quad (1)$$

where n_{H2} is the number of molecules of H_2 generated and n_p is the number of incident photons reaching the catalyst. The number of incident photons can be calculated by $n_p = E_T/E_p$, where E_T is the total energy reaching the catalyst and E_p is the photon energy. $E_T = P \times S \times t$, where P (W m^2) is the power density of the incident monochromatic light, S (m^2) is the irradiation area and t (s) is the duration of the incident light exposure. $E_p = hc/\lambda$, where h is the Planck's constant, c the speed of light and λ (m) is the wavelength of the incident monochromatic light. The number of hydrogen molecules can be calculated as $n_{H2} = n \times N_A$, where n are the H_2 mol evolved during the time of light exposure (t), and N_A is the Avogadro constant [20].

The efficiency of the conversion of light to chemical energy (η), or LTH (light-to-hydrogen), has been calculated with equation (2) [21,22]:

$$\eta(\%) = \frac{r_{H_2}\cdot x\Delta G}{I_{rad}\cdot Area}\cdot 100 \quad (2)$$

where, r_{H_2} is the production rate of H_2, ΔG is the Gibbs free energy (237 kJ mol^{-1}), I_{rad} is the incident power and Area corresponds to the illuminated catalytic surface.

2.4. Photoelectrochemical measurements

The photoelectrochemical properties were studied by recording the transient photocurrent responses. A Bio-logic Sp-200 (Bio-Logic Science Instruments, France) potentiostat/galvanostat in a three-electrode cell (volume 100 mL) with 25 mL of 0.5 M Na_2SO_4 electrolyte (pH = 7.0) was used. The working electrode consisted on the catalyst loaded onto fluorine-doped tin oxide (FTO) glass. To that end, FTO was first washed with ethanol and acetone. Then, 15 ± 0.01 mg of photocatalyst was dispersed in 15 mL of ethanol using ultrasounds for 30 min and the suspension was deposited on the FTO glass using the spin-coating method and dried at room temperature. An Ag/AgCl (3.5 M) electrode (+0.205 V vs. NHE at 298 K) was used as a reference electrode and a Pt

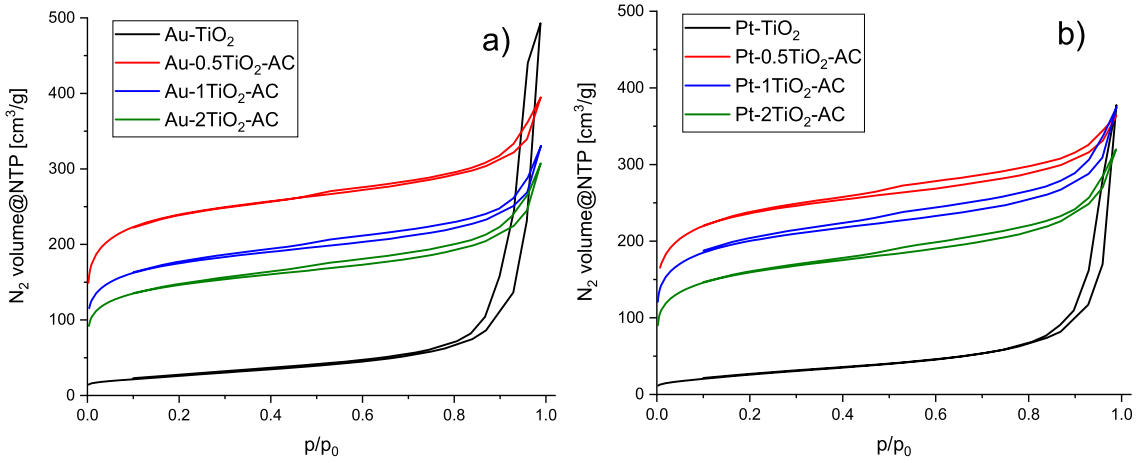

Fig. 1. N_2 adsorption/desorption of samples (a) Au-xTiO_2-AC and (b) Pt-xTiO_2-AC.

Table 1
Physical characteristics of the M-xTiO_2-AC photocatalysts.

Sample	S_{BET} [m^2/g]	V_{tot} [cm^3/g]	V_{mic} [cm^3/g]	Eg (eV)
TiO_2	98	0.27	–	3.01
AC	1284	0.76	0.42	–
0.5TiO_2-AC	867	0.56	0.29	2.88
1TiO_2-AC	707	0.46	0.23	2.93
2TiO_2-AC	583	0.38	0.19	3.05
Au-TiO_2	95	0.21	–	2.99
Au-0.5TiO_2-AC	803	0.61	0.25	2.88
Au-1TiO_2-AC	589	0.51	0.18	2.93
Au-2TiO_2-AC	483	0.48	0.14	3.05
Pt-TiO_2	98	0.22	–	2.80
Pt-0.5TiO_2-AC	793	0.56	0.25	2.94
Pt-1TiO_2-AC	675	0.58	0.20	2.80
Pt-2TiO_2-AC	541	0.50	0.15	2.92

Table 2
Elemental composition of the samples determined from XRF.

Sample	K [%]	Ti [%]	Fe [%]	Au [%]	Ca [%]	Pt [%]
TiO_2	0	76.35	0	0	0	0
AC	0.005	0	0.100	0	0.053	0
0.5TiO_2-AC	0.001	67.09	0.003	0	0.045	0
1TiO_2-AC	0.001	74.37	0.002	0	0.034	0
2TiO_2-AC	0.001	77.48	0.002	0	0.026	0
Pt-0.5TiO_2-AC	0.001	68.87	0.002	0	0	1.08
Pt-1TiO_2-AC	0.001	75.36	0.002	0	0	1.08
Pt-2TiO_2-AC	0.001	81.62	0.002	0	0	1.03
Au-0.5TiO_2-AC	0.001	68.73	0.003	1.07	0	0
Au-1TiO_2-AC	0.001	74.31	0.002	1.01	0	0
Au-2TiO_2-AC	0.001	79.88	0.002	1.01	0	0
Au-TiO_2	0	85.30	0.003	1.07	0	0
Pt-TiO_2	0	86.08	0.003	0	0	1.02

wire was used as a counter electrode (~3.6 cm^2). Transient photocurrent responses were recorded at a bias potential of 10 mV versus OCP during repeated on/off UV light cycles with intervals of 20 s.

3. Results and discussion

3.1. Characterization

The nitrogen adsorption–desorption isotherms at 77 K for the activated carbons and composite materials are shown in Fig. 1. The porosity of the selected carbon precursor exhibits a type (I + IV) profile. It has a round knee, which suggests the presence of microporosity, and an important slope at higher relative pressures, which indicates the presence of significant mesoporosity, confirmed by the hysteresis cycle. The N_2 adsorption–desorption isotherms of the AC, TiO_2, and composite M-xTiO_2-AC samples are presented in Fig. 1a and b. The adsorption capacity of the prepared samples decreased with increasing the TiO_2 content in M-xTiO_2-AC, indicating that partial coverage or blocking of the pores with increasing TiO_2 contents is taking place.

These changes in porosity caused by the sol–gel method followed by IWI impregnation are quantified in Table 1 in terms of apparent BET surface area and pore volumes (micro and total). As an example, the specific surface area of AC (1284 m^2/g) is higher than those of the composite materials Au-0.5TiO_2-AC, Au-1TiO_2-AC and Au-2TiO_2-AC (803, 589 and 483 m^2/g, respectively). Similarly, the total pore volumes of the hybrid materials M-xTiO_2-AC (V_{tot} = 0.61 cm^3/g for Au-0.5TiO_2-AC) are lower than that of the carbon support AC (0.76 cm^3/g), indicating that some pores are covered or blocked by TiO_2.

The band gap energy values (E_g) estimated from Tauc plots are included in Table 1. TiO_2 shows an E_g value of 3.01 eV, which is accordance with values reported in the literature [23]. The TiO_2-AC composites exhibit E_g values slightly lower, particularly at low TiO_2 content. This suggests an intimate contact between AC and TiO_2 nanoparticles. Table 2 shows the elemental composition of the samples determined by XRF spectroscopy. Samples containing AC showed trace amounts of potassium, iron and calcium. This is due to the fact that the activated carbon used in these studies comes from biomass precursor.

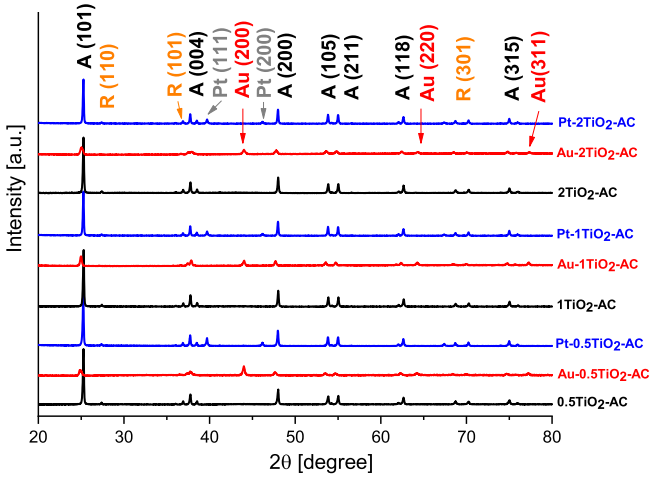

Fig. 2. XRD patterns. A and R refer to anatase and rutile, respectively.

The results obtained by the analysis of X-ray diffraction are shown in

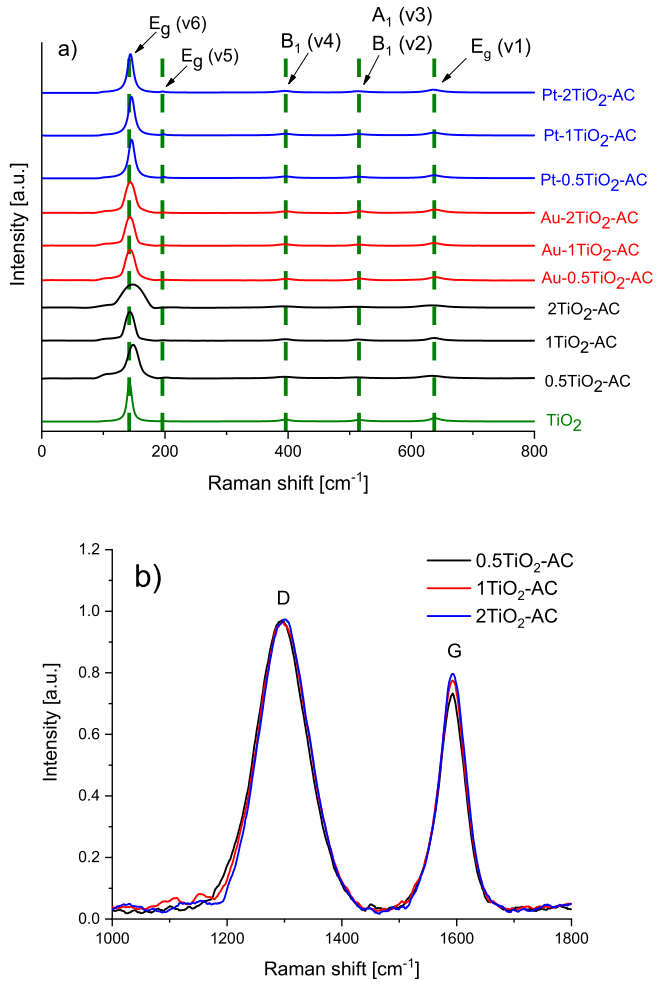

Fig. 3. Raman spectra.

Fig. 2. XRD patterns exhibited strong diffraction peaks of anatase (2θ at 25.3° (101), 37.8° (004), 48.1° (200), 53.8° (105), 55.0° (211), 62.6° (204), 68.9° (116), 70.2° (220) and 74.9° (315); JCPDS card N° 01-071-1167) and weak diffraction peaks of rutile (2θ at 27.4° (110) and 36.08° (200); JCPDS card N° 21–1276) [21]. As expected, AC did not show diffraction peaks due to its amorphous structure. The diffraction peaks at 44.4° (200), 64.6° (220) and 77.6° (311) correspond to the Au with a face-centered cubic (fcc) structure [24], and those at 39.8° and 46.2° correspond to cubic Pt (PDF N° 04-0802).

Raman spectra of $xTiO_2$-AC and M-$xTiO_2$-AC hybrid materials are shown in Fig. 3. According to the XRD results, all photocatalysts showed the characteristic Raman active modes of anatase at 144.4 [E_g(v6)], 196.2 [E_g(v5)], 400.4 [B_1(v4)], 514.9 [A_1(v3), B_1(v2)], and 637.5 cm^{-1} [E_g(v1)], whereas rutile phase was not observed due to its poor scattering efficiency. The most intense peak at 144.4 cm^{-1} corresponds to the external vibration of the Ti − O bond of the anatase phase of TiO_2. The position of this peak shifted from 144.4 cm^{-1} for pure TiO_2 up to150.0 cm^{-1} for the composite samples (Fig. 3a). This indicates that TiO_2-AC composites likely contain Ti^{3+} species and oxygen vacancies. Similar results were obtained by Zhang et al. [25]. For the TiO_2-AC composites, two peaks characteristic for carbon materials are also visible at around 1320–1350 cm^{-1} (D band) and 1595 cm^{-1} (G band) (Fig. 3b). These peaks are characteristic of graphitized structures. The I_D/I_G intensity ratio oscillated between 1.21 and 1.33, and this ratio increased as the amount of TiO_2 increased. This fact suggests the occurrence of significant changes in the structure of the activated carbon due to the contact between titanium oxide and the carbonaceous matrix and the formation of more sp^3 defects [26,27].

The distribution of TiO_2 nanoparticles on the surface of AC was studied by SEM. A heterogeneous distribution of the TiO_2 nanoparticles on the surface of the AC was detected. As can be seen in Fig. 4a, the titanium oxide is deposited in the form of spherical particles on the surface of the activated carbon. Additionally, the distribution of Pt and/or Au nanoparticles for each sample was analyzed by SEM using a

Table 3
Surface atomic ratios determined by XPS.

Sample	Ti/C	Pt/Ti
Pt-TiO_2	–	0.02
Pt-0.5TiO_2-AC	0.09	0.01
Pt-1TiO_2-AC	0.20	0.01
Pt-2TiO_2-AC	0.26	0.02

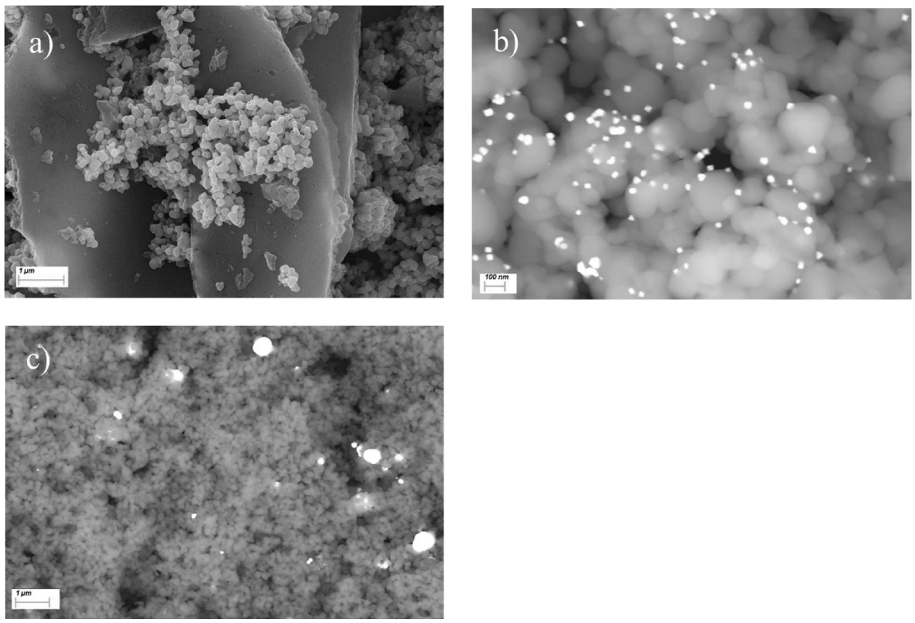

Fig. 4. SEM images of 1TiO_2-AC (a), Pt-1TiO_2-AC (b) and Au-1TiO_2-AC (c).

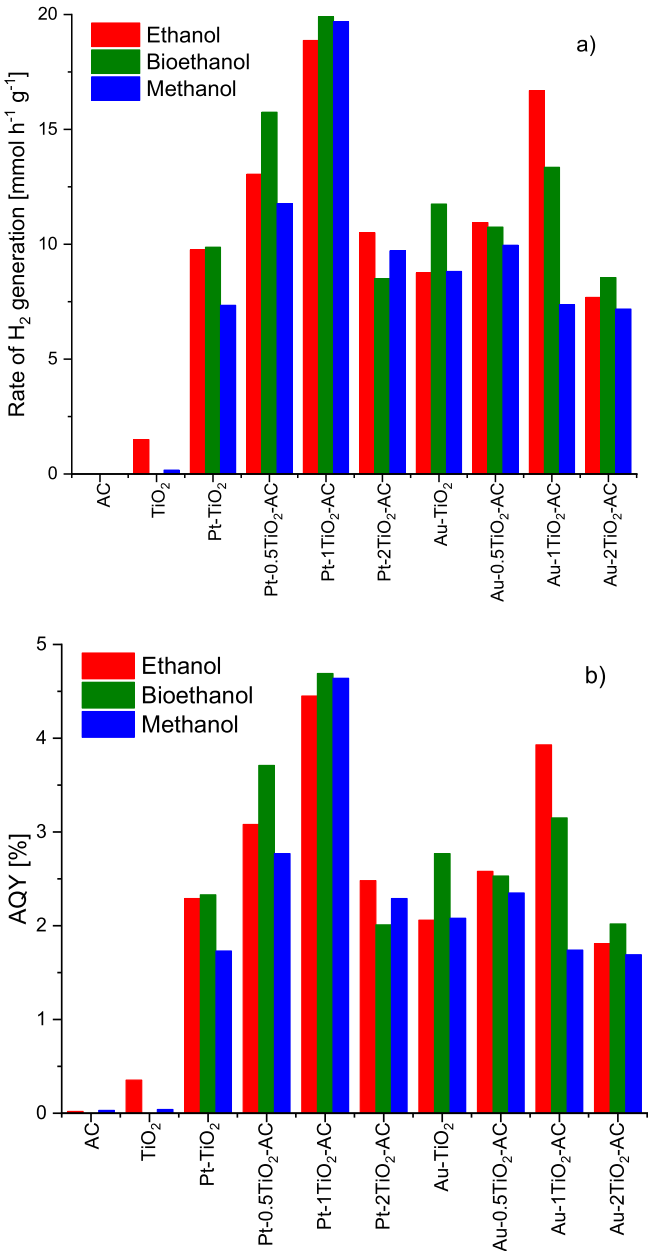

Fig. 5. Hydrogen photogeneration rates (a) and apparent quantum yield (AQY) values (b).

backscattered electron detector. The Pt-1TiO_2-AC sample (Fig. 4b) exhibited a homogeneous distribution of Pt nanoparticles with a similar particle size of about 20 nm. In contrast, the Au-1TiO_2-AC sample (Fig. 4c) exhibited a distribution of Au nanoparticles and agglomerates ranging from 20 up to 500 nm.

The surface composition of the samples containing Pt was measured by X-ray photoelectron spectroscopy (XPS) and is compiled in Table 3. The Ti/C surface atomic ratio progressively increased following an increase of the Pt-TiO_2 content in the composite material, from 0.09 for Pt-0.5TiO_2-AC up to 0.26 for Pt-2TiO_2-AC. Since these values are very similar to the nominal Ti/C atomic ratio of the sample (0.08, 0.15 and 0.30 for Pt-0.5TiO_2-AC, Pt-1TiO_2-AC and Pt-2TiO_2-AC, respectively), this suggests a good dispersion of the titania nanoparticles on the surface of the activated carbon. On the other hand, the surface Pt/Ti atomic ratio was in all cases 0.01–0.02, close to the nominal ratio (1 wt% Pt). For all samples, the Ti 2p signals recorded at 459.7 and 465.3 eV (Ti $2p_{3/2}$ and Ti $2p_{1/2}$, respectively) correspond well to Ti(IV) species in TiO_2.

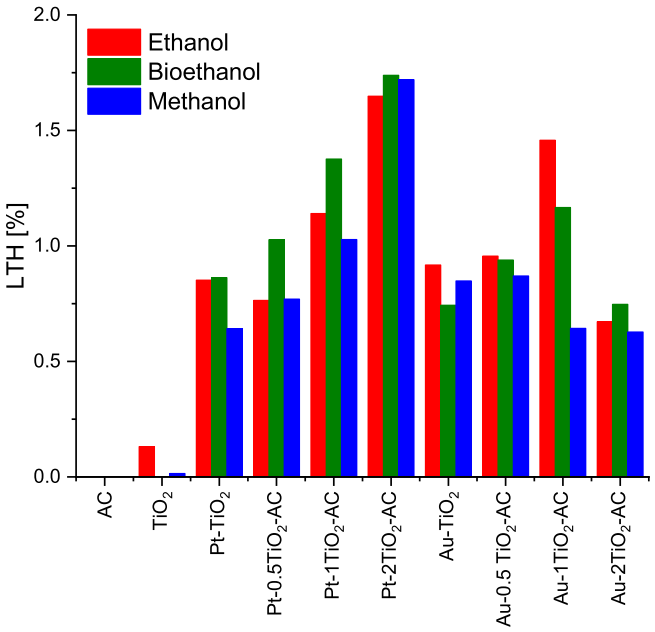

Fig. 6. The efficiency of light-to-hydrogen (LTH) energy conversion.

3.2. Photocatalytic tests

The photocatalysts were evaluated for hydrogen photoproduction in a continuous mode using UV irradiation at room temperature from gaseous ethanol:water, bioethanol:water and methanol:water in a molar ratio of 1:9. Experiments in the absence of light did not generate hydrogen, as expected. Hydrogen was produced from the dehydrogenation of the alcohol, as deduced from the quantification of the reaction products (only hydrogen and the aldehyde corresponding to the alcohol used).

Fig. 5 shows the hydrogen photogeneration rates and apparent quantum yield (AQY) values for each sample and alcohol used. It is important to highlight that the hydrogen photogeneration rates were stable in all cases for the duration of the experiments (S1-3). Pure TiO_2 was the reference sample and showed a hydrogen production rate of 1.5 mmol $h^{-1}g^{-1}$ and AQY of 0.26 % for ethanol–water and negligible for methanol–water due to the rapid recombination of photoexcited electron-hole pairs [28]. The highest H_2 production rate was achieved with the Pt-1TiO_2-AC sample and it was in the range of 19–20 mmol $h^{-1}g^{-1}$ for all the mixtures tested (around 4.5% AQY). The benefit in terms of hydrogen photoproduction rate of the composite photocatalysts containing TiO_2-AC with respect to TiO_2 is evident. It is believed that activated carbon improves the hydrogen generation due to its electron acceptor and transferring capability and inhibition of the recombination of photo-excited electrons and holes. The higher activity of the composite photocatalysts is attributed to the better charge separation achieved in these catalysts, with Pt particles being good electron scavengers as well as catalytic surfaces for the formation of hydrogen. The optimum composition of the photocatalyst is TiO_2:AC = 1:1. The hydrogen photoproduction rates obtained in this work are remarkably higher than those reported in the literature for similar systems. In particular, Hakamizadeh et al. [29] used a 0.75%Pt/TiO_2/AC photocatalyst in an aqueous solution of methanol under UV light irradiation and obtained a H_2 production of approximately 7.5 mmol $h^{-1}g^{-1}$. It is concluded that the simultaneous presence of active carbon and metal nanoparticles deposited on the surface of titanium oxide increases hydrogen production. A lower Fermi level characterizes platinum and gold compared to TiO_2. Therefore, the electron produced from TiO_2 as a result of UV radiation is transferred to metal particles loaded on the TiO_2 surface, where proton species are reduced into H_2 molecules [30].

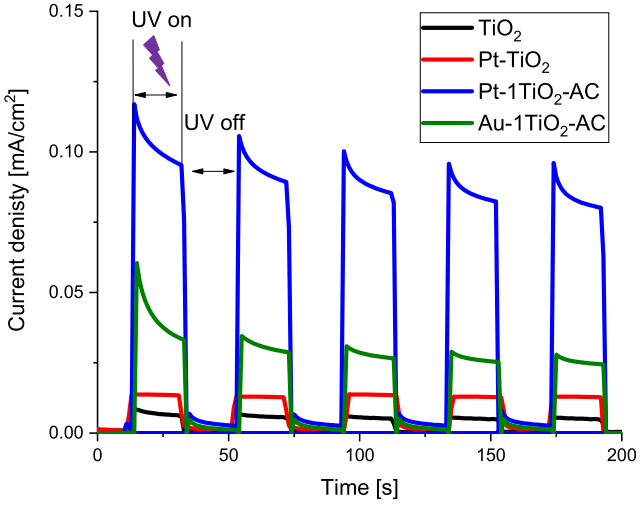

Fig. 7. Transient Photocurrent response (λ = 365 nm) of TiO_2, Pt-TiO_2, Pt-1TiO_2-AC and Au-1TiO_2-AC.

Fig. 6 shows the corresponding light-to-hydrogen (LTH) conversion efficiency. The highest LTH was obtained for Pt-1TiO_2-AC sample and was ca. 1.7 % depending on the alcohol-water mixture. The LTH value is a parameter that measures the efficiency of solar energy conversion. It shows the potential of the practical application under the conditions of irradiation with sunlight. As Cao and Piao recalls that the United States Department of Energy estimated that photocatalytic H_2 production from water splitting makes sense when hydrogen price is $ 2.00–4.00 kg^{-1}, which requires an LTH of 10 % or more. On the other hand, when determining the LTH parameter, the mass of the photocatalyst is not taken into account, which makes it impossible to compare for systems using different masses of the photocatalyst rationally. The highest LTH was obtained for the Pt-1TiO_2-AC sample and was 1.65–1.74 % for 2 mg of catalyst depending on the alcohol-water mixture.

Transient photocurrent measurements were performed to analyze the formation of electron-hole pairs as well as the electron transfer efficiency [22,31] for TiO_2, Pt-TiO_2, Pt-1TiO_2-AC and Au-1TiO_2-AC (Fig. 7). It is clear that an intense photoelectric current characterized the Pt-1TiO_2-AC sample, which indicates that the photogenerated electrons and holes in this sample moved much faster than in the other photocatalysts, leading to an increased photocatalytic H_2 production with respect to the other photocatalysts. The lower photocurrent observed for the Au-1TiO_2-AC sample with respect to Pt-1TiO_2-AC is likely due to the poor dispersion of Au nanoparticles, as deduced from SEM analysis (Fig. 4). In any case, the samples containing both TiO_2-supported metal nanoparticles and AC showed a remarkably higher photocurrent response and hydrogen photoproduction rate than the Pt-TiO_2 and Au-TiO_2 samples without AC and the bare TiO_2 sample, which indicates the existence of a strong cooperative effect between TiO_2 loaded with metal nanoparticles and AC.

4. Conclusions

A series of M-TiO_2-AC (M = Pt, Au) composite photocatalysts were prepared, characterized and tested for the photoproduction of hydrogen from alcohol-water mixtures in gas phase and in continuous mode (methanol–water, ethanol–water and commercial bioethanol-water). The highest value of hydrogen production was obtained with the Pt-1TiO_2-AC catalyst, with values of about 19–20 mmol $h^{-1}g^{-1}$, followed by Au-1TiO_2-AC. These values are remarkable higher than those obtained separately over Pt-TiO_2, Au-TiO_2 and TiO_2. The better photocatalytic activity exhibited by the M-TiO_2-AC composites is ascribed to an enhanced electron transport and electron-hole pair lifetime as deduced from transient photocurrent response experiments.

CRediT authorship contribution statement

Jarosław Serafin: Conceptualization, Methodology, Validation, Formal analysis, Data curation, Investigation, Writing – original draft, Writing – review & editing, Visualization, Project administration, Supervision. **Mohammed Ouzzine:** Formal analysis, Writing – original draft, Writing – review & editing. **Joanna Sreńscek-Nazzal:** Resources, Investigation, Validation. **Jordi Llorca:** Funding acquisition, Resources, Writing – review & editing.

Declaration of Competing Interest

The authors declare that they have no competing financial interests or personal relationships that could have appeared to influence the work reported in this paper.

Acknowledgements

This work has been funded by projects MICINN/FEDER RTI2018-093996-B-C31 and GC 2017 SGR 128. JL is a Serra Húnter Fellow and is grateful to ICREA Academia program.

Appendix A. Supplementary data

Supplementary data to this article can be found online at https://doi.org/10.1016/j.jphotochem.2021.113726.

References

[1] A.V. Puga, Review: Photocatalytic production of hydrogen from biomass-derived feedstocks, Coordination Chem. Rev. 315 (2016) 1–66, https://doi.org/10.1016/j.ccr.2015.12.009.
[2] J. Chi, H. Yu, Water electrolysis based on renewable energy for hydrogen production, Chin. J. Catal. 39 (3) (2018) 390–394, https://doi.org/10.1016/S1872-2067(17)62949-8.
[3] A. Boyano, A.M. Blanco-Marigorta, T. Morosuk, G. Tsatsaronis, Exergo-environmental analysis of a steam methane reforming process for hydrogen production, Energy 36 (4) (2011) 2202–2214, https://doi.org/10.1016/j.energy.2010.05.020.
[4] D. Iranshahi, E. Pourazadi, K. Paymooni, M.R. Rahimpour, A. Jahanmiri, B. Moghtaderi, A dynamic membrane reactor concept for naphtha reforming, considering radial flow patterns for both sweeping gas and reacting materials, Chem. Eng. J. 178 (2011) 264–275, https://doi.org/10.1016/j.cej.2011.08.005.
[5] S.S. Seyitoglu, I. Dincer, A. Kilicarslan, Energy and exergy analyses of hydrogen production by coal gasification, Int. J. Hydrogen Energy 42 (4) (2017) 2592–2600, https://doi.org/10.1016/j.ijhydene.2016.08.228.
[6] Y. Kalinci, A. Hepbasli, I. Dincer, Biomass-based hydrogen production: A review and analysis, Int. J. Hydrogen Energy 34 (21) (2009) 8799–8817, https://doi.org/10.1016/j.ijhydene.2009.08.078.
[7] D.B. Levin, L. Pitt, M. Love, Biohydrogen production: prospects and limitations to practical application, Int. J. Hydrogen Energy 29 (2004) 173–185, https://doi.org/10.1016/S0360-3199(03)00094-6.
[8] S. Siracusano, V. Baglio, N. Briguglio, G. Brunaccini, A. Di Blasi, A. Stassi, R. Ornelas, E. Trifoni, V. Antonucci, A.S. Aricò, An electrochemical study of a PEM stack for water electrolysis, Int. J. Hydrogen Energy 37 (2) (2012) 1939–1946, https://doi.org/10.1016/j.ijhydene.2011.06.019.
[9] L.M. Ahmed, A.F. Alkaim, A.F. Halbus, F.H. Hussein, Photocatalytic hydrogen production from aqueous methanol solution over metallized TiO_2, Int. J. Chem. Tech. Res. 9 (2016) 90–98.
[10] M. Ouzzine, M.A. Lillo-Ródenas, A. Linares-Solano, Photocatalytic oxidation of propene in gas phase at low concentration by optimized TiO_2 nanoparticles, Appl. Catal. B Environ. 134–135 (2013) 333–343, https://doi.org/10.1016/j.apcatb.2013.01.035.
[11] M. Ouzzine, A.J. Romero-Anaya, M.A. Lillo-Rodenas, A. Linares-Solano, Spherical activated carbon as an enhanced support for TiO_2/AC photocatalysts, Carbon 67 (2014) 104–118, https://doi.org/10.1016/j.carbon.2013.09.069.
[12] F. Li, Q. Gu, Y. Niu, R. Wang, Y. Tong, S. Zhu, H. Zhang, Z. Zhang, X. Wang, Hydrogen evolution from aqueous-phase photocatalytic reforming of ethylene glycol over Pt/TiO_2 catalysts: Role of Pt and product distribution, Appl. Surface Sci. 391 (2017) 251–258, https://doi.org/10.1016/j.apsusc.2016.06.046.
[13] J. Serafin, L. Soler, D. Vega, Á. Rodríguez, J. Llorca, Macroporous silicon coated with M/TiO_2 (M= Au, Pt) as a highly efficient photoreactor for hydrogen

production, Chem. Eng. J. 393 (2020) 124701, https://doi.org/10.1016/j.cej.2020.124701.
[14] T. Hisanaga, K. Tanaka, Photocatalytic degradation of benzene on zeolite-incorporated TiO_2 film, J. Hazard Mater 93 (3) (2002) 331–337, https://doi.org/10.1016/S0304-3894(02)00050-X.
[15] N. Bouazza, M. Ouzzine, M.A. Lillo-Ródenas, D. Eder, A. Linares-Solano, TiO_2 nanotubes and CNT–TiO_2 hybrid materials for the photocatalytic oxidation of propene at low concentration, Appl. Catal. B 92 (3-4) (2009) 377–383, https://doi.org/10.1016/j.apcatb.2009.08.017.
[16] M. Ouzzine, M.A. Lillo-Rodenas, A. Linares-Solano, Carbon nanofibres as substrates for the preparation of TiO_2 nanostructured photocatalysts, Appl. Catal. B 127 (2012) 291–929, https://doi.org/10.1016/j.apcatb.2012.08.029.
[17] Y. Li, X. Li, J. Li, J. Yin, Photocatalytic degradation of methyl orange by TiO_2-coated activated carbon and kinetic study, Water Res. 40 (6) (2006) 1119–1126, https://doi.org/10.1016/j.watres.2005.12.042.
[18] L. Martínez, L. Soler, I. Angurell, J. Llorca, Effect of TiO_2 Nanoshape on the Photoproduction of Hydrogen from water-ethanol mixtures over Au_3Cu/TiO_2 Prepared with Preformed Au-Cu Alloy Nanoparticles, Appl. Catal. B Environ. 248 (2019) 504–514, https://doi.org/10.1016/j.apcatb.2019.02.053.
[19] J. Serafin, E. Kusiak-Nejman, A. Wanag, A.W. Morawski, J. Llorca, Hydrogen photoproduction on TiO_2-reduced graphene oxide hybrid materials from water-ethanol mixture, J Photochem. Photobiol. A 418 (2021) 113406, https://doi.org/10.1016/j.jphotochem.2021.113406.
[20] Y. Li, P. Han, Y. Hou, S. Peng and X. Kuang, Oriented $Zn_mIn_2Sm_{+3}$@ In_2S_3 heterojunction with hierarchical structure for efficient photocatalytic hydrogen evolution, Appl. Catal., B, 244 (2019) 604-611. doi.org/10.1016/j.apcatb.2018.11.088.
[21] C. Jiang, S.J.A. Moniz, A. Wang, T. Zhang, J. Tang, Photoelectrochemical devices for solar water splitting – materials and challenges, Chem. Soc. Rev. 46 (15) (2017) 4645–4660, https://doi.org/10.1039/c6cs00306k.
[22] S. Cao, L. Piao, Considerations for a More Accurate Evaluation Method for Photocatalytic Water Splitting, Angewandte Chemie International Edition 59 (42) (2020) 18312–18320, https://doi.org/10.1002/anie.202009633.
[23] L. Shen, N.Z. Bao, Y.N. Zheng, A. Gupta, T.C. An, K. Yanagisawa, Hydrothermal Splitting of Titanate Fibers to Single-Crystalline TiO_2 Nanostructures with Controllable Crystalline Phase, Morphology, Microstructure, and Photocatalytic Activity, J. Phys. Chem. C. 112 (2008) 8809–8818, https://doi.org/10.1021/jp711369e.
[24] S. Musić, M. Gotić, M. Ivanda, S. Popović, A. Turković, R. Trojko, A. Sekulić, K. Furić, Chemical and microstructural properties of TiO_2 synthesized by sol-gel procedure, Mater. Sci. Eng. B 47 (1) (1997) 33–40, https://doi.org/10.1016/S0921-5107(96)02041-7.
[25] X. Zhang, L. Luo, R. Yun, M. Pu, B. Zhang, X. Xiang, Increasing the Activity and Selectivity of TiO2-Supported Au Catalysts for Renewable Hydrogen Generation from Ethanol Photoreforming by Engineering Ti^{3+} Defects, ACS Sustainable Chem. Eng. 7 (16) (2019) 13856–13864, https://doi.org/10.1021/acssuschemeng.9b02008.
[26] D.L.C.e. Silva L.R.P. Kassab A.D.D. Santos M.F. Pillis Evaluation of Carbon thin Films Using Raman Spectroscopy Mat. Res. 21 4 10.1590/1980-5373-mr-2017-0787.
[27] L.-L. Qu, N.a. Wang, Y.-Y. Li, D.-D. Bao, G.-H. Yang, H.-T. Li, Novel titanium dioxide-graphene-activated carbon ternary nanocomposites with enhanced photocatalytic performance in rhodamine B and tetracycline hydrochloride degradation, J. Mater. Sci. 52 (13) (2017) 8311–8320, https://doi.org/10.1007/s10853-017-1047-0.
[28] Y. Chen, L. Soler, C. Xie, X. Vendrell, J. Serafin, D. Crespo, J. Llorca, A straightforward method to prepare supported Au clusters by mechanochemistry and its application in photocatalysis, Appl. Mater. Today 21 (2020), 100873, https://doi.org/10.1016/j.apmt.2020.100873.
[29] M. Hakamizadeh, S. Afshar, A. Tadjarodi, R. Khajavian, M.R. Fadaie, B. Bozorgi, Improving hydrogen production via water splitting over Pt/TiO_2/activated carbon nanocomposite, J. Hydr. Ener. 39 (14) (2014) 7262–7269, https://doi.org/10.1016/j.ijhydene.2014.03.048.
[30] R. Abe, K. Sayama, H. Arakawa, Significant effect of iodide addition on water splitting into H_2 and O_2 over Pt-loaded TiO_2 photocatalyst: suppression of backward reaction, Chem. Phys. Lett. 371 (3-4) (2003) 360–364, https://doi.org/10.1016/S0009-2614(03)00252-5.
[31] W. Gao, J. Lu, S. Zhang, X. Zhang, Z. Wang, W. Qin, J. Wang, W. Zhou, H. Liu, Y. Sang, Suppressing Photoinduced Charge Recombination via the Lorentz Force in a Photocatalytic System, Adv. Sci. 6 (18) (2019) 1901244, https://doi.org/10.1002/advs.201901244.

Supplementary Material

for

Photocatalytic hydrogen production from alcohol aqueous solutions over TiO_2-activated carbon composites decorated with Au and Pt

Jarosław Serafin[1*], Mohammed Ouzzine[2], Joanna Sreńscek-Nazzal[3], Jordi Llorca[1]

[1]Institute of Energy Technologies, Department of Chemical Engineering and Barcelona Research Center in Multiscale Science and Engineering, Universitat Politècnica de Catalunya, EEBE, Eduard Maristany 10-14, 08019 Barcelona, Spain

[2]ERSIC research group, Department of Chemistry, Polydisciplinary Faculty, University of Sultan Moulay Slimane, Béni-Mellal, Morocco

[3]Department of Catalytic and Sorbent Materials Engineering, Faculty of Chemical Technology and Engineering, West Pomeranian University of Technology in Szczecin, Piastów Ave. 42, 71-065 Szczecin, Poland

Content

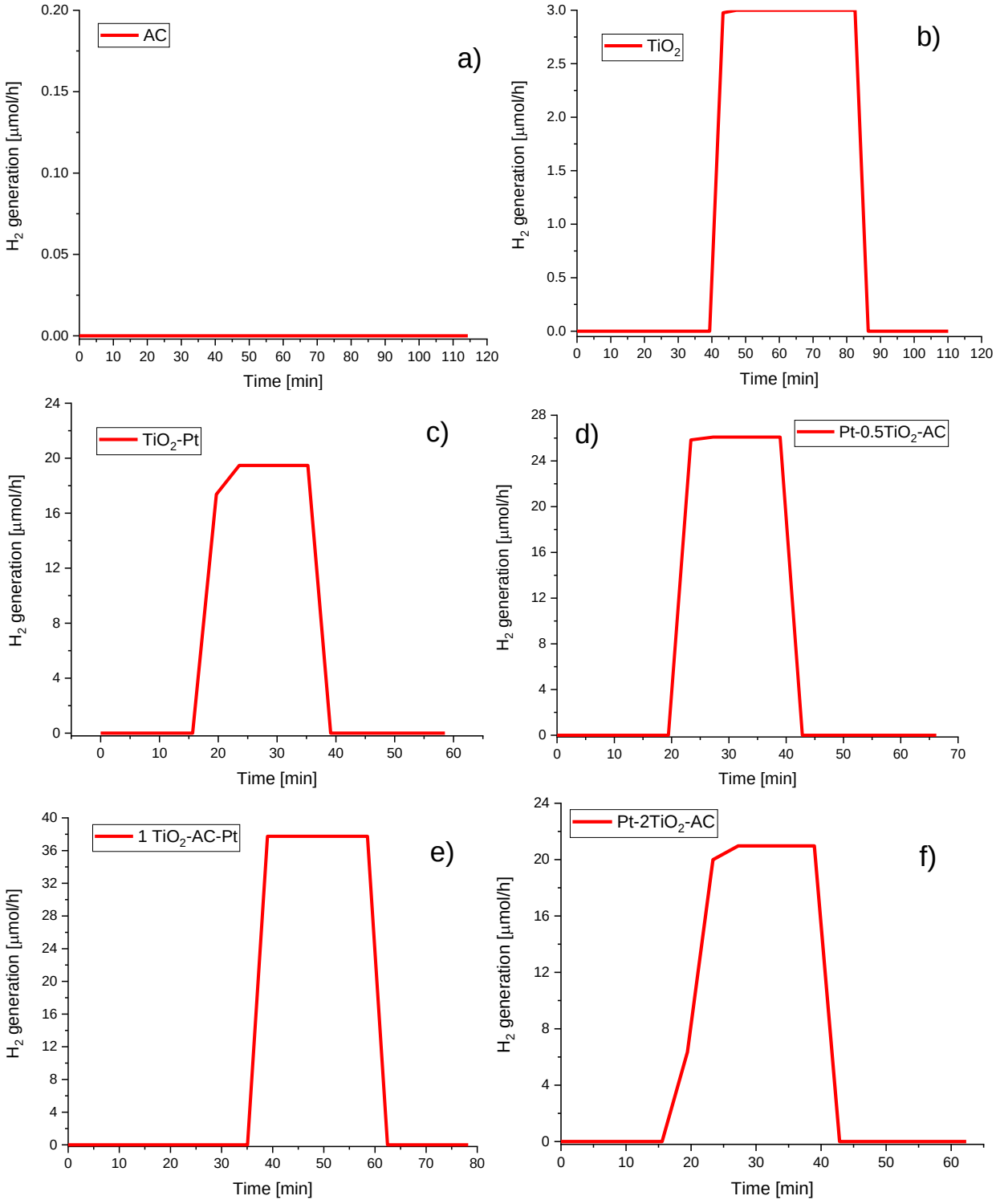
AC
a)
H2 generation [µmol/h]
Time [min]
TiO2
b)
H2 generation [µmol/h]
Time [min]
TiO2-Pt
c)
H2 generation [µmol/h]
Time [min]
Pt-0.5TiO2-AC
d)
H2 generation [µmol/h]
Time [min]
1 TiO2-AC-Pt
e)
H2 generation [µmol/h]
Time [min]
Pt-2TiO2-AC
f)
H2 generation [µmol/h]
Time [min]

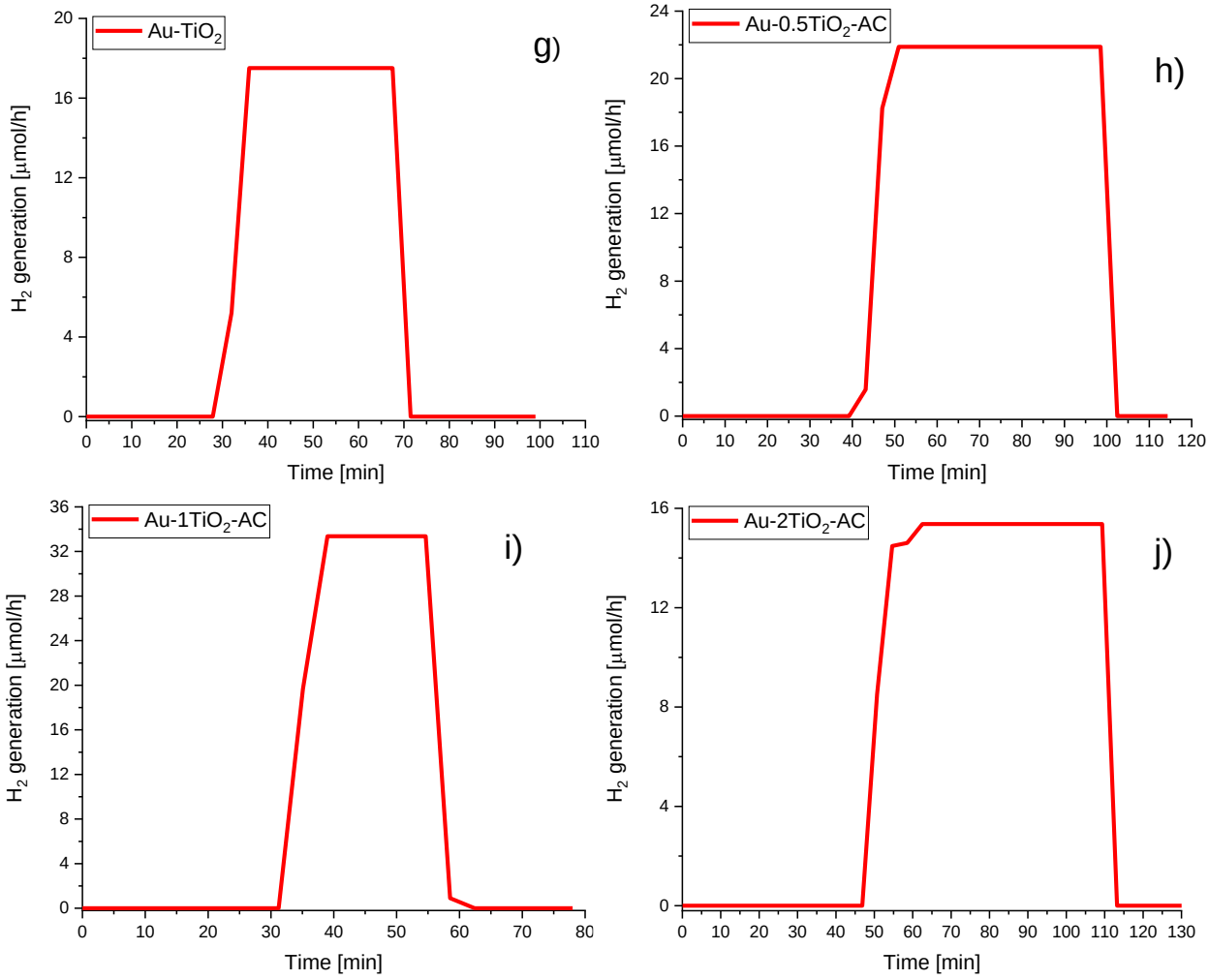

S1. Hydrogen generation for all of the samples in ethanol/water phase.

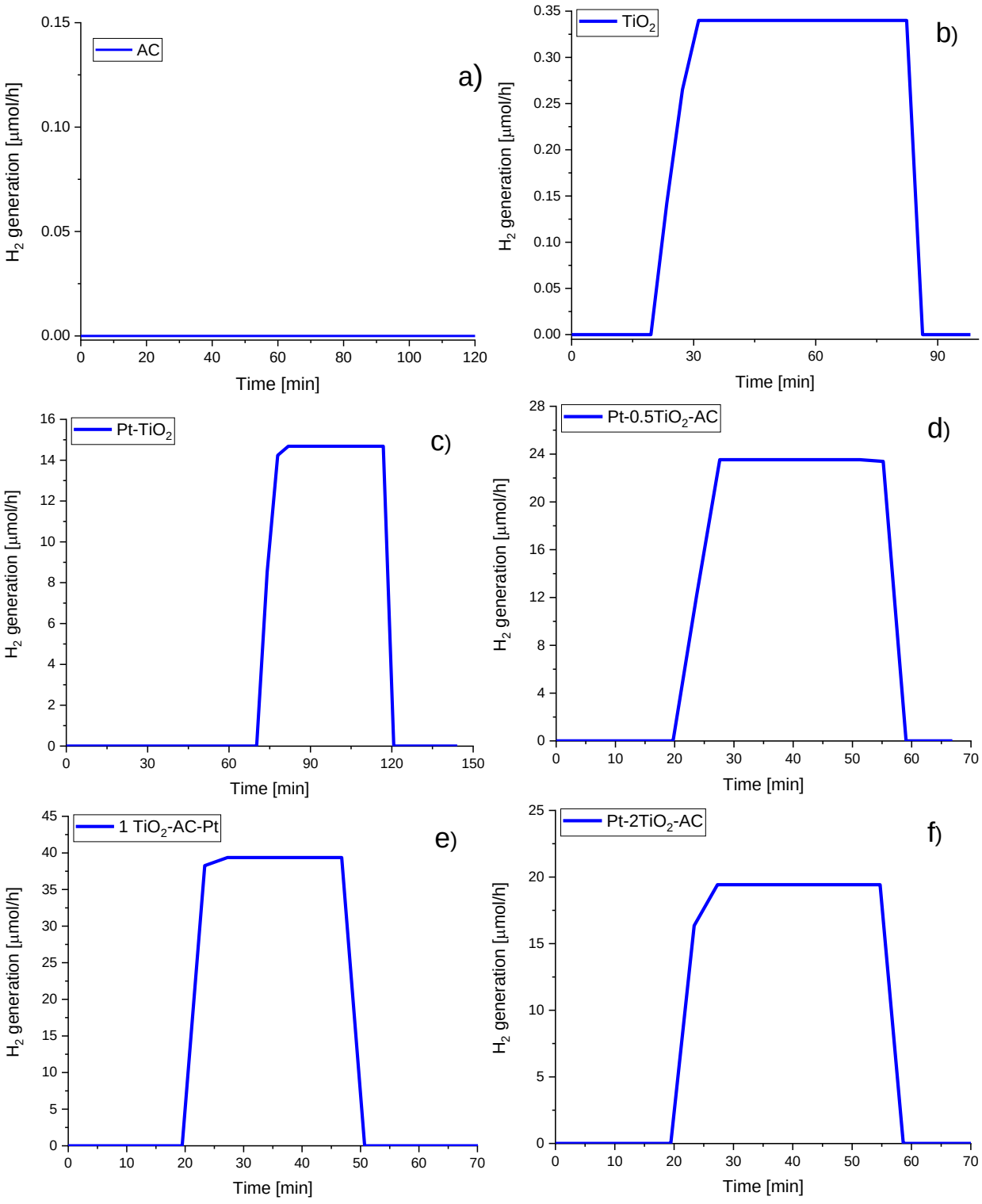
AC
a)
H2 generation [µmol/h]
Time [min]
TiO2
b)
Pt-TiO2
c)
Pt-0.5TiO2-AC
d)
1 TiO2-AC-Pt
e)
Pt-2TiO2-AC
f)

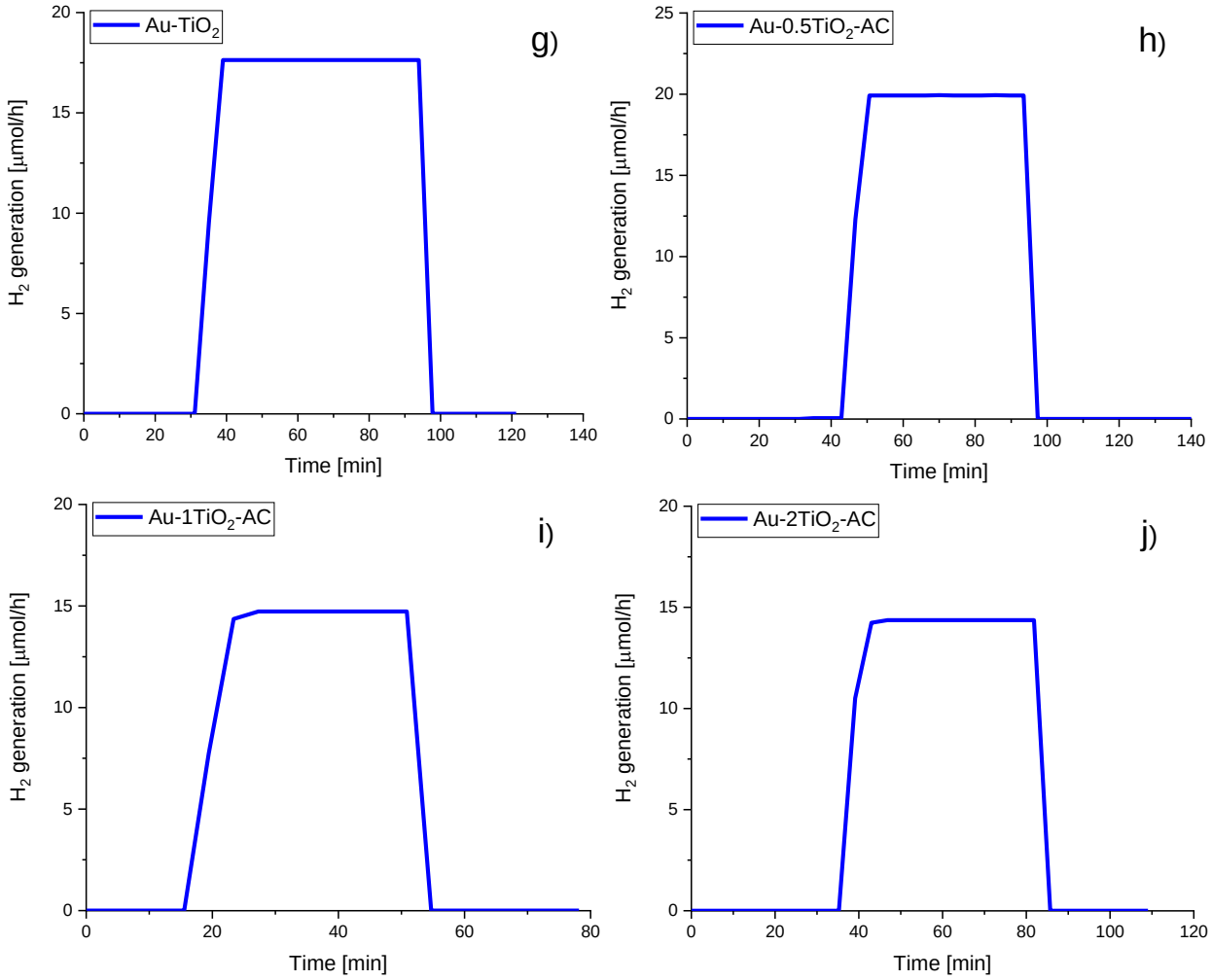

S2. Hydrogen generation for all of the samples in methanol/water phase.

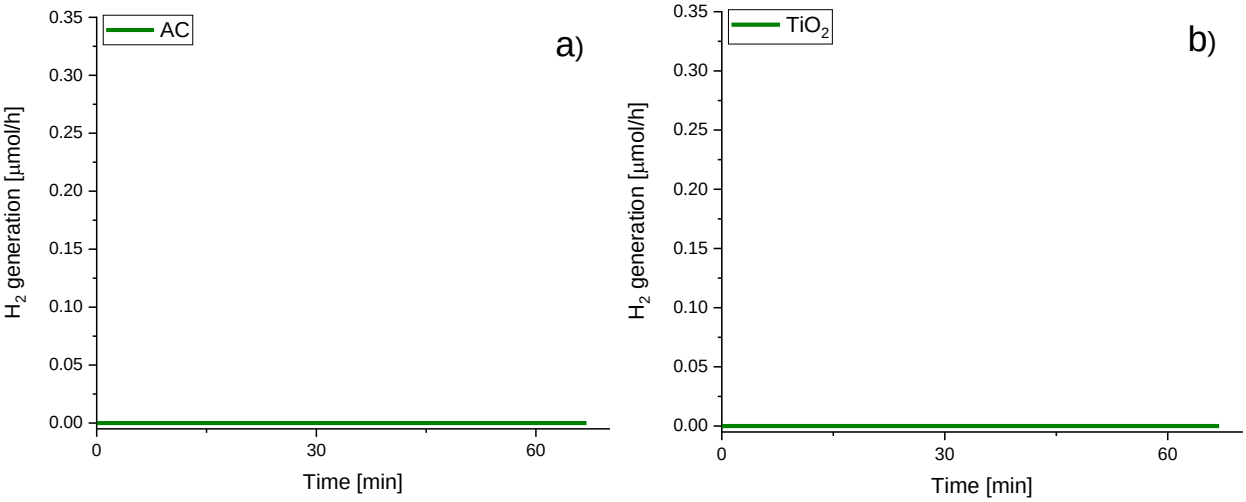

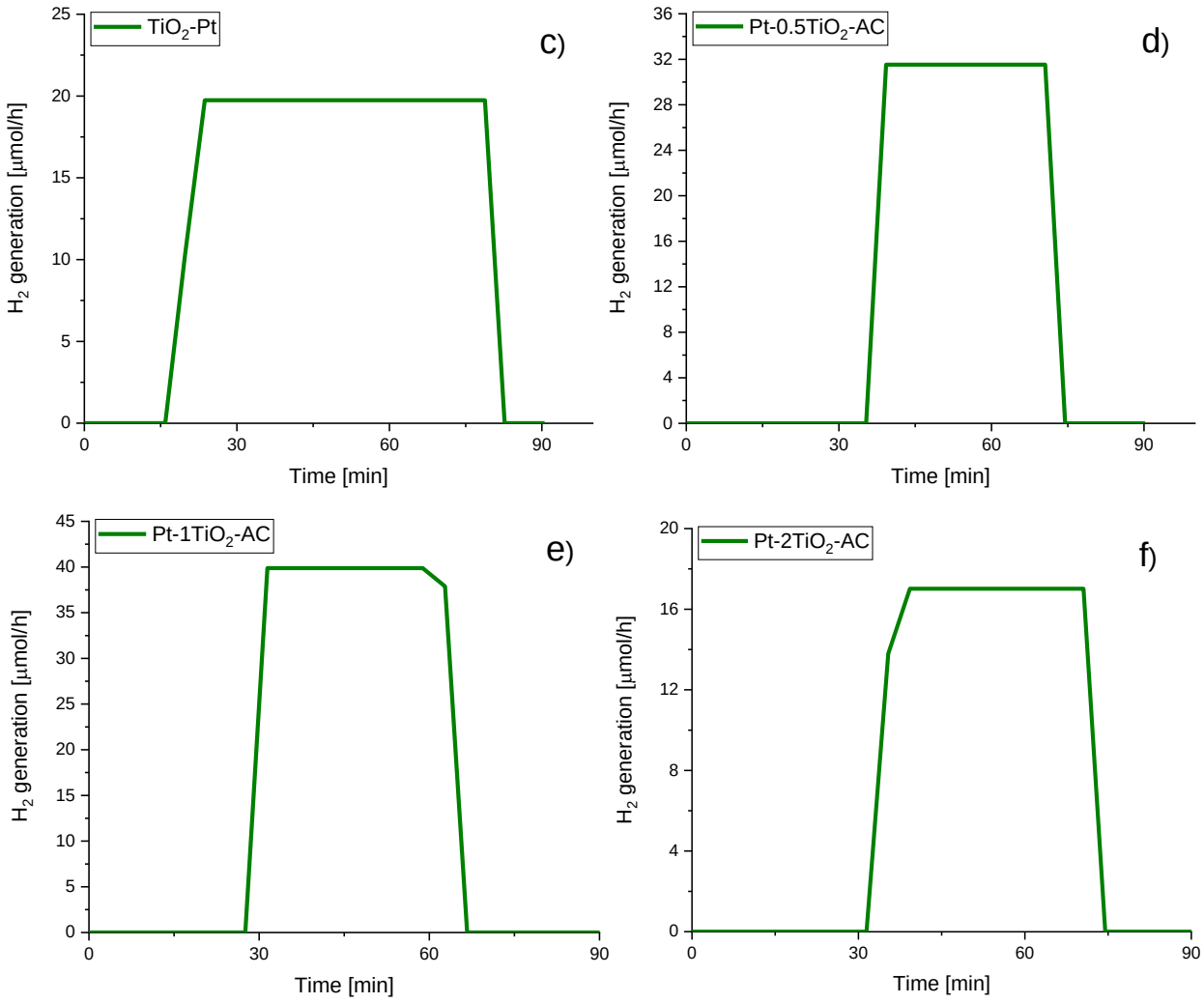
TiO2-Pt
c)
H2 generation [µmol/h]
Time [min]
Pt-0.5TiO2-AC
d)
H2 generation [µmol/h]
Time [min]
Pt-1TiO2-AC
e)
H2 generation [µmol/h]
Time [min]
Pt-2TiO2-AC
f)
H2 generation [µmol/h]
Time [min]

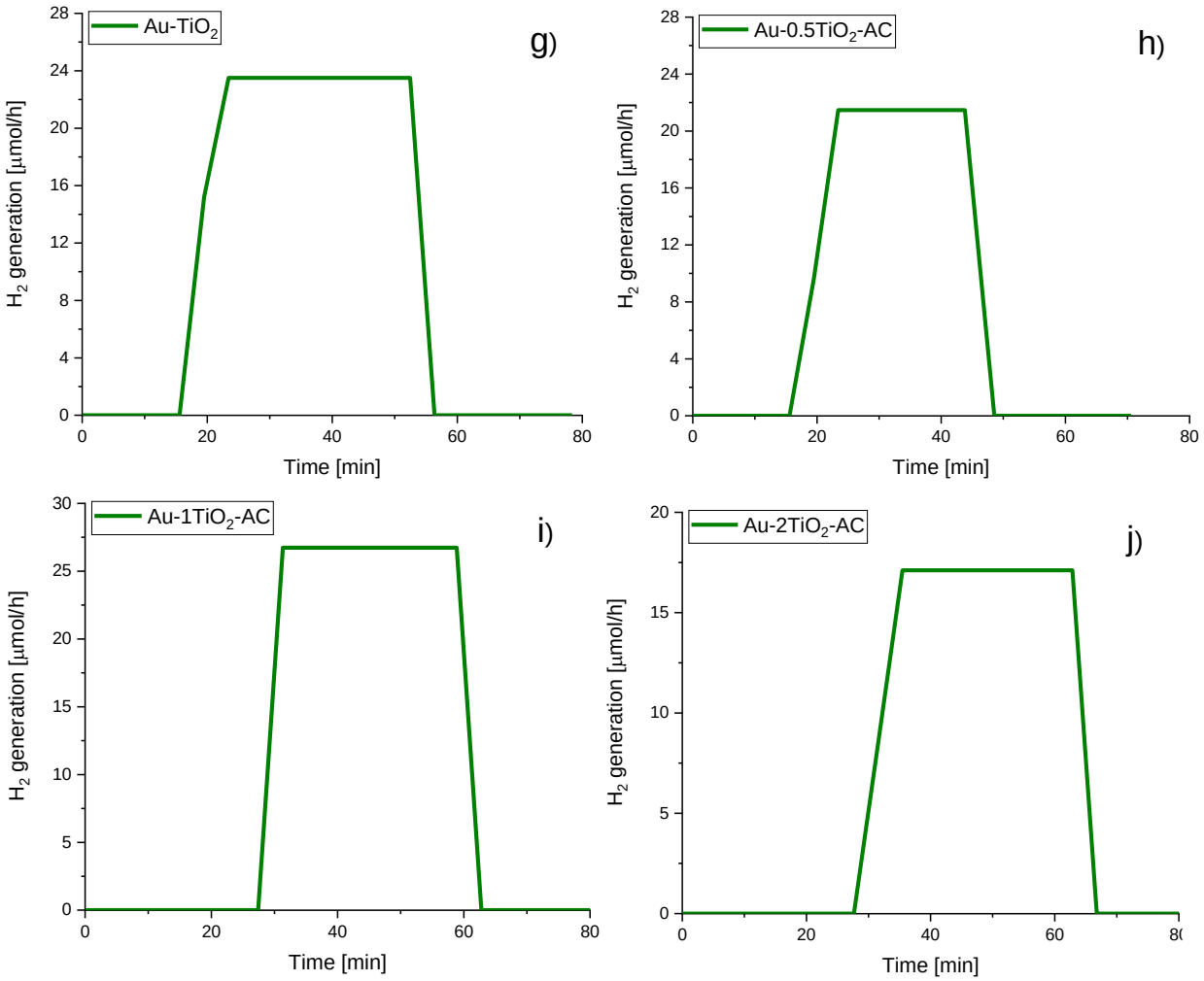

S3. Hydrogen generation for all of the samples in bioethanol/water phase.

Annex

Contents

1. Thermochemical production of hydrogen

Currently, one idea of reducing CO_2 in the atmosphere is its conversion into products with a high positive value, i.e., chemicals or fuels [1,2]. There is a possibility of thermochemical conversion of CO_2 using solar energy [3]. Research on thermochemical cycles dates back to the 1960s. They focused primarily on the development of materials for nuclear reactors. The increase in their importance in the production of synthetic fuels as one of the technological possibilities of using them via the low-emission route has increased with the approved worldwide protocols (Kyoto, Rio de Janeiro, etc.) [4]. One of the most effective thermochemical cycles is the two-step redox oxide pair system, which have shown great potential for synthetic solar fuel generation [5]. The principle of its operation is based on the transition between higher valence oxidized and lower valence reduced form of the oxide of a metal having multiple oxidation states [6]. In the first stage, there is a thermal reduction of the metal oxide through the release of oxygen as a result of an endothermic reaction. As a result, the oxidation state changes from higher to lower. The metal oxide is oxidized in the second stage by taking oxygen from water and/or CO_2. As a result, there is a return to the original oxidation state. This causes the production of H_2 and CO in reactions called water splitting (WS) and carbon dioxide splitting (CDS), respectively [7]. Cerium oxide is considered an excellent candidate for use in thermochemical cycles due to its well-known essential properties [8] as well as the ability to form superficial oxygen vacancies during reduction and easy oxidation [9]. This ability is described by equations 1 and 2:

$$CeO_{2-Xox} \rightarrow CeO_{2-Xox}\frac{\Delta X}{2}O_2 \qquad \text{Equation (1)}$$

$$CeO_{2-Xred} + \Delta X\ H_2O \rightarrow CeO_{2-Xox} + \Delta X\ H_2 \qquad \text{Equation (2a)}$$

$$CeO_{2-Xred} + \Delta X\ CO_2 \rightarrow CeO_{2-Xox} + \Delta X\ CO \qquad \text{Equation (2b)}$$

Equation 1 describes the endothermic reduction step, which is intended to perform using solar energy Equation 2 describes the exothermic oxidation where $CeO_{2\text{-}Xred}$ is re-oxidized by H_2O to generate H_2 (Equation 1) or by CO_2 to generate CO (Equation 2b).

As for metal, nickel proved to be a good choice due to its low price, relative stability and good properties in reactions involving CO_2 [10,11]. In the present work, cerium oxide rods have been used to support different concentration of nickel nanoparticles, a possible combination that is expected to perform well in carbon dioxide splitting.

1.1. Cerium oxide shapes

The rapidly developing field of nanomaterials is becoming very important in heterogeneous catalysis. This is because the properties of some nanocatalysts are shape-dependent. In addition, the simplicity of producing catalytic nanomaterials makes it easier for scientists to design materials with specific catalytic properties. The results presented in this chapter will focus on one of the objectives of this dissertation, namely, the synthesis of different nanoshaped CeO_2 by the hydrothermal method.

Cerium oxide has the ability to store and release oxygen easily, which makes it very interesting for redox processes [12]. It is obvious that there is a relationship between the oxygen storage capacity and the surface of the cerium oxide crystal exposed. The result of this dependence has a strong influence on the redox properties of cerium dioxide, which is directly related to the ability of cerium to change the oxidation state between Ce^{4+} and Ce^{3+} and the concomitant formation of oxygen vacancies. There are ideally three characteristic main planes for cerium dioxide: cubes (100), rods (110) and octahedral (111). Figure 1 shows a scheme of the different planes of ceria. The fact is that the stability of these planes is of the order octahedral (111) > rods (110) > cubes (100). The shape of the octahedral is the most stable of all [13].

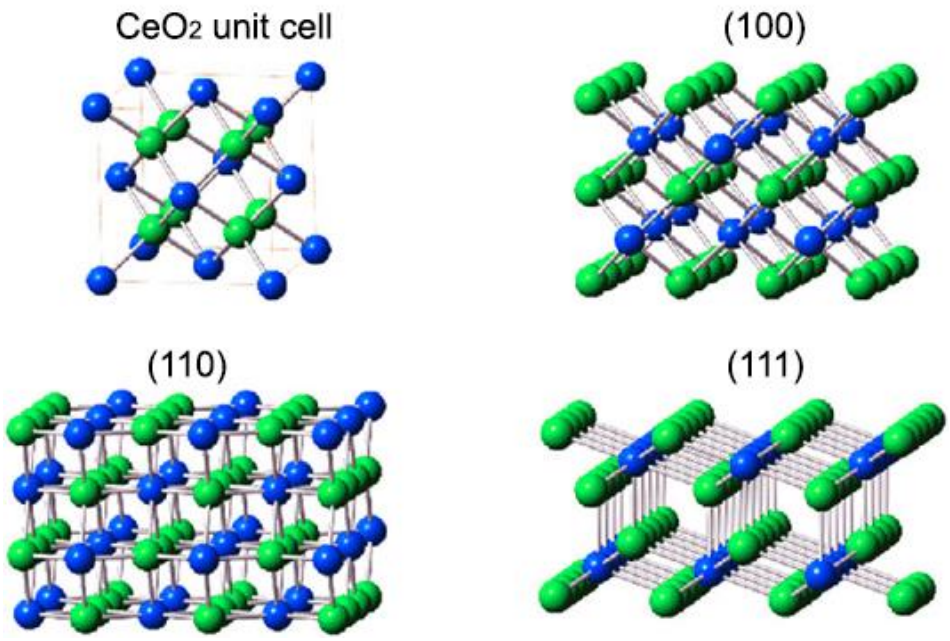

Figure 1. Cristal models of cerium dioxide shapes [14].

1.1.1. Catalyst synthesis

To prepare polycrystalline cerium dioxide (no preferred crystal planes exposed), a solution of 2.0 g of NaOH dissolved in 245 mL of distilled water was prepared using a magnetic stirrer at 300 rpm. A beaker was prepared separately in which 6.07 g of $Ce(NO_3)_3 \cdot 6H_2O$ were dissolved in 35 mL of distilled water with a magnetic stirrer. Using an ultrasonic atomizer, the cerium salt was added to the aqueous solution of NaOH. The final molarity of the solution was 0.2 M. The resulting solution was then aged for 30 minutes and introduced in a hydrothermal reactor at 150 °C for 24 hours to produce polycrystalline cerium oxide. After cooling, the next step was centrifuging the solution, treating it with ultrasound, and purifying it with distilled water (three times) and ethanol (twice) until the excess NaOH was completely eliminated from the material. Each centrifugation step was performed at 25 °C, 6000 rpm and 20 minutes to achieve complete separation. The material then was dried at a temperature of approx. 60 °C and

crushed in an agate mortar to obtain a fine powder. The last step was calcination at 450 °C for 4 hours with a 2 °C/min ramp rate.

The cerium dioxide rods and cubes were prepared using the same method, but using different concentrations of NaOH in the precursor solution and temperature of the hydrothermal method. The method of preparing the rods assumes an OH^- concentration of 7.875 M. A solution of 6.08 g $Ce(NO_3)_3 \cdot 6H_2O$ in 35 mL of distilled water was sprayed into a solution of 88.133 g of NaOH in 245 mL of distilled water. Crystallization of the precursor solution in the hydrothermal reactor was carried out at 100 °C for 24 hours in order to produce rods. The cubes were prepared with an OH^- concentration of the precursor solution of 6 M. A solution of 6.08 g $Ce(NO_3)_3 \cdot 6H_2O$ in 35 mL distilled water was sprayed into a solution of 67.23 g NaOH in 245 mL distilled water. The precursor solution was treated in a hydrothermal reactor at 180 °C for 24 hours.

To obtain of cerium dioxide in octahedral shape, 3.26 g of Ce $(NO_3)_3 \cdot 6H_2O$ were dissolved in 50 mL distilled water using a magnetic stirrer. Then, this solution was spread using an atomizer to the solution of 4.95 mg $NaPO_4 \cdot H_2O$ with 250 mL distilled water and mixed with a magnetic stirrer for one hour. The next step was to put the solution in the autoclave and heated it at 180 °C for 10h. After cooling, treatment was the same as for the other shapes.

1.1.2. Characterization

1.1.2.1. Textural parameters

A QUADRASORB evo TM gas sorption surface area and pore size analyzer was used for textural characterization. Nitrogen adsorption isotherms were measured at -196 °C and carbon dioxide isotherms at 0 °C. Before adsorption measurements all samples were outgassed at 250 °C for at least 20 h. The specific surface area was calculated using the Brunauer–Emmett–Teller (S_{BET}) equation from nitrogen adsorption isotherms. The total pore volume (Vtot) was evaluated from the nitrogen volume adsorbed at a relative

pressure of ~0.98 atm. The volumes of larger micropores (super-micropores) and small micropores (ultramicropores) were calculated by the DFT method on the basis on nitrogen adsorption. The pore size distribution was obtained from the DFT model in the Quadra Win software package based on the N_2 sorption isotherm. In this case, a cylinder pores ASDFT adsorption model was used. To calculate pore size distribution from CO_2 sorption isotherm a NLDFT model of the same software was applied.

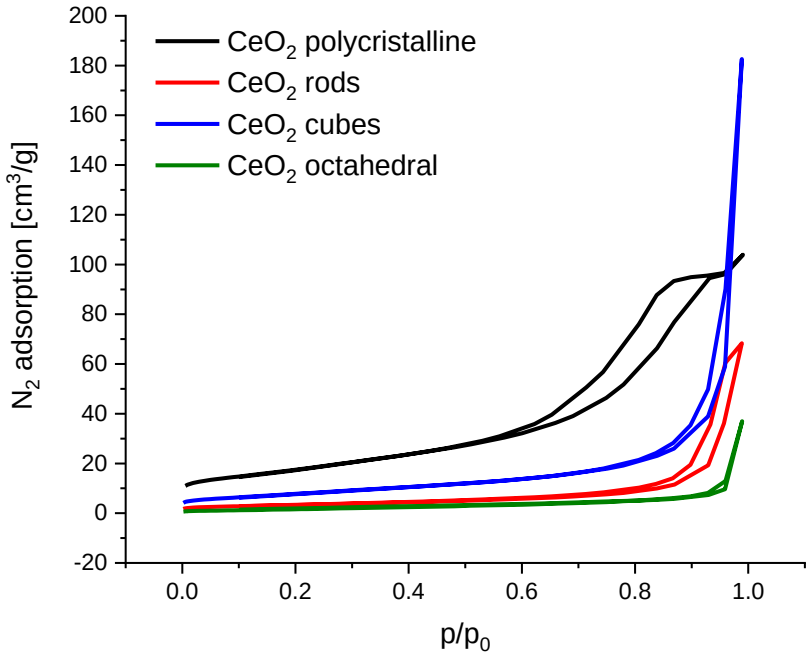

Figure 2. Adsorption - desorption isotherms of nitrogen for cerium dioxide shapes.

Figure 2 shows the N_2 adsorption isotherms of the cerium dioxide shapes prepared. The polycrystalline ceria presented a IV type isotherm, characteristic of mesoporous materials and a H3 hysteresis loop associated to materials with a regular porous structure and a narrow pore size distribution. The others types of shapes also showed type IV isotherm and a H4 hysteresis loop. The type H3 loop is observed with aggregates of plate-like particles giving rise to slit-shaped pores. On the other side, a type H4 loop can be correlated to narrow slit-like pores. Solsona et al. [15] reported similar results. The respective pore size distribution (PSD) of the samples are presented in figure 3 and indicate that samples are mesoporous with pore diameter higher than 4 nm.

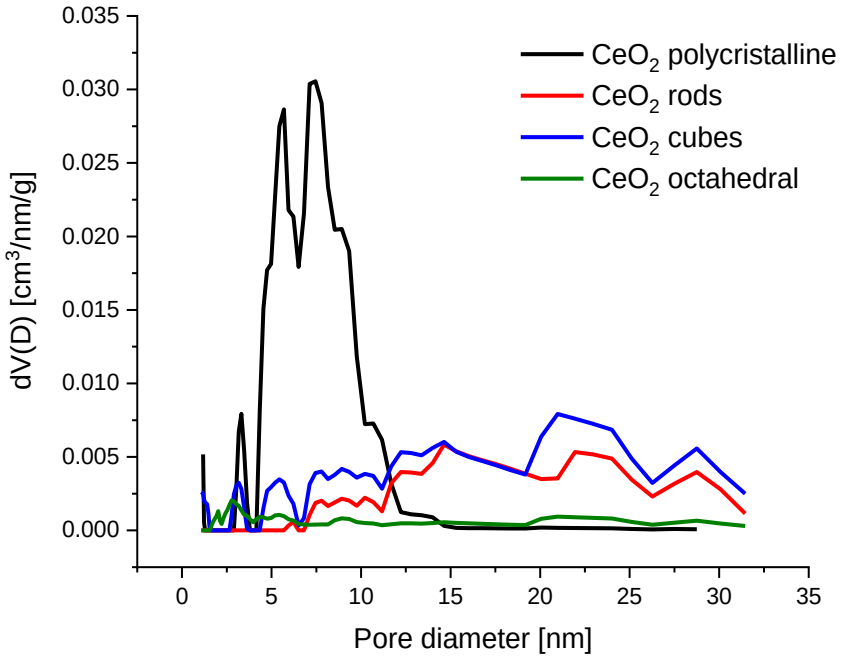

Figure 3. Pore size distribution for cerium dioxide shapes.

Table 1. Textural properties of cerium oxide shapes.

Cerium oxide	BET [m^2/g]	DFT pore volume [cm^3/g]	TPV [cm^3/g]	DFT CO_2 [cm^3/g]
Polycrystalline	63.7	0.145	0.1611	0.013
Rods	18.8	0.086	0.1060	0.002
Cubes	28.9	0.129	0.2832	0.006
Octahedral	6.6	0.019	0.0573	0.001

Table 1 summarizes the textural properties for all cerium oxide samples. Surface area values are in the range of 6.6- 63.7 m^2/g and total pore volume values of 0.06–0.28 cm^3/g. The micropore volume of narrow pores (0.3–1.4 nm) ranged from 0.001 to 0.013 cm^3/g and micropore volume values estimated based on N_2 adsorption ranged from 0.02 to 0.15 cm^3/g.

1.1.2.2. UV-VIS

UV-vis absorbance spectroscopy was measured on a Shimadzu UV 3600 UV-Vis/NIR equipment. $BaSO_4$ was used as a reference standard. The spectra were registered at 25 ^oC in air within the range of 200-800 nm. The band gap energies (E_g) of the samples were calculated from UV-Vis spectra absorption by the Tauc plot equation [16,17].

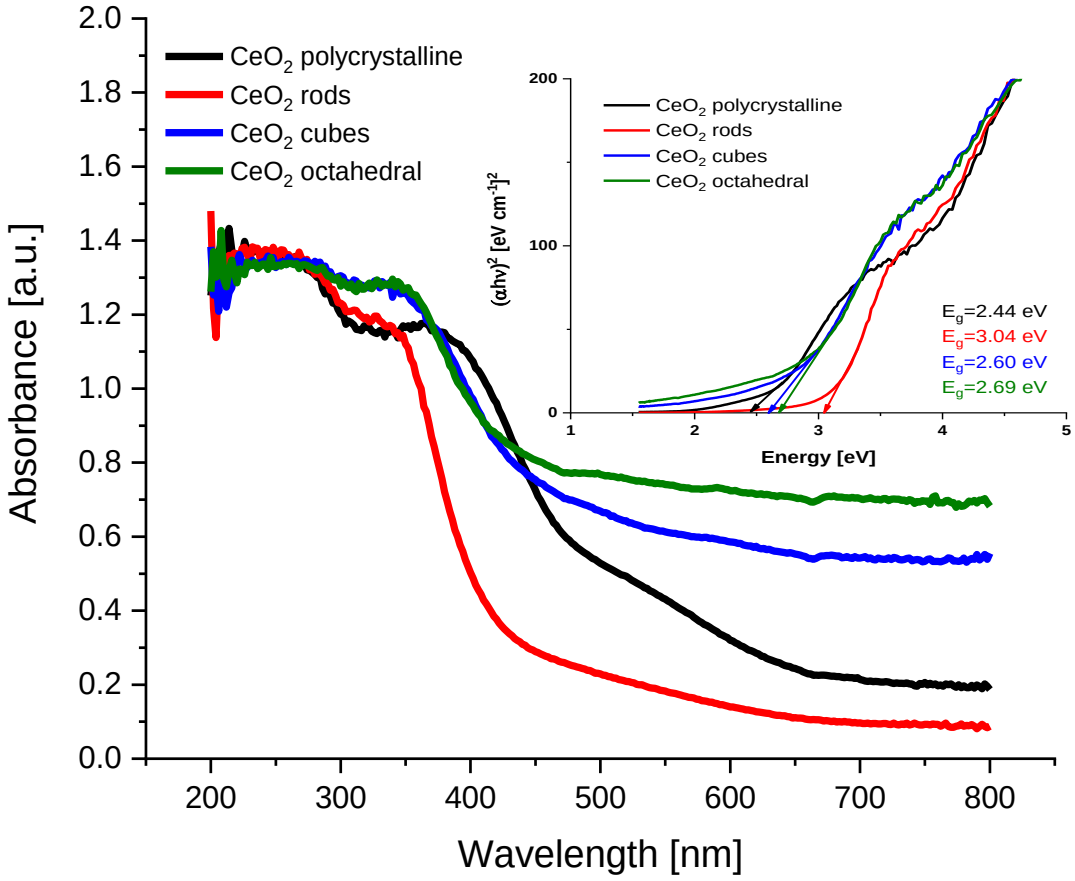

Figure 4. UV-Vis absorption spectra of the prepared cerium dioxide shapes and optical band gap determination from Tauc plots.

UV-visible absorption spectra of CeO_2 shapes are shown figure 4. All samples have a strong absorption below 400-450 nm. The broad absorption bands located at 250 and 340 nm originate from the charge transfer transition from O^{2-}(2p) to Ce^{4+}(4f) orbitals in CeO_2 [18]. These spectral profiles indicate that the charge transfer transition of Ce^{4+}

overlaps with the $4f^1$-$5d^1$ transition of Ce^{3+}. It can be seen that the intensity and position of the absorption bands are characteristic for the different shapes of CeO_2.

The band gap values obtained are 2.44, 3.04, 2.60, 2.69 eV, respectively, for samples CeO_2 polycrystalline, CeO_2 rods, CeO_2 cubes and CeO_2 octahedral (table 2). The spacing of the electronic levels and the energy band gap are highly dependent of the particle shape. Similar conclusions have been reported by Patsalas et al. [19] and Filtschew et al. [20].

1.1.2.3. Raman spectroscopy

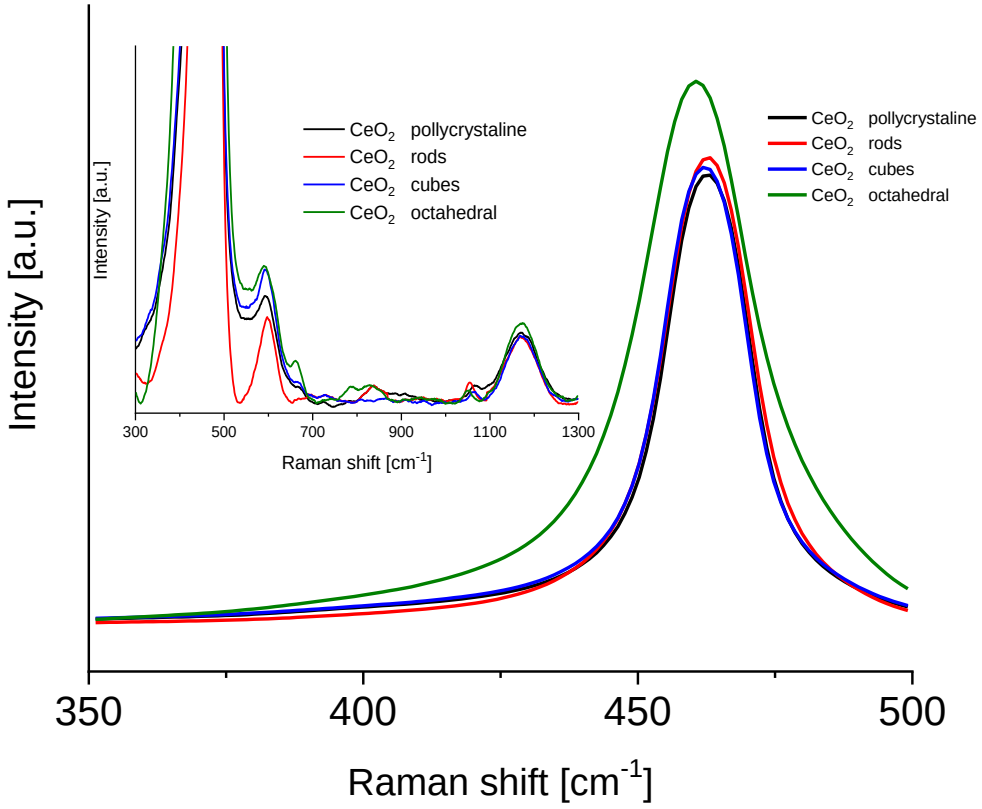

Figure 5. Raman spectra of the cerium dioxide shapes.

Figure 5 shows the Raman spectra of the synthesized different shapes of cerium oxide. These spectra show an intense peak centered at approximately 465 cm^{-1}. This peak can be associated with the F_{2g} Raman vibrational mode of the crystalline fluorite type of

structure of ceria, originated by the tension vibrations of the oxygen atoms that surround the cerium [21, 22, 23]. All ceria dioxide shapes spectra shown characteristic peaks of bulk ceria at 370, 465, 550, 595, 660 and 1170 cm^{-1} [24]. According to Filtschew et al. [20] the peaks on the range 370- 660 cm^{-1} can be ascribed to second-order Raman peaks. In fact, the former results from a combination of A_{1g}, E_g, and F_{2g} scattering tensors, whereas the latter arises from mixing A_{1g} and E_g scattering tensors [24]. The peak around 600 cm^{-1} correspond to O^{2-} vacancies and replacement of cerium(IV) atoms by cerium(III) atoms [25, 26]. Other small band around 800 cm^{-1} can be attributed to adsorbed peroxide species (O_2^{2-}). The band located around 1170 cm^{-1} was observed in all the spectra of ceria oxide and can be correlated with the Raman mode characteristic of surface superoxide species (O_2^{2-}). A small carbonate peak was observed at about 1060 cm^{-1}. The particle size of the CeO_2 samples was calculated from the Raman line broadening using the equation (3):

$$\Gamma\ (cm^{-1}) = 10 + \frac{124.7}{\mathrm{D}} \qquad \text{Equation (3)}$$

Where:

Γ (cm^{-1}) is the full width at half maximum of the Raman active mode peak at 465 cm^{-1} and D is the particle size of the CeO_2. The size of the ceria nanoparticles samples CeO_2 polycrystalline, CeO_2 rods, CeO_2 cubes and CeO_2 octahedral are presented in Table 2.

1.1.2.4. X-ray diffraction (XRD)

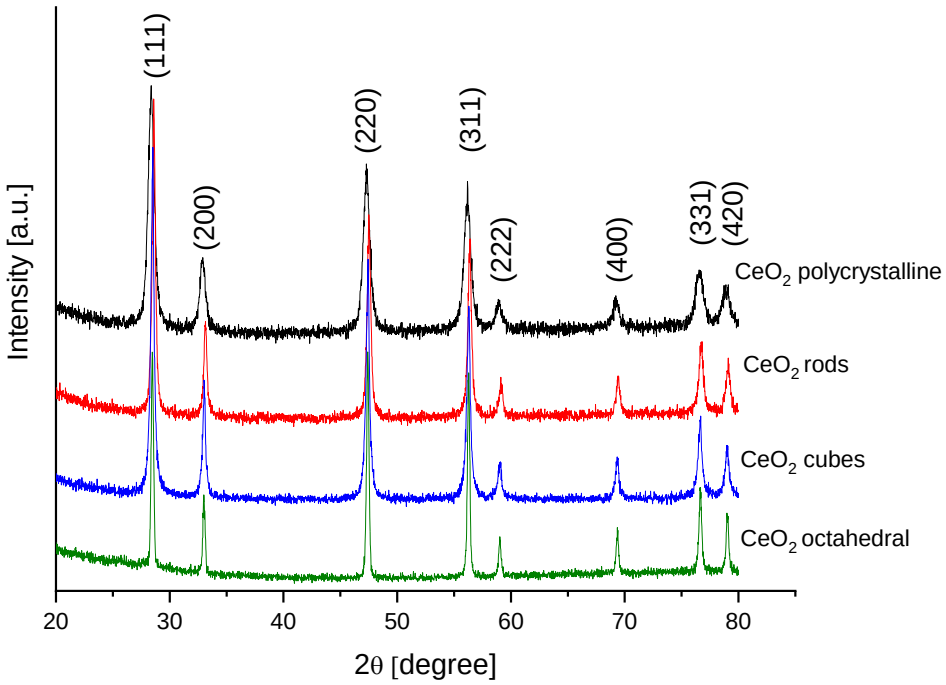

Figure 6. XRD profiles of different cerium dioxide shapes.

Figure 6 shows the XRD patterns of different shapes of cerium dioxide. These XRD patterns were indexed with the JCPDS card no. 81-0792. Eight diffraction peaks were observed at 2θ values, 28.42, 33.13, 47.37, 56.23, 59.04, 69.33, 76.60, and 79.02 corresponding to reflections from the (111), (200), (220), (311), (222), (400), (331), and (420) planes of the cubic crystalline phase of CeO_2.

A good crystallization of all shapes of the cerium dioxide was confirmed with sharp and strong peaks. No additional peaks were observed, indicating a high purity of the synthesized samples. The crystallite sizes (D) have been estimated by applying the Scherrer formula (equation method chapter 2). Table 2 presents the average crystallite size for different shapes of cerium dioxide.

Table 2. Calculated values of particle size and band gap of cerium dioxide shapes.

Sample	Crystallite size calculated using XRD (nm)	Particle size calculated using Raman (nm)	Band gap (eV)
CeO_2 polycrystalline	12.7	13.1	2.44
CeO_2 rods	28.2	27.5	3.04
CeO_2 cubes	14.3	16.1	2.60
CeO_2 octahedral	21.1	20.5	2.69

1.1.2.5. SEM

Figure 7 shows representative SEM images of the different morphologies of cerium dioxide prepared: polycrystalline (a), rods (b), cubes (c), and octahedral (d). On measuring the nanoparticles using the image J software, the average size of the particles obtained for each shape was in the range of: 12-13 nm for polycrystalline; 16 nm to 17 nm for rods, 15-16 nm cubes and 20-21 nm octahedral.

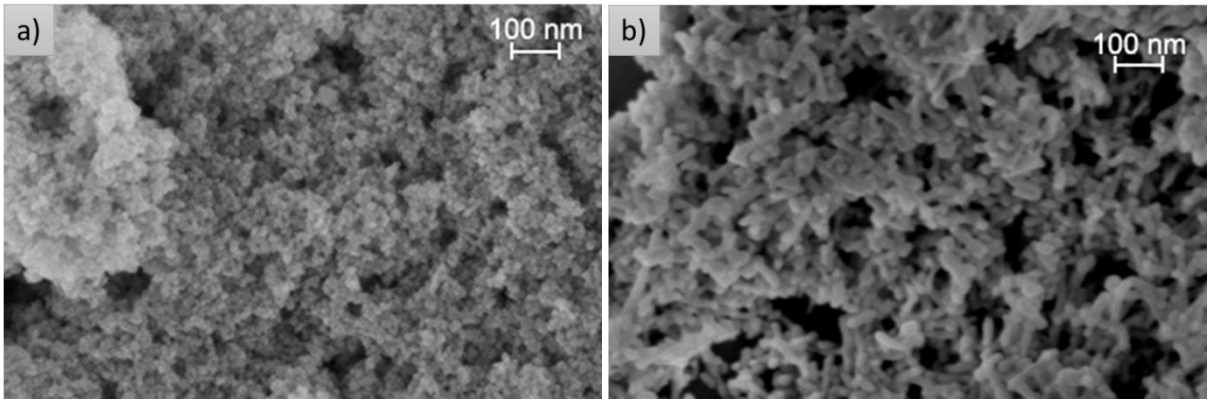

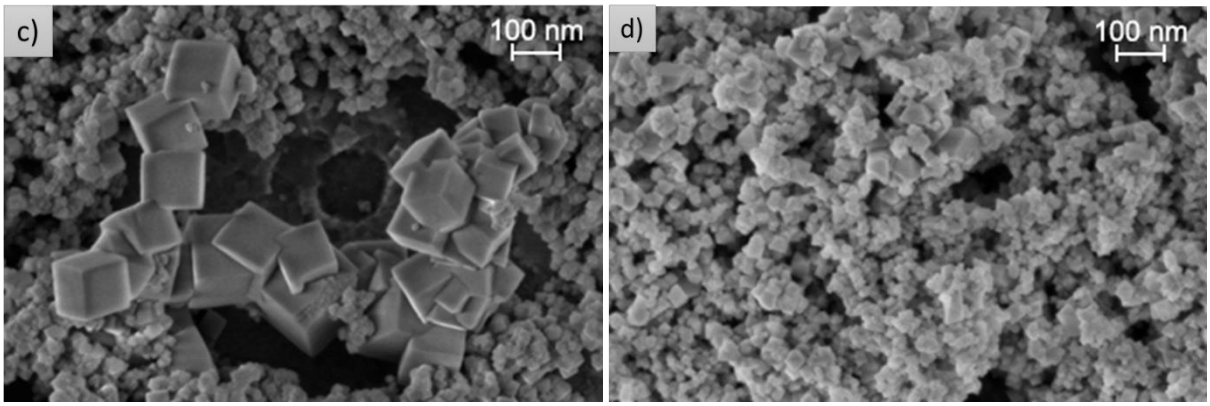

Figure 7. SEM analysis of cerium dioxide shapes: a) polycrystalline, b) rods, c) cubes and d) octahedral.

1.1.2.6. H_2-TPR

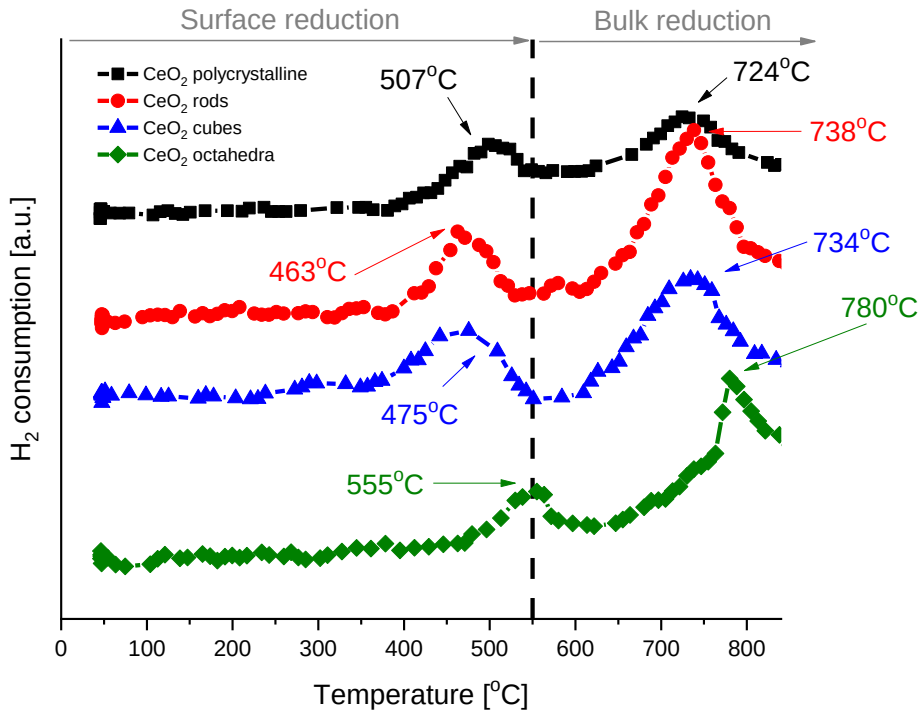

Figure 8. H_2-TPR curves of cerium dioxide shapes (~50 mg).

H_2-TPR analysis was performed to understand the reducibility of the various shapes of cerium dioxide (Fig. 8). The H_2-TPR profiles of all samples exhibit a bimodal shape with a wide low temperature peak at 463–555 °C, which is attributed to the characteristic

reduction of surface ceria and a wide high temperature peak at 724−780 °C, which corresponds to the bulk ceria reduction [27, 28]. The hydrogen consumption was calculated for each cerium dioxide shape and is presented in table 3. After H_2-TPR analysis, the samples were subjected to pulse CO_2 oxidation to study the oxygen transfer from CO_2 to reduced ceria through the replenishment of oxygen vacancies created during the reduction treatment with H_2. Pulse CO_2 sorption was applied until the cerium oxide was fully saturated with oxygen. The results for the individual shapes of cerium dioxide are included in Table 3. In all cases an excellent oxygen transfer was measured, with H_2 consumption and CO_2 consumption values virtually identical. The highest reduction/oxidation value was achieved for CeO_2-rods, and it was about 170 µmol/g_{cat}. The lowest value was achieved for CeO_2-octahedral, with only 20 µmol/g_{cat}.

Table 3. The overall amount of hydrogen consumed in H_2-TPR and oxygen consumed in CO_2 pulse chemisorption.

Catalyst	**H_2 consumption [µmol/g_{cat}]**	**CO_2 consumption [µmol/g_{cat}]**
CeO_2 polycrystalline	107.1	106.8
CeO_2 rods	170.1	169.1
CeO_2 cubes	124.9	124.4
CeO_2 octahedral	20.3	20.1

Conclusions

Four distinct shapes of cerium dioxide (polycrystalline, rods, cubes, and octahedral) were successfully prepared and characterized by N_2 and CO_2 adsorption/desorption, UV-VIS, FTIR spectroscopy, SEM, Raman spectroscopy, XRD spectroscopy, H_2-TPR and pulse CO_2 sorption. It is concluded that ceria rods exhibit the best oxygen storage and exchange capacity.

1.2. Nanoshaped cerium oxide doped with metals (Ru, Pd, Au, Pt, and Ni) prepared by incipient wetness impregnation (IWI) and ball milling (BM) method

An important role in the catalytic process is the strong metal-carrier interaction (SMSI). Therefore, after the characterization of different cerium dioxide shapes, the influence of Ru, Pd, Au, Pt and Ni on the ceria properties was investigated. After analyzing the reduction/oxidation ability of various cerium oxide shapes (described in sub-section 4.1), CeO_2-cubes and CeO_2-rods were selected for further studies due to the highest values of oxygen storage-release. Then, they were decorated with 2% wt. of the metal (Ru using $RuCl_2$, Pd using $PdCl_2$, Au using $Au(O_2CCH_3)_3$, Pt using $PtCl_2$, and Ni using $NiCl_2$). The catalysts were prepared in two different ways, the first of which was the traditionally and commonly used method of incipient wetness impregnation (IWI), which consisted of weighing the appropriate amount of the metal precursor and dissolving it in ethanol, sonicating, and then using an automatic pipette to apply the solution on cerium oxide by spotting. The second method used was ball milling, where a powder mixture placed in the ball mill is subjected to high-energy collision from the balls (BM). For the ball milled samples, the metal precursor was mixed directly with cerium dioxide in a zirconium oxide vessel (0.5 g of sample and 1 zirconium oxide ball of 15 mm diameter) using a Fritsch Pulverisette 23 (Idar-Oberstein, Germany) mini-mill apparatus. The ball milling conditions were 15 Hz for 3 min. These conditions were selected to avoid any modification of the cerium dioxide shapes. After both methods, samples were calcined at 450°C for 4 h (5°C/min). Subsequently, the redox properties of the obtained catalysts were checked by CO_2 pulse chemisorption. Figure 9 shows all of the results.

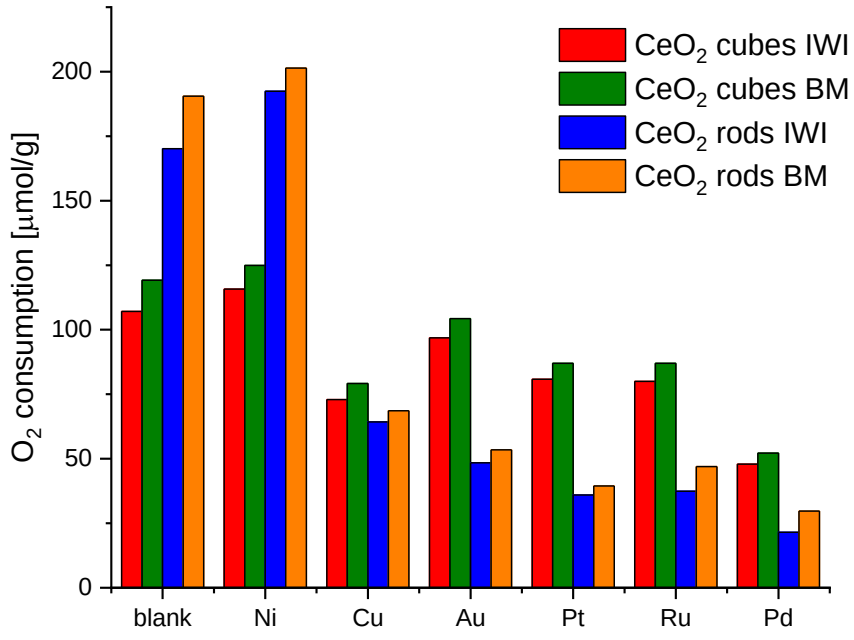

Figure 9. Redox ability of catalysts with different metal and method of activation for CeO_2 cubes and CeO_2 rods.

The obtained results showed that nickel turned out to be the most efficient metal for both CeO_2 cubes and CeO_2 rods. In addition, the ball milling method for the preparation of the catalysts increases its redox capacity. Therefore, nickel as metal and ball milling method to prepare the catalysts were chosen for further research.

An attempt to evaluate the effect of the nickel salt type on the redox properties of the catalysts was investigated. Catalysts based on various shapes of CeO_2 and various nickel precursors: nickel nitrate ($Ni(NO_3)_2$; nickel chloride ($NiCl_2$) and nickel acetate ($Ni(CH_3CO_2)\cdot 4H_2O$ were prepared (Figure 10).

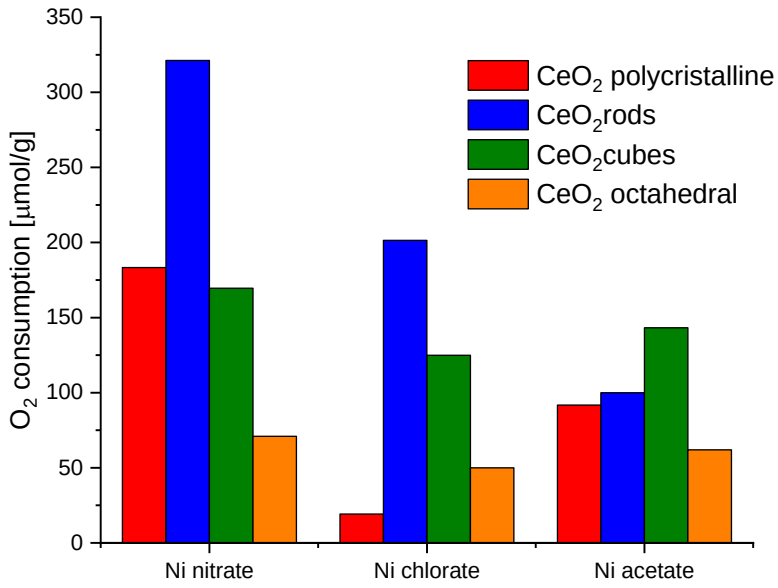

Figure 10. Redox ability of catalysts based on different shapes of CeO_2 and nickel salt.

Figure 10 shows the effect of the nickel salt used on the redox properties of catalysts based on different shapes of cerium oxide. The highest values were obtained for CeO_2 rods using nickel nitrate. Based on these observations, it was decided to investigate another parameter; the effect of the amount of metal on the redox capacity of the catalyst was investigated.

1.2.1. Preparation of Ni-CeO_2 catalysts

Catalysts were prepared by the milling method (15 Hz for 3 min) using CeO_2 rods and nickel nitrate at various metal weight concentrations of 0.5%, 1%, 2%, 5% and 10%, respectively. Finally, all prepared samples were calcined at 350°C with a ramp of 2°C/min in air during 4 h. The prepared Ni-CeO_2 catalysts were named as 0.5%Ni-CeO_2 rods, 1%Ni-CeO_2 rods, 2%Ni-CeO_2 rods, 5%Ni-CeO_2 rods and 10%Ni-CeO_2 rods according to the nominal wt. % concentration of Ni.

1.2.2. Results

Figure 11 shows the results of the structural and textural characterization of the Ni-CeO_2 rods samples performed by N_2 adsorption-desorption isotherms.

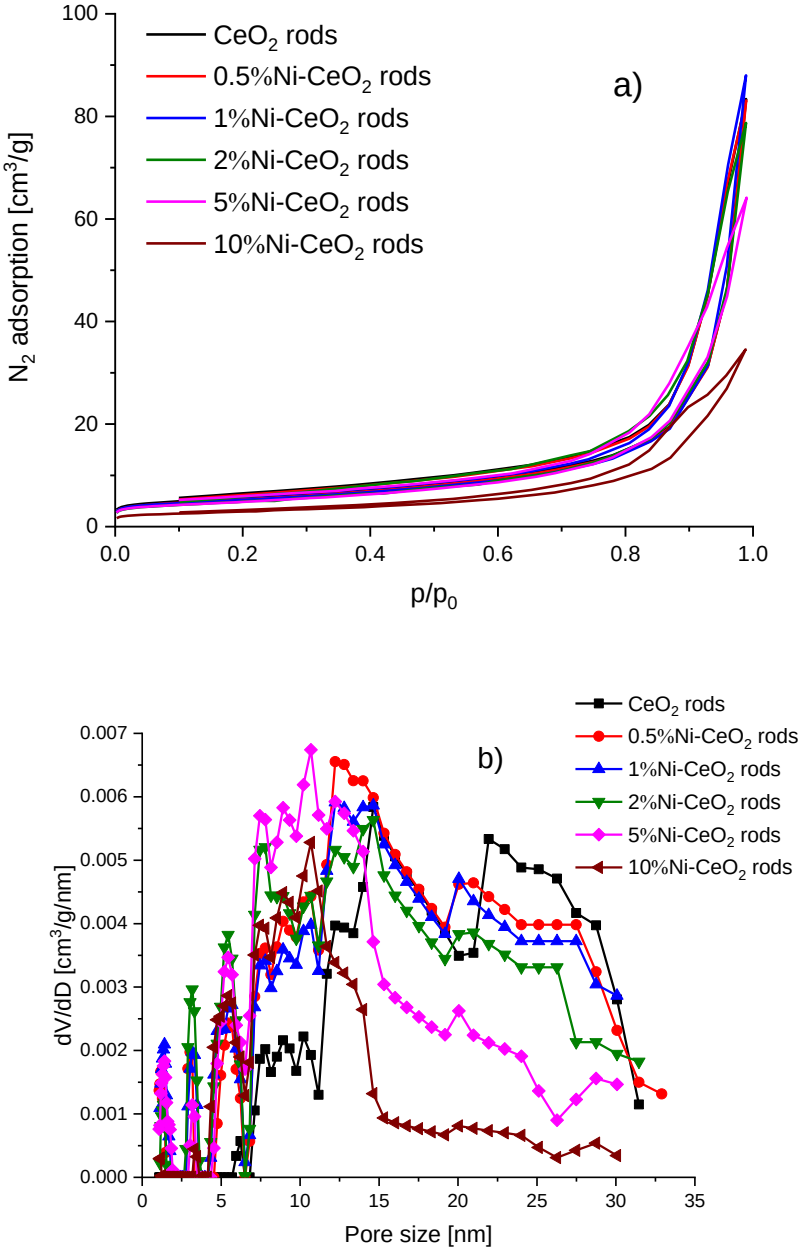

Figure 11. N_2 adsorption- desorption isotherms (a) and pore size distribution (b).

All isotherms of adsorption-desorption of N_2 presented in Figure 1a showed type IV isotherm with a H3 shaped hysteresis loop according to the IUPAC classification. This type is typical for powders containing mesopores [29]. Figure 1b presents the pore size distribution for all samples. Catalysts exhibited an average pore size of 5-32 nm. An increase of %Ni resulted to a narrowing of the range of pore distribution. The textural parameters of specific surface area (S_{BET}), total pore volume (V_{tot}), micropore volume (V_m) and pore diameter (D_p) for all catalysts are listed in Table 4. The specific surface area and pore volume decreased as the nickel loading increased with respect to pure cerium dioxide. It is likely that pore blocking was caused by nickel accumulation. Conversely, the diameter of the pores was not affected notably by the increasing of nickel. Similar conclusion was observed by Peymani et al. [30]. Damyanova et al. [31]prepared Ni/CeO_2-Al_2O_3 catalysts and reported the same trends for all textural parameters. According to XRF analysis, the Ni loadings reached values close to the nominal ones (Table 4).

Table 4. Textural characteristics of Ni-CeO_2 rods samples.

Sample	**S_{BET} (m^2/g)**	**V_{tot} (cm^3/g)**	**V_m(cm^3/g)**	**D_p (nm)**	**Length of CeO_2 crystals [nm]**	**Ni (wt.%) loading according to XRF**	**Ni dispersion (%)**
0.5%Ni-CeO_2 rods	18.7	0.14	0.018	12.4	25.9	0.44	4.2
1%Ni-CeO_2 rods	18.2	0.13	0.015	12.3	27.1	1.05	5.4
2%Ni-CeO_2 rods	17.1	0.12	0.015	12.3	28.5	2.09	9.7
5%Ni-CeO_2 rods	15	0.10	0.010	12.1	31.9	5.11	3.9
10%Ni-CeO_2 rods	10.5	0.05	0.005	11.9	38.1	9.86	2.5

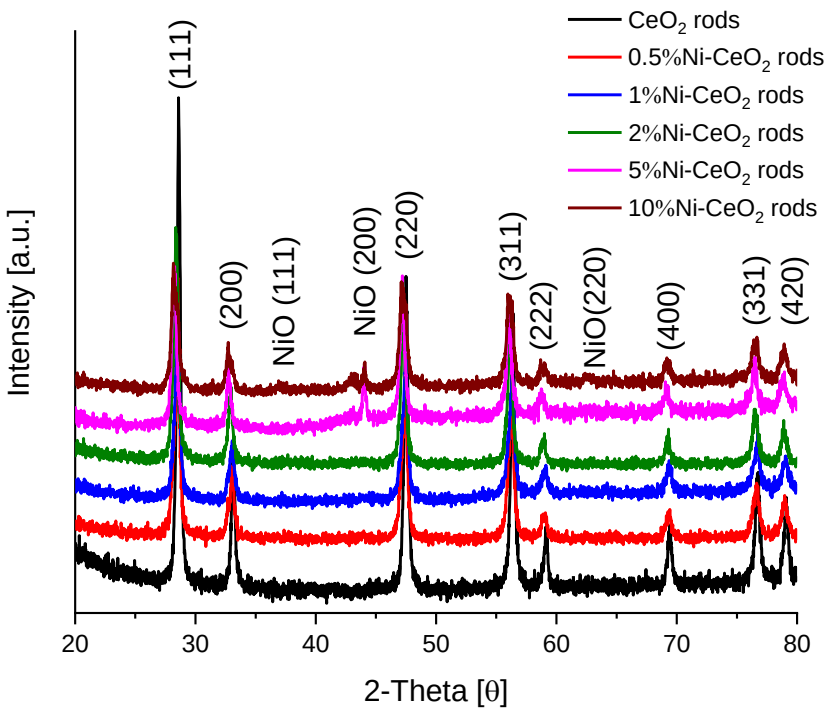

Figure 12. XRD patterns for Ni-CeO_2-rods catalysts.

The XRD patterns of the catalysts are presented in Figure 12. The characteristic peaks of the fluorite structured CeO_2 at 28.5°, 33.1°, 47.5°, 56.4°, 59°, 69.3°, 76.7° and 79.2° corresponding to the (111), (200), (311), (222), (400), (331) and (420) lattice planes are identified (standard JCPDS card no. 34-0394) [32]. Peaks at 37°, 44.1° and 62.6° correspond to NiO (111, 200, 220) according to JCPDS file no. 78-0643 [33]. As can be seen in Figure 12, the Ni-CeO_2 rods diffractograms were characterized by well-defined, intense peaks typical of a fluorite-structured complexion that was preserved after the incorporation of nickel. Moreover, the absence of distinct diffraction peaks for samples containing less than 5% Ni is indicative of the relatively high dispersion of the nickel phases in the samples (Table 4). Cristal size length of CeO_2 was in the range from 25.9 nm to 38.1 nm. Similar results were obtained by Peymani et al. [30] for Ni/CeO_2 rods catalysts with different concertation of Ni (2.5-10%).

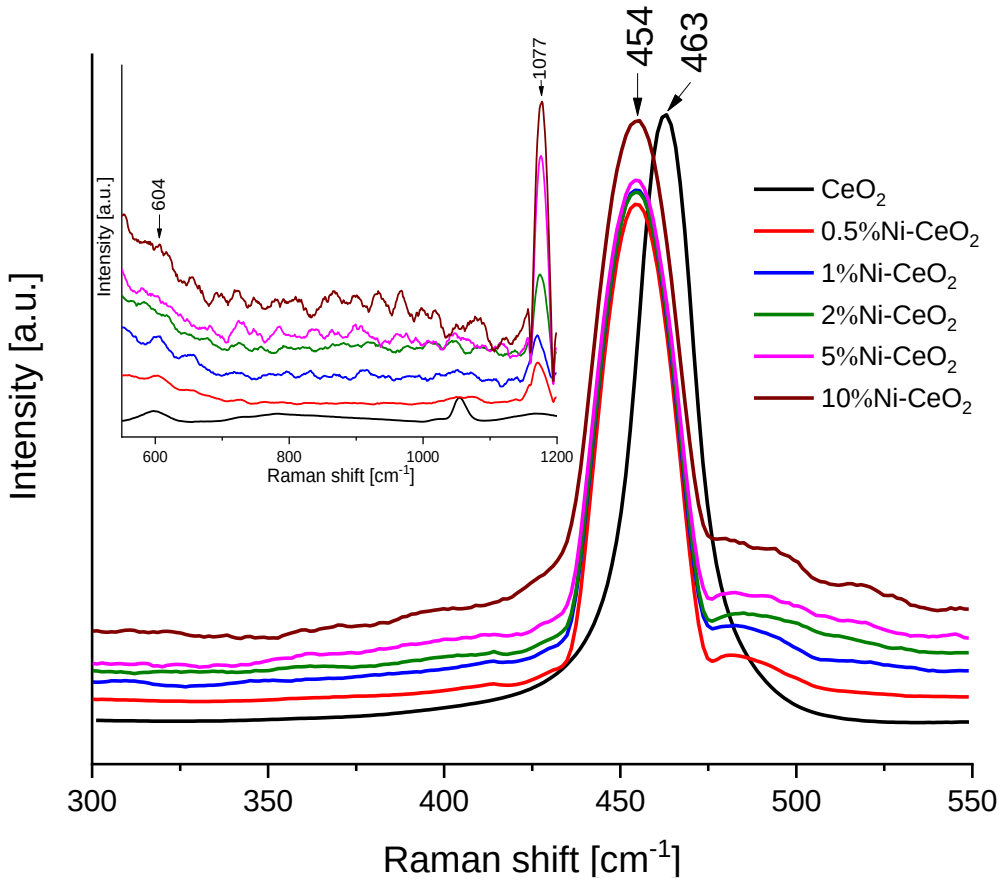

Figure 13. Raman spectra of the Ni-CeO_2 rods catalysts.

To obtain additional structural information of prepared catalysts, Raman spectroscopy was used and the corresponding spectra are presented in Figure 13. All the spectra present a main band at 454-463 cm^{-1}. This band corresponds to the F_{2g} mode of the fluorite structure of cerium dioxide. The position of the peak shifts from 463 cm^{-1} to 454 cm^{-1} for the catalysts modified with nickel. The reason of this shift can depend on various factors like oxygen vacancies, phonon confinement or crystal defects [34,35]. In any case, the peak shift can be related to a strong interaction between the CeO_2 surface and Ni [36] [34]. The peaks observed at 604 and 1177 cm^{-1} correspond to the defect-induced mode (D) and second-order longitudinal optical mode (2LO) bands of ceria, respectively.

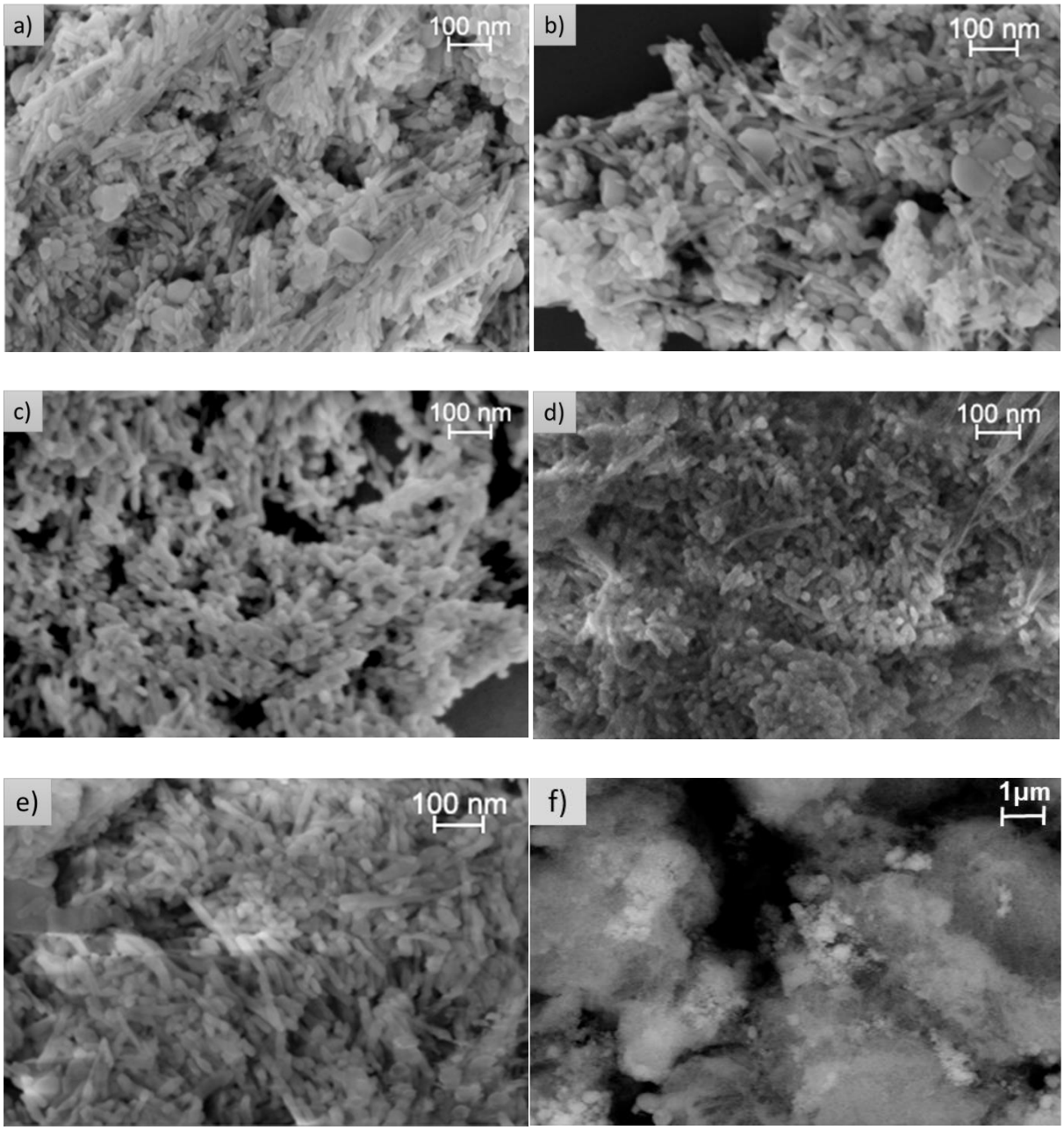

Figure 14. SEM pictures of the Ni-CeO_2 rods catalysts: a) 0.5%-Ni-CeO_2 rods; b) 1%-Ni-CeO_2 rods; c) 2%-Ni-CeO_2 rods; d) 5%-Ni-CeO_2 rods; e) 10%-Ni-CeO_2 rods; f) 2%-Ni-CeO_2 rods-backscattered.

Figure 14 shows SEM images showing the morphologies of the prepared catalysts. It can be seen that the structure has not changed with the ball milling method. Rods shape of cerium oxide has been retained for all prepared catalysts. Figure 14f presents the sample

2%ni-CeO_2-rods measured with the backscattered electrons. The Ni particles could not be seen by backscattered, which means that the nanoparticles are very small and the dispersion is very good.

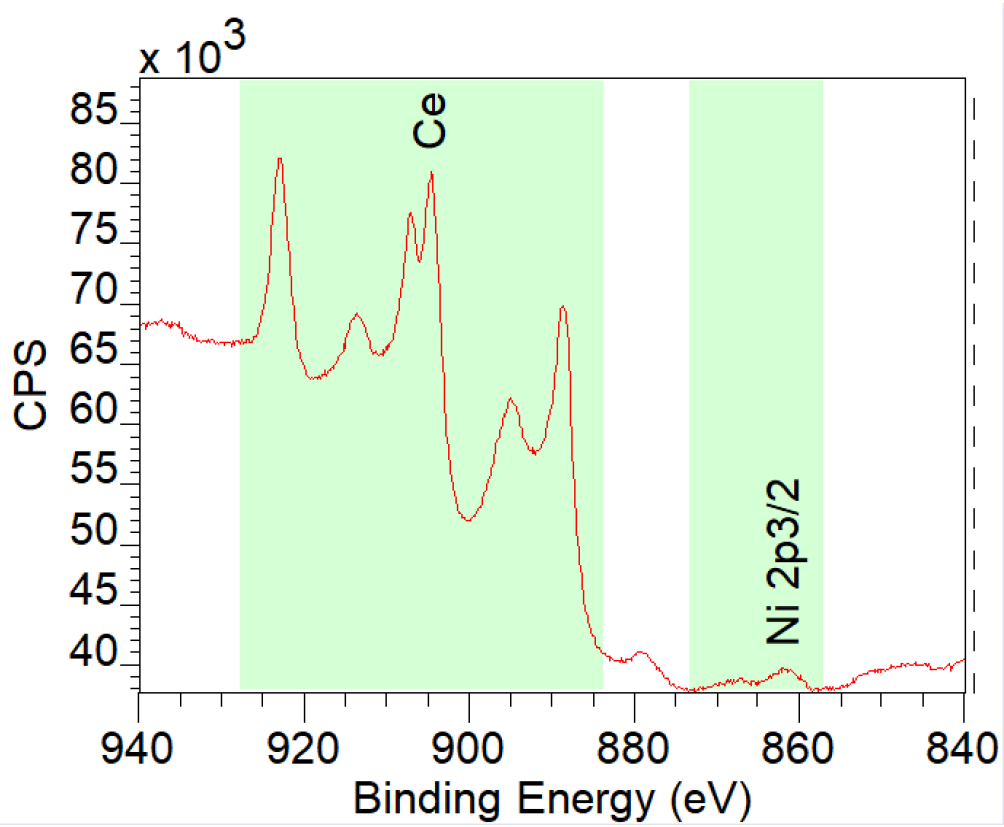

Figure 15. XPS spectra of 2%Ni-CeO_2-rods.

Figure 15 shows XPS spectra of 2%Ni-CeO_2-rods. From the spectra, the atomic concentration on the surface is Ce 91.93% and Ni 8.07%. The Ni signal is weak.

The fact is that the oxidation state of cerium and nickel plays a key role in the interaction with CO_2, and thus in the hydrogenation of this chemically stable molecule [37,38]. Many studies have shown the ability of the skin to activate the CO_2 molecule by a mechanism supported by the oxygen vacancy [39], which of course requires the presence of Ce^{3+} cations at the surface level. Moreover, the oxidation state of nickel is pre-correlated with both the activity and selectivity of supported nickel cerium oxide catalysts [6]. Therefore, it is necessary to characterize in detail the redox properties of the prepared X-Ni-CeO_2

rods catalysts. For this purpose, H_2-TPR and pulse CO_2 chemisorption experiments were carried out on these nanomaterials.

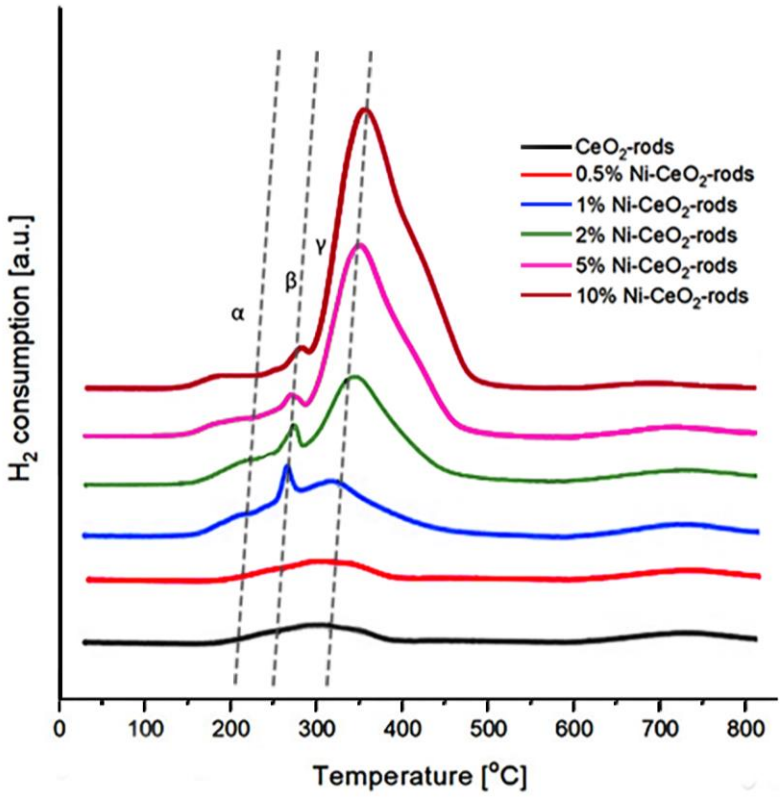

Figure 16. H_2-TPR profiles of Ni-CeO_2 rods catalysts.

Figure 16 shows H_2-TPR of the catalysts. It can be seen that the reduction of all catalysts took place in the temperature range of 150–700 °C. As can be seen, three types of reduction peaks (assigned by the symbols α, β and γ) are observed. The α peak at 150–220 °C can be attributed to the reduction of the surface of the ceria rods and concomitant formation of oxygen vacancies. The peak (β) at 250-280 °C can be attributed mainly to the reduction of NiO weakly interacting with CeO_2 as a support in the catalysts. The γ peak at 310-350°C is ascribed to the reduction of NiO strongly interacting with CeO_2 support [40]. The strong interaction of NiO with CeO_2 leads to a progressive shift of the γ peak to a higher reduction temperature. Moreover, the area of the reduction peaks in the

TPR profile of the catalysts with a higher percentage of nickel was higher than the area detected for the catalysts with a lower nickel content, which was due to the higher amount of hydrogen needed to reduce the catalyst with a higher Ni content, as expected [41].

The quantification of the hydrogen consumption for the Ni-CeO_2 rod samples are compiled in Table 5, along with the CO_2 consumption recorded after the H_2-TPR experiments. In all cases, a good correlation between the oxygen transfer and H_2 consumption was measured for catalysts with Ni content up to 2%. The best reduction ability was measured for 10%Ni-CeO_2 rods and it was about 811.6 µmol/g_{cat}. The highest reoxidation value was achieved for 2%Ni-CeO_2-rods, and it was about 412 µmol/g_{cat}. As the metal content increases, the reduction capability of the catalyst increases. On the other hand, the ability of reoxidation with the participation of CO_2 decreases at high Ni loadings, which is a direct consequence of the increasing size of the Ni nanoparticles as the amount of nickel increases, as confirmed by the XRD analysis. In other words, the oxygen vacancies created at the contact points between Ni and the ceria support is a balance between the loading of Ni and the perimeter available, which is directly related to the size of the Ni particles.

Table 5. The overall amount of hydrogen consumed in H_2-TPR and oxygen consumed in CO_2 pulse chemisorption.

Catalyst	**H_2 consumption [µmol/g_{cat}]**	**CO_2 consumption [µmol/g_{cat}]**
CeO_2 rods	170.1	169.1
0.5%-Ni-CeO_2 rods	179.2	176.8
1%-Ni-CeO_2 rods	352.4	229.1
2%-Ni-CeO_2 rods	453.2	412
5%-Ni-CeO_2 rods	680.1	163.8
10%-Ni-CeO_2 rods	811.6	105.3

1.2.3. Conclusions

Ni-CeO_2 rods catalysts with 0.5−10% wt. Ni were prepared using the ball milling method. The resulting catalysts were characterized by N_2 sorption isotherms, X-ray diffraction, Raman spectroscopy, scanning electron microscopy, H_2-TPR analysis and CO_2 pulse chemisorption. The specific surface area and the pore volume of the obtained catalysts decreased with the increase in the amount of nickel. The XRD analysis show a good crystallization of all catalysts, with peaks assigned to the CeO_2 cubic system and NiO for catalysts with 5% and 10% Ni. Raman spectroscopy shows that the catalysts with nickel generate more surface oxygen vacancies than pure cerium dioxide. SEM microscopy confirms that the structure of the rods of cerium oxide not was destroyed during ball milling preparation. The pulse CO_2 chemisorption results show that the prepared Ni-CeO_2 catalysts possessed a higher CO_2 consumption than pure cerium oxide. 2%Ni-CeO_2 rods catalyst exhibits the best redox properties.

1.3 Molecular dynamics: theory and methods

Molecular simulations allow to study the behavior of catalysts without experimentation. They enable access to microscopic information that would otherwise not be obtained without great effort. Molecular dynamics (MD) techniques are one of the main possibilities for computer experiments. Molecular dynamics is based on a detailed over-time evaluation of a system's dynamic behavior. This paves the way to get information about transport properties as well as a time-dependent response to perturbations [42].

In molecular simulations, because the preparation process involves determining a limited volume and introducing a specific number of molecules into that volume. In a simulation it is calculated how these molecules behave in the force-field built by all molecules.

Finally, the desired properties can be derived from the simulated motion of atoms. This work aimed to briefly introduce MD simulations and present their application to the calculation of the interactions of cerium oxide and water using the GROMACS software package (Groningen Machine for Chemical Simulations).

Molecular Dynamics simulations consists on a numerical calculation method by which Newton's equations of dynamics are solved for a system of N interacting particles:

$$m_i \frac{\partial^2 \vec{r_i}}{\partial t^2} = \vec{F_i}, \text{ i=1… N} \qquad \text{Equation (4)}$$

Where $\vec{F_i}$, is the resultant force acting on the its particle, m_i its mass and $\vec{r_i}$ its position. The forces are the sign-changed gradients of the interaction potentials V ($\vec{r_1}$, $\vec{r_2}$ …, $\vec{r_N}$) that act on each particle of the system:

$$\vec{F_i} = -\vec{\nabla_i} V \qquad \text{Equation (5)}$$

Equations (4) and (5) are solved simultaneously in steps of a given size. The system evolves for some time. If simulation is performed in the NPT ensemble, temperature and pressure is kept within a stipulated range around the required values (for this the package has its respective thermostats and barostats). During the simulation atomic coordinates are recorded at regular intervals. The latter as a function of time represent the trajectory of the system. After the initial simulation steps, the system will tend to reach a state of equilibrium, in which it minimizes its potential energy. Many macroscopic properties can then be then extracted from the output data, when averaged over an equilibrium path.

1.3.1. In silico experiments

Computer simulation is one of the latest tools for performing in silico experiments complementing the experimental work. The main goal of computer simulations is to mimic the experiments to replicate the reactions taking place at the atomic level. This helps to explain the experimental results.

Molecular dynamics simulations calculate the movement of atoms in light of positions, velocities, forces, and orientations over time. Thus, MD creates a series of

configurations based on the initial configuration and speed. A set of numerical integration algorithms are used to calculate the equations of motion. This integration is done in a way that Pressure, Temperature or both can be kept constant. In the case of simulations carried out in this work, the temperature was 300 K and the pressure was 0.1 MPa and were checked to be constant in the time of 200 ns.

1.3.2. Non-bonded interactions

Non-bonded interactions are those taking place between atoms that are not directly linked. Therefore, for small molecules such as water, it only affects inter-atomic interaction. On the other hand, cerium oxide is a crystal formed by atoms, thus, they are only affected by non-bonded interactions.

There are two potential functions to describe non-bonded atoms: Coulomb interactions between electrostatic charges and Van der Waals interactions, which is usually modelled by Lennard-Jones (LJ), Morse or Buckingham potentials. In van der Waals interaction, atoms with no net electrostatic charge will still tend to attract each other at short distances or tend to repel each other when they get too close. In the case of Buckingham, this potential is defined as:

$$\phi_{12}(r) = \mathrm{Aexp}(-\mathrm{Br}) - \frac{C}{r^6} + \frac{q_1 q_2}{4\pi\varepsilon_0 r} \qquad \text{Equation (6)}$$

where A, B, C and are suitable constants and the additional term is the electrostatic potential energy.

In electrostatic interactions, atom charges are involved in interactions. Opposite atom charges attract and the same atom charges repel each other. In this potential, the force of the attraction is inversely proportional to the square of the distance between atoms:

$$\mathrm{F} = \mathrm{k}\frac{q_1 q_2}{d^2} \qquad \text{Equation (7)}$$

Where F is the magnitude of repulsion or attraction force between two charged objects; q_1 and q_2 are the electrical charge of the atoms, d is the distance between the center of the two charged objects, and k is a constant that depends on the medium in which charged objects are placed.

1.3.3. Empirical force field

The most important step in the simulation of molecular dynamics is describing the atomic interactions of a molecular system, the so-called force field [43]. The force field is constructed to cover all relevant molecular interactions that will model molecular behaviour. The first step to construct a realistic atomic model is to evaluate the forces. The force F_i at time t is determined by the potential energy gradient concerning the particle position coordinates and according to:

$$\vec{F_i} = -\vec{\nabla} \ V_i \qquad \text{Equation (8)}$$

The potential energy V can be calculated as bonded (intra-molecular) and non-bonded (intermolecular) interactions:

$$E(R) = \sum_{bonded} E_i(R) + \sum_{non-bonded} E_i(R) \qquad \text{Equation (9)}$$

However, as aforementioned, in our case we will find no bonded interactions for cerium oxide and bonded for water molecules.

1.3.3.1. Description of the force-field to simulate cerium oxide

Calculating the forces acting on every atom in the system is the most time-consuming step in a simulation. The forces considered are the long-range forces between atoms such as the electrostatic one, and the short-range Van der Waals forces between two atoms, both of which dictate how the atoms interact with each other. The forces used for an individual simulation must be determined by testing in-silico some of the properties of the material being simulated. For a highly ionic material such as ceria, forces between the interacting atoms can be approximated using a combination of long-range and short-range potentials.

The long-ranged forces in the crystal that were used in this study of ceria can be described by Coulomb's Law (Equation 7). Short-range force-field was taken from the publication by Sayle et al. [44] but it was necessary creating a force field for the tested system, consisted of transforming the Morse potential into a Buckingham potential to perform simulations. Conversion of Morse potential to Buckingham potential was described by Liam and Dawson [45].

1.3.3.2. Description of the force-field to simulate water

Many water models are available in the literature for an accurate representation of water. The most common ones are often distributed together with the force fields described above. These models have been parametrized to reproduce physical and thermodyc properties such as the density, enthalpy of vaporization, radial distribution functions, energies of hydration or dipole moment. They can be classified by the number of points used to define the model (atoms plus dummy sites), whether the structure is right or flexible, and whether the model includes polarization effects or not. The simplest and most popular model for MD are TIP3P [46], which has three interaction sites, corresponding to the three atoms of the water molecule with rigid geometry. Each atom has a point charge assigned and the oxygen atom is described by Lennard-Jones parameters. The more complex 4-site or 5-site molecules such as TIP4P and TIP5P, respectively, place the negative charge on either a dummy atom placed near the oxygen along the bisector of the HOH angle or two dummy atoms representing the lone pairs of the oxygen atom. These models improve the electrostatic distribution around the water molecule though to a large computational cost because of the large number of electrostatic interactions to compute. Because TIP3P has been shown to provide a good compromise between quality and computational cost, it has been chosen as the water model for all simulations that are part of this thesis.

1.3.4. Simplifications and computational aspects

1.3.4.1. GROMACS

GROMACS is a free software for molecular dynamics simulations and the subsequent analysis and evaluation of the generated data. It was developed in the 1990s at the University of Groningen (Sweden) and is now maintained by universities and research centers around the world. A practical introduction to GROMACS can be found in the chapter below. More detailed descriptions of the various methods and commands can be found in the GROMACS user manual [47] and on the GROMACS website [48].

1.3.4.2. Length and time scales in molecular dynamics

All molecular phenomena occur on length scales of nanometers. This is the common unit in which all coordinates and dimensions are stated in GROMACS. Typically, atom velocities observed in MD simulations are in the range from 0.01 to 1.0 nm ps^{-1}. MD simulation times for full equilibration can range from only a few picoseconds up to multiple microseconds, depending on system size and constitution. For numerical stability and accuracy, the time step size must be chosen according to the smallest time scale, usually bond vibrations (≈ 10^{-3} ps).

1.3.5. Molecular simulations with GROMACS

The basic procedure for performing a molecular simulation in GROMACS is outlined in figure 17, together with the most important file types that are produced in these steps. Positions and velocities of all atoms are the main outcome of MD simulations as they result from solution of the equations of motion.

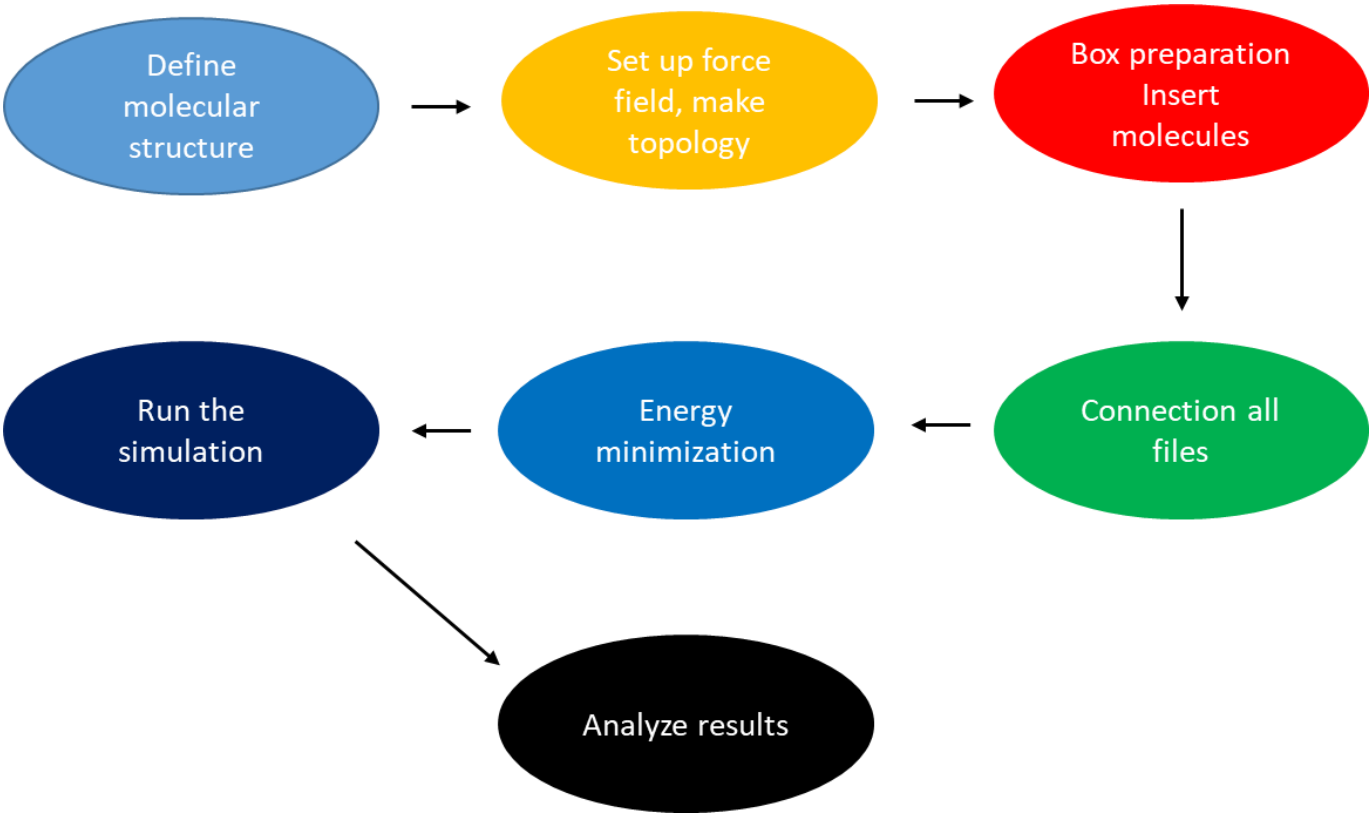

Figure 17. Steps of a GROMACS simulations.

1.3.5.1. Definition of molecular structures

To perform the simulations a slab of Cerium Oxide was generated cut along the perpendicular to [111] crystallographic direction. The structure of cerium oxide was obtained on the basis of the standard cubic structure from crystallographic data, which is available in the "The Material Projects" database [49]. The constructed structure is then saved as a .pdb file containing information about the type of atoms in the molecule, their position, and connections. A sample of a .pdb file used in our work is shown in Figure 18.

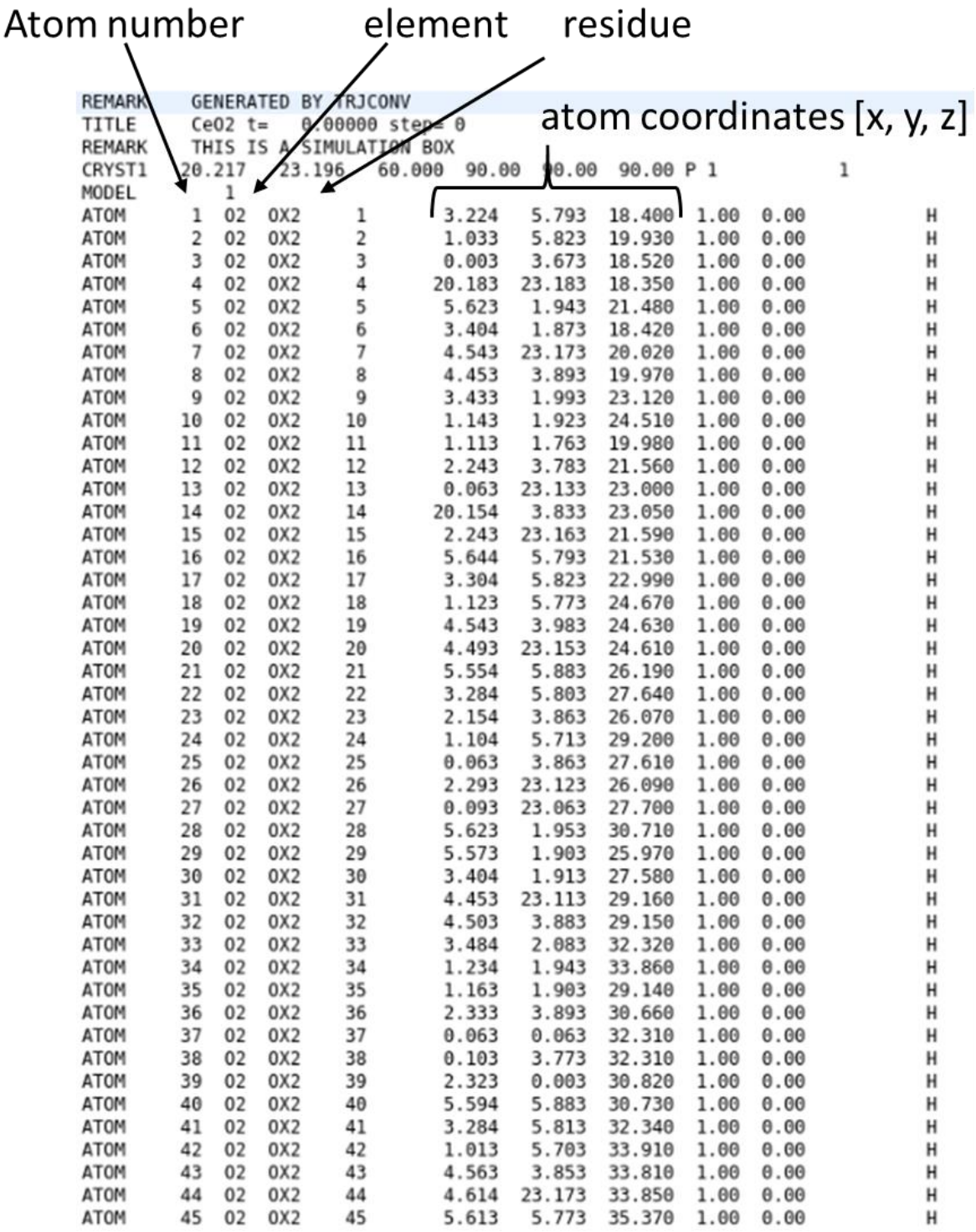

Figure 18. The .pdb file cerium oxide molecule.

1.3.5.2. Force field and topology

The next step is to set up the force field and generate the topology file. It is an essential step in preparing the simulation as it has a significant impact on the quality of the results.

Force field

Force field parameters were obtained from the parameter transformation that was determined by Sayle et al. [3]. The determination of these parameters consisted in transforming the data that was determined for the Morse potential into parameters consistent with Buckingham's potential. The Lennard Jones potential was used for water molecules. A summary of he potential parameters are given in Table 6. The potential models, used to describe the interactions between CeO_2 and water, were derived using Lorenz-Berthelot rules and the data from Sayle et al. [3].

Table 6. Potential parameters for all simulations.

Species	A [kJ mol^{-1}]	B [nm^{-1}]	C_6 [kJ mol^{-1} nm^{-6}]
O_2-Ce^{4+}	880143	38.67	0.01248
O_2-O_2	995833	38.91	0.00844
Ce^{4+}-Ce^{4+}	0	0	0
Ce^{4+}-OW	10060000	49.94	0.00682
O_2-OW	1633000	39.88	0
OW-OW	49650000	56.54	0.000805
Ce^{4+}-Ce^{3+}	0	0	0
O_2-Ce^{3+}	880143	38.67	0.01248
Ce^{3+}-Ce^{3+}	0	0	0
Ce^{3+}-OW	10060000	49.94	0.0682

Topology

A topology file (.top) can be thought of as a dataset that contains all the constant attributes of the molecular system, i.e. references to all force field parameter files, functional terms, the force field, and the number of all species particles to be introduced in step 3, Figure 19. In contrast, dynamic attributes, such as positions and velocities that are generated during the simulation run, are stored in coordinate and trajectory files. Since the CeO_2 slab and water will be initiated separately, we need to generate two topologies. The compound and number of molecules should be given in the order they are inserted during the box making process. Therefore, creating a topology can be done after step 3.

```
[system]
CeO2/H2O

[molecules]
OX2        576
Ce4        286
SOL         29
```

Figure 19. Topology .top file.

At this stage, we also have to decide the number of molecules that will be simulated. Reducing this number increases the statistical impact on the results and reduces the quality of the data generated. In contrast, a large number of molecules increases the computation time. Therefore, a compromise must be found.

1.3.5.3. Preparing the simulation box

We have prepared the simulation box, after creating the CeO_2 slab, inserting water molecules. The box is initialized and filled step by step for each water molecule. The configuration file is a .gro file with positions (and speed) that simply contains the positions of all the atoms. In this case, the box was prepared with the size of 2 x 2.3 x 6 Å. Then, in the box were placed 288 cerium atoms of a slab of cerium oxide (CeO_2) as an intentional set and 29 molecules of water. Figure 20 visualizes the simulation box with the molecules inside.

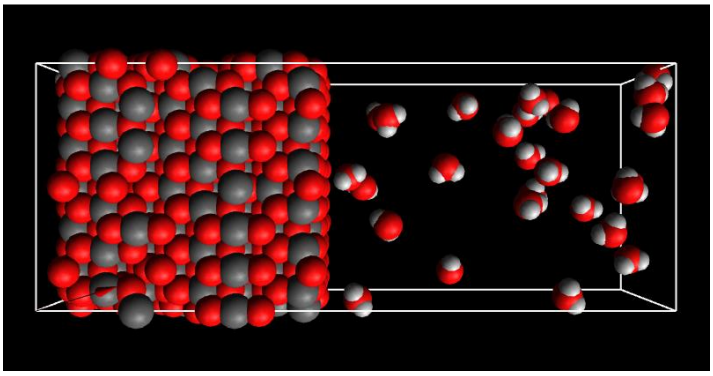

Figure 20. Initial configuration of the CeO_2 slab and water molecules.

1.3.5.4. Merging of files, initialization of simulation

The actual MD simulation start command in GROMACS requires a single input file that contains all necessary information. Therefore, in this step all data files are merged to a .tpr file. Prior to this, we have to define all simulation settings. These are listed in a .mdp file. (figure 21).

```
; RUN CONTROL PARAMETERS =
integrator               =  md
; start time and timestep in ps =
tinit                    = 0
dt                       = 0.002
nsteps                   = 100000
; number of steps for center of mass motion removal =
nstcomm                  = 100
comm_grps                = OX2 Ce4 SOL Ce3
; OUTPUT CONTROL OPTIONS =
; Output frequency for coords (x), velocities (v) and forces (f) =
nstxout                  = 10
nstvout                  = 0
nstfout                  = 0
; Output frequency for energies to log file and energy file =
nstlog                   = 100
nstenergy                = 100
energygrps               = OX2 Ce4 SOL Ce3
; NEIGHBORSEARCHING PARAMETERS =
; nblist update frequency =
nstlist                  = 10
; ns algorithm (simple or grid) =
ns_type                  = grid
; Periodic boundary conditions: xyz or none =
pbc                      = xyz
; cut-off scheme
cutoff-scheme = Group
; nblist cut-off         =
rlist                    = 1.
; OPTIONS FOR ELECTROSTATICS AND VDW =
; Method for doing electrostatics =
coulombtype              = pme
rcoulomb                 = 1.
; Dielectric constant (DC) for cut-off or DC of reaction field =
epsilon-r                = 1
; Method for doing Van der Waals =
; cut-off lengths        =
vdw-type                 = Cut-off
rvdw                     = 1.
;OPTIONS FOR TEMPERATURE COUPLING
tcoupl                   = v-rescale
tc_grps                  = OX2 Ce4 SOL Ce3
tau_t                    = 0.5 0.5 0.5 0.5
ref_t                    = 300 300 300 300
;OPTIONS FOR PRESSURE COUPLING
pcoupl                   = no
;tau_p                    = 0.5
;compressibility          = 4.5e-05
;ref_p                    = 1.0
; GENERATE VELOCITIES FOR STARTUP RUN =
gen_vel                  = yes
;gen_temp                 = 300
;gen_seed                 = -1
; OPTIONS FOR BONDS     =
constraints              = all-bonds
```

Step size and simulation time

Figure 21. File structure simulation settings.

1.3.5.5. Energy minimization

Although atom coating is avoided, the insertion procedure can still result in an incorrect molecular arrangement. This is avoided by minimizing the energy of the system, until equilibrium is reached. This will be a good starting point for the actual simulation.

1.3.5.6. Simulation

The idea of the undertaken simulation is to reproduce the conditions in the experiments. Therefore, some additional changes must be done to reproduce experimental conditions.

The simulations consisted of modifying the structure of cerium oxide (face [111]) by creating defects on its surface. Special care must be taken to keep the total charge of the system neutral. Five different simulations were carried out, which consisted on a variable number of defects on the cerium oxide surface and the location of defects. The first simulation consisted in making two vacancies on the surface of the structure (called Simulation 1-2 defects). The second (Simulation 2-4 close defects) and the third (Simulation 2-4 far defects) consisted in the creation of four: Two cases were explored: one where vacancy positions are next to each other and another one for which vacancies are located away from each other. In the case of the fourth (Simulation 3-6 close defects) and fifth (Simulation 3-6 far defects) simulations, the same step was applied as in the case of the previous two, except that the difference with the number of vacancies was increased to six. For each simulation, the system is presented in Table 7.

Table 7. Initial system compounds of each simulation.

Simulation	O_2	Ce^{4+}	Ce^{3+}	H_2O
Inicial system	576	288	0	29
Simulation 1-2 defects	574	284	4	29
Simulation 2-4 close defects	572	280	8	29
Simulation 2-4 far defects	572	280	8	29
Simulation 3-6 close defects	570	276	12	29
Simulation 3-6 far defects	570	276	12	29

The presence of oxygen vacancies and Ce^{3+} ions at the surface play an important role in the promoter/catalyst properties of CeO_2. The defect studies were carried out on the [111] surface as this face is present if ceria is grown non-stoichiometrically. Two defect configurations were investigated. The first configuration was based on the formation of side-by-side defects, namely the removal of oxygen atoms from Ce^{4+} and the creation of a free Ce^{3+} vacancy that would be available for oxygen from the water molecule. The second configuration, on the other hand, was to create defects located far away from each other. In the first simulation, 2 defects were made. It consisted in removing 2 oxygen atoms from the initial system and changing the oxidation state of 4 cerium atoms from Ce^{4+} to Ce^{3+}. This is shown in figure 22.

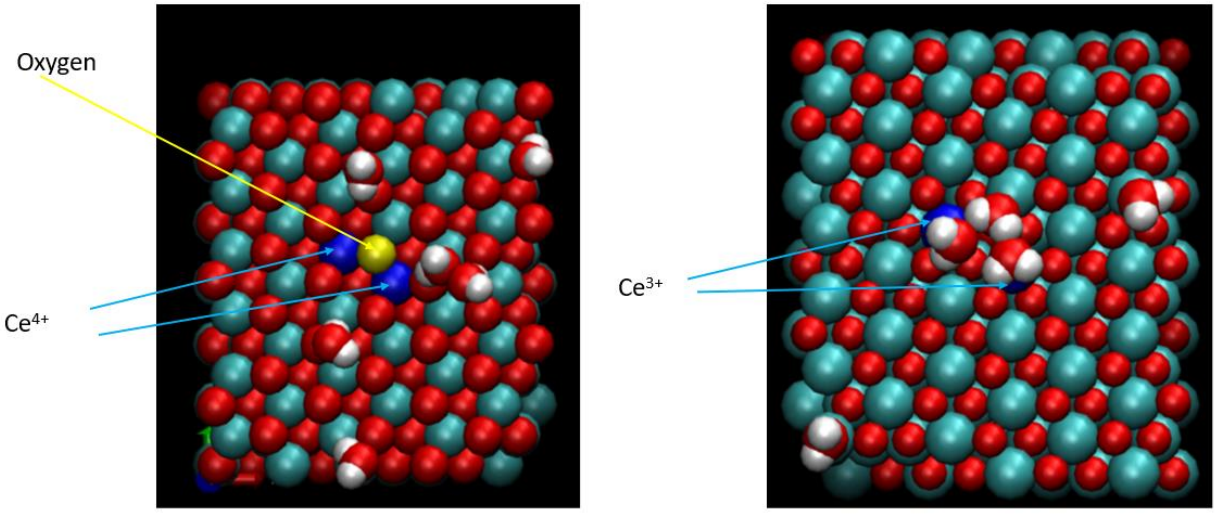

Figure 22. Defects of simulation 1-2 defects.

The second and third simulations consisted in doubling the number of defects to four. In the case of the second simulation, these were defects created close to each other (Simulation 2-4 close defects), while in the case of the third simulation, these were defects created far from each other (Simulation 2-4 far defects). The defects formed are illustrated in figure 23.

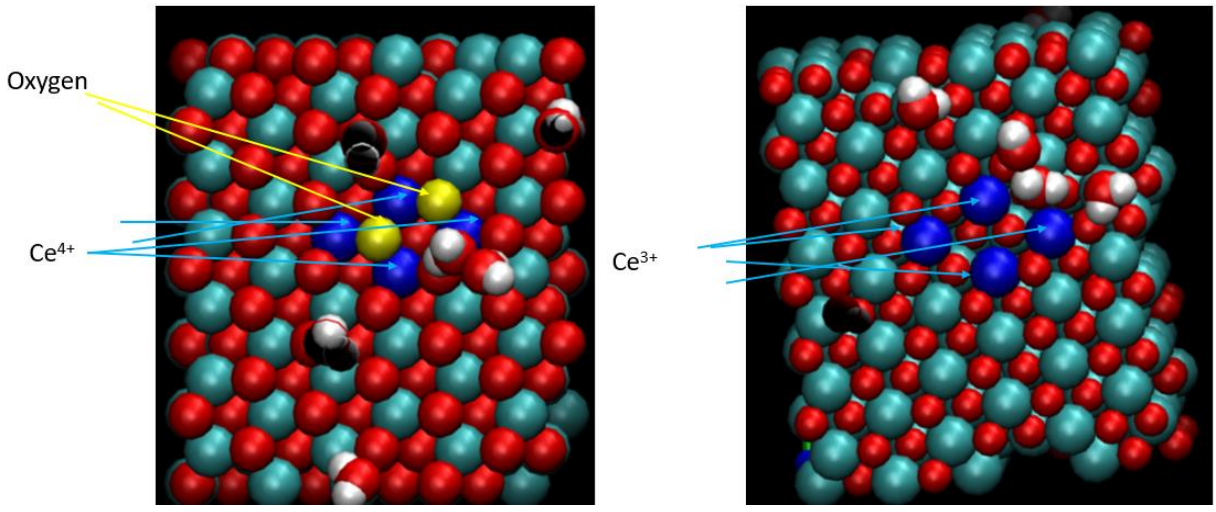

Figure 23. Defects for the simulation 2 and 3: a) Simulation 2-4 close defects; b) Simulation 2-4 far defects.

In the case of the fourth and fifth simulations, the number of created defects was 6, creating 12 vacancies. As in the case of simulation, two and three defects were created close to each other (3-3 close) and away from each other (3-3 far) what show figure 24.

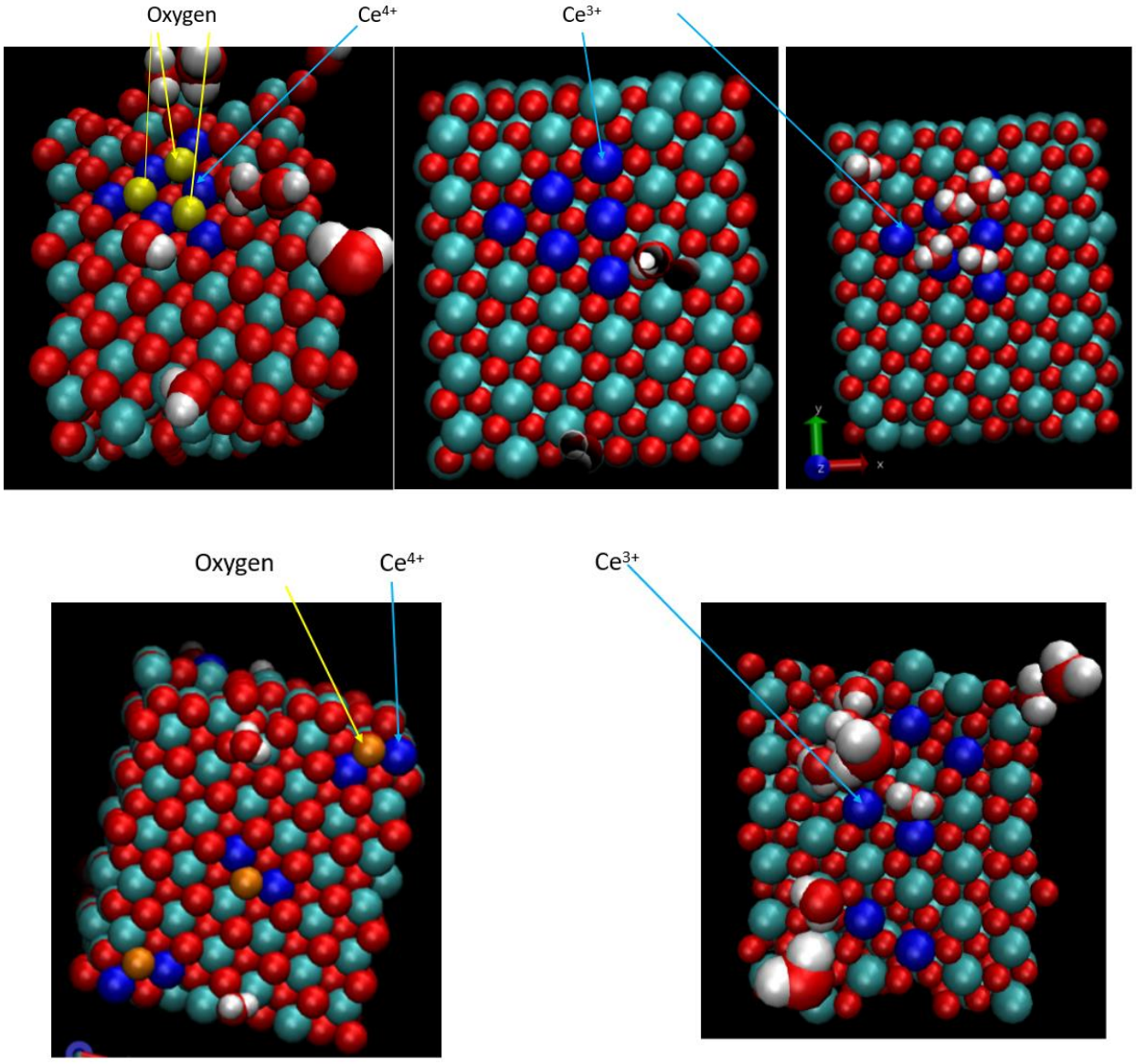

Figure 24. Defects of the simulation 4 and 5: a) Simulation 3-6 close defects; b) Simulation 3-6 far defects.

1.3.5.7. Results

Besides performing molecular simulations, GROMACS enables the user to analyze generated trajectory and energy data. For each simulation, conditions were strictly the same.

Based on the performed simulations, the distance between the free Ce^{3+} vacancies and the H_2O water molecules that directly interacted with them on each simulation's time function are shown (Figure 25-27).

It was found that in the case of the first simulation (simulation 1-2 defects), taking up all the free vacancies formed by oxygen atoms from water took 125 ns (figure 25). In the second (Simulation 2-4 close defects) and third simulation (Simulation 2-4 far defects), it was noticed that the occupation of all vacancies by oxygen atoms from the oxygen from water was faster in the case of defects formed close to each other than distant from each other (figure 26). A similar correlation was observed in the case of the fourth (Simulation 3-6 close defects) and fifth simulations (Simulation 3-6 far defects) (figure 27).

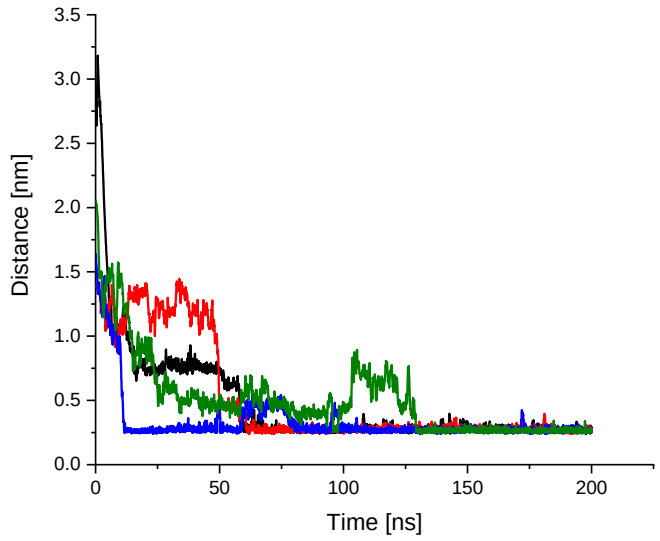

Figure 25. Distance between each defect and the water molecules that occupies the defect in equilibrium for 1-2 defects.

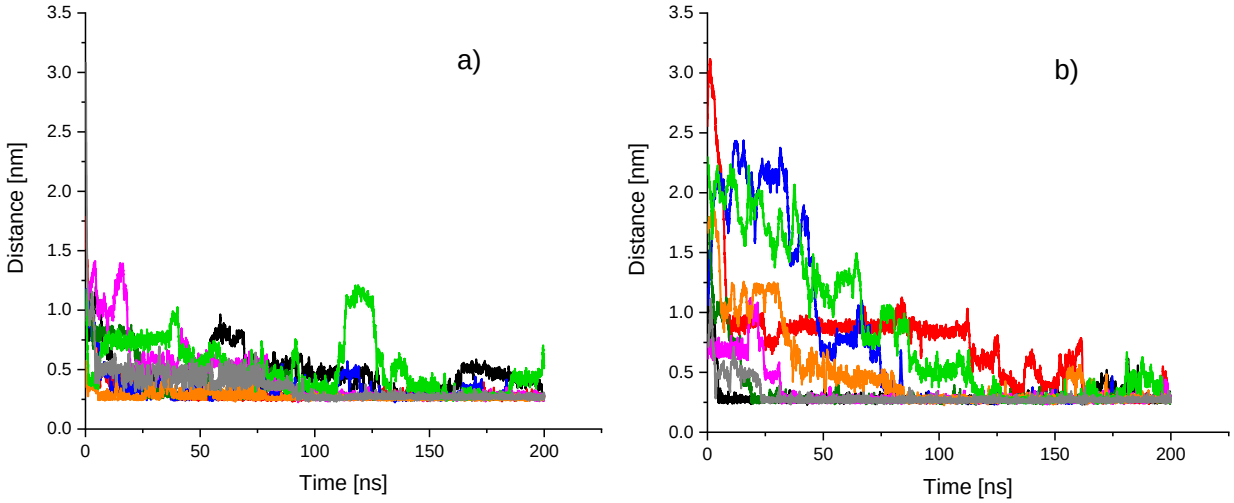

Figure 26. Distance between each defect and the water molecules that occupies the defect in equilibrium a) Simulation 2-4 close defects; b) Simulation 2-4 far defects.

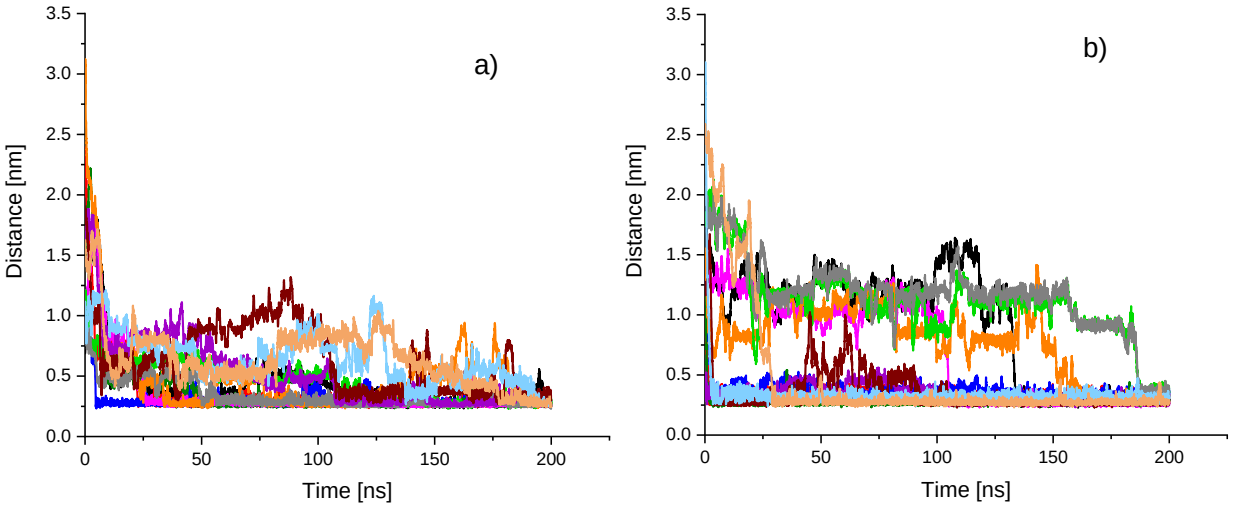

Figure 27. Distance between each defect and the water molecules that occupies the defect a) Simulation 3-6 close defects; b) Simulation 3-6 far defects.

We have also calculated the occupancy of each defect as a function of time. A defect is counted as occupied when the distance between water oxygen and Ce^{3+} is below 0.4 nm. In each time step, we count the number of defects for which this is the case. Figure 28 shows that all of the defects were occupied on each simulation and confirm that the defects made close to each other are occupied quicker than defects with the distance.

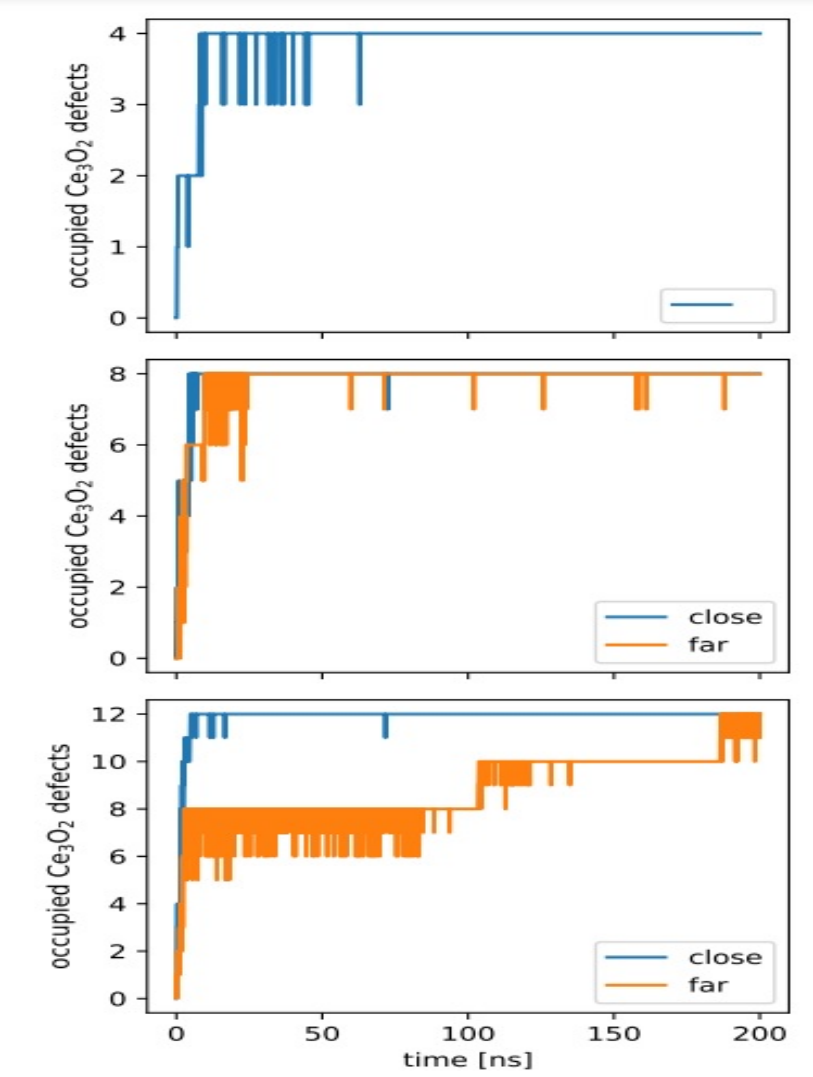

Figure 28. Number of occupied defects in relation to time.

1.3.6. Conclusions

In summary, the present results show that water molecules readily interact with the oxygen vacancies of ceria. This leads to the splitting of water molecules and the release of hydrogen. Importantly, it is found that the reaction between oxygen vacancies in ceria and water vapor occurs faster for defects forming close to each other. This means that clustering of oxygen vacancies in ceria plays an important role and it is advantageous for

the thermochemical water splitting process, and possibly for the thermochemical CO_2 reduction. This may inspire the design of novel catalysts for this purpose.

References

[1] S. Perathoner, G. Centi, CO_2 Recycling: A key strategy to introduce green energy in the chemical production chain. ChemSusChem 2014, *7*, 1274–1282. doi.org/10.1002/cssc.201300926

[2] A. Barroso-Bogeat, G. Blanco,J.J. Pérez-Sagasti, C. Escudero, E. Pellegrin,F.C. Herrera, J.M. Pintado, Thermocatalytic CO2 Conversion over a Nickel-Loaded Ceria Nanostructured Catalyst: ANAP-XPS Study.Materials2021,14,711. doi.org/10.3390/ma14040711

[3] M. Aresta, A. Dibenedetto, A. Angelini, The changing paradigm in CO2utilization. J. CO2 Util. 2013, 3–4, 65–73. doi.org/10.1016/j.jcou.2013.08.001

[4] D. Yadav, R. Banerjee, A review of solar thermochemical processes. Renew. Sustain. Energy Rev. 2016, 54, 497–532. doi.org/10.1016/j.rser.2015.10.026

[5] A. Farooqui, A. Bose, D. Ferrero, J. Lorca, M. Santarelli, Simulation of two-step redox recycling of non-stoichiometric ceria with thermochemical dissociation of CO2/H2O in moving bed reactors -Part II: Techno-economic analysis and integration with 100 MW oxyfuel power plant with carbon capture. Chem. Eng. Sci. 2019. doi.org/10.1016/j.ces.2019.03.050

[6] C. Agrafiotis, M. Roeb, C. Sattler, A review on solar thermal syngas production via redox pair-based water/carbon dioxide splitting thermochemical cycles. Renew. Sustain. Energy Rev. 2015, 42, 254–285. doi.org/10.1016/j.rser.2014.09.039

[7] M. Roeb, M. Neises, N.Monnerie, F. Call, H. Simon, C.Sattler, M. Schmcker, R. Pitz-Paal, Materials-related aspects of thermochemical water and carbon dioxide splitting: A review. Materials (Basel).2012, 5, 2015–2054. doi.org/10.3390/ma5112015

[8] S. Bernal, G. Blanco, J.M. Gatica, J.A. Perez-Omil, J.M. Pintado, H. Vidal, Chemical reactivity of binary rare earth oxides. In Binary Rare Oxides; Adachi, G., Imanaka, N., Kang, Z.C., Eds.; Springer: Dordrecht, The Netherlands, 2004; pp. 9–55. ISBN: 978-1-4020-2569-3.

[9] A. Trovarelli, Catalytic properties of ceria and CeO_2-containing materials. Catal. Rev. 1996, 38, 439–520. doi.org/10.1080/01614949608006464

[10] F.W. Chang, M.S. Kuo, M.T. Tsay, M.C. Hsieh, Hydrogenation of CO_2 over nickel catalysts on rice husk ash-alumina prepared by incipient wetness impregnation. Appl. Catal. A Gen. 2003, 247, 309–320. doi.org/10.1016/S0926-860X(03)00181-9

[11] G. Du, S. Lim, Y. Yang, C. Wang, L.Pfefferle, G.L. Haller, Methanation of carbon dioxide on Ni-incorporated MCM-41 catalysts: The influence of catalyst pretreatment and study of steady-state reaction. J. Catal. 2007, 249, 370–379. doi.org/10.1016/j.jcat.2007.03.029

[12] A. Trovarelli, J. Llorca, . Ceria Catalysts at Nanoscale: How Do Crystal Shapes Shape Catalysis? ACS Catalysis, 2017, 7, 4716-4735. doi.org/10.1021/acscatal.7b01246

[13] Q. Yang, X. Fu, C. Jia, C. Ma, X. Wang, J. Zeng, R. Si, Y. Zhang, C. Yan, Structural determination of catalytically active subnanometer iron oxide clusters. ACS Catal.,2016, 6, 3072−3082. doi.org/10.1021/acscatal.6b00328

[14] Y. Li and W. Shen: Morphology-dependent nanocatalysts: rod-shaped oxides. Chem. Soc. Rev.2014, 43, 1543-1574. doi.org/10.1039/C3CS60296F

[15] B. Solsona, R. Sanchis, A.M. Dejoz, T. García, L. Ruiz-Rodríguez, J.M. López Nieto, J.A. Cecilia, E. Rodríguez-Castellón, Total Oxidation of Propane Using CeO_2 and CuO-CeO_2 Catalysts Prepared Using Templates of Different Nature. Catalysts 2017, *7*, 96. doi.org/10.3390/catal7040096

[16] A. Zicko Johannes et al 2020 IOP Conf. Ser.: Mater. Sci. Eng. 823 012030

[17] P. Makuła, M. Pacia, W. Macyk, How To Correctly Determine the Band Gap Energy of Modified Semiconductor Photocatalysts Based on UV–Vis Spectra, J. Phys. Chem. Lett. 2018, 9, 23, 6814–6817. doi.org/10.1021/acs.jpclett.8b02892

[18] G. Rao, H. Sahu, XRD and UV-Vis diffuse reflectance analysis of CeO2–ZrO2solid solutions synthesized by combustion method. Proc. Indian Acad. Sci. (Chem. Sci.), Vol. 113, Nos 5 & 6, October–December 2001, pp 651–658.

[19] P. Patsalas, S. Logothetidis, L. Sygellou, S. Kennou, Structure Dependent Electronic Properties of Nanocrystalline Cerium Oxide Films. Phys. Rev. B: Condens. Matter Mater. Phys. 2003, 68, 035104. doi.org/10.1103/PhysRevB.68.035104

[20] A. Filtschew, K.Hofmann, Ch. Hess, Ceria and Its Defect Structure: New Insights from a Combined Spectroscopic Approach, J. Phys. Chem. C 2016, 120, 6694−6703, doi.org/10.1021/acs.jpcc.6b00959

[21] N. Kainbayev, M. Sriubas, D. Virbukas, Z. Rutkuniene, K. Bockute, S. Bolegenova, G. Laukaitis, Raman Study of Nanocrystalline-Doped Ceria Oxide Thin Films. *Coatings* 2020, *10*, 432. doi.org/10.3390/coatings10050432

[22] W.H. Weber, K.C. Hass, J.R. McBride, Raman study of CeO2: Second-order scattering, lattice dynamics, and particle-size effects, Phys Rev B Condens Matter. 1993 Jul 1;48(1):178-185. doi.org/10.1103/physrevb.48.178.

[23] J.R. McBride, K.C. Hass, B.D. Poindexter, W.H. Weber, Raman and X-Ray Studies of Ce1−xRexO2−y, Where Re = La, Pr, Nd, Eu, Gd, and Tb. J. Appl. Phys. 1994, 76, 2435−2441. doi.org/10.1063/1.357593

[24] W.H. Weber, K.C. Hass, J.R. McBride, Raman-Study of CeO2: Second Order Scattering, Lattice-Dynamics, and Particle-Size Effects. Phys. Rev. B: Condens. Matter Mater. Phys. 1993, 48, 178−185. doi.org/10.1103/PhysRevB.48.178

[25] T. Taniguchi, T. Watanabe, N. Sugiyama, A.K. Subramani, H. Wagata, N. Matsushita, M. Yoshimura, Identifying Defects in Ceria-Based Nanocrystals by UV Resonance Raman Spectroscopy. J. Phys. Chem. C 2009, 113, 19789−19793. doi.org/10.1021/jp9049457

[26] J.R. McBride, K.C.Hass, B.D. Poindexter, W.H. Weber, Raman and X-Ray Studies of Ce1−xRexO2−y, Where Re = La, Pr, Nd, Eu, Gd, and Tb. J. Appl. Phys. 1994, 76, 2435−2441. doi.org/10.1063/1.357593

[27] M. Piumetti, S.Bensaid, N. Russo, D. Fino, Nanostructured ceria-based catalysts for soot combustion: Investigations on the surface sensitivity. Appl. Catal. B 2015, 165, 742–751. doi.org/10.1016/j.apcatb.2014.10.062

[28] P. Miceli, S. Bensaid, N. Russo, D. Fino, CeO2-based catalysts with engineered morphologies for soot oxidation to enhance soot-catalyst contact. Nanoscale. Res. Lett. 2014, 9, 254. doi.org/10.1186/1556-276X-9-254

[29] G. Leofanti, M. Padovan, G. Tozzola, B. Venturelli, Surface area and pore texture of catalysts, Cat. Today, 41, 1998, 207-219. doi.org/10.1016/S0920-5861(98)00050-9

[30] M. Peymani, S. M. Alavi, H. Arandiyan, M. Rezaei, Rational Design of High Durface Area mesoporous Ni/CeO2 for Partial Oxidation of Propane, Catalysts, 2018, 8, 388. doi.org/10.3390/catal8090388

[31] S. Damyanova, B. Pawelec, R. Palcheva, Y. Karakirova, M.C. Capel Schanez, G. Tyuliev, E. Gaigneaux, J. L.G. Fierro, Strucutre and Surface properties of ceria- modified Ni-based catalysts for hydrogen production. Appl. Catal. B Environ.,, 2018, 5, 340-353. doi.org/10.1016/j.apcatb.2017.12.002

[32] F. A. Al-Agel, E. Al-Arfaj, A.A. Al-Ghamdi, Y. Losovyj, L.M. Bronstein, W.E. Mahmoud, A novel recipe to improve the magnetic properties of Mn doped CeO2 as a room temperature ferromagnetic diluted metal oxide, J. Mang. Mater; 2014, 360, 73-79. doi.org/10.1016/j.jmmm.2014.02.013

[33] S. Rakshit, S. Ghosh, S. Chall, S. S. Mati, S.P. Moulik, S. Ch. Bhattacharya, Controlled synthesis of spin glass nickel oxide nanoparticles and evaluation of their potential antimicrobial: A cost effective and eco friendly approach, RSC Advances, 2013, 3, 19348. doi.org/10.1039/C3RA42628A

[34] X. Liu, L. Han, W. Liu, Y. Yang, Synthesis of Co/Ni Unitary-or Binary-Doped CeO2 mesoporous Nanospheres and Their Catalytic Performance for CO Oxidation, Eur. J. Inorg. Chem., 2014, 28, 742-746. doi.org/10.1002/ejic.201402570

[35] D. Qiao, G. Lu, Y. Guo, Y. Wang, Y. Guo, Effect of water vapor on the CO and CH4 catalytic oxidation over CeO2-MOx (M=Cu, Mn, Fe, Co, and Ni) mixed oxide, J Rare Earths, 2010, 28, 742-746. doi.org/10.1016/S1002-0721(09)60192-7

[36] J. Guan, F. Mou, Z. Sun, W. Shi, Preparation of hollow spheres with controllable interior structures by heterogeneous contraction, Chem. Commun., 2010, 46, 6605-6607. doi.org/10.1039/C0CC01044H

[37] Winter, L.R.; Chen, R.; Chen, X.; Chang, K.; Liu, Z.; Senanayake, S.D.; Ebrahim, A.M.; Chen, J.G. Elucidating the roles of metallic Ni and oxygen vacancies in CO_2 hydrogenation over Ni/CeO_2 using isotope exchange and in situ measurements. Appl. Catal. B Environ. 2019, 245, 360–366. doi.org/10.1016/j.apcatb.2018.12.069

[38] Winter, L.R.; Gomez, E.; Yan, B.; Yao, S.; Chen, J.G. Tuning Ni-catalyzed CO_2 hydrogenation selectivity via Ni-ceria support interactions and Ni-Fe bimetallic formation. Appl. Catal. B Environ. 2018, 224, 442–450. doi.org/10.1016/j.apcatb.2017.10.036

[39] Boaro, M.; Colussi, S.; Trovarelli, A. Ceria-based materials in hydrogenation and reforming reactions for CO_2 valorization. Front. Chem. 2019, *7*, 28. doi.org/10.3389/fchem.2019.00028

[40] L. Wang, H. Liu, Y. Liu, Y. Chen, S. Yang, Influence of preparation method on performance of Ni–CeO_2 catalysts for reverse water-gas shift reaction, J Rare Earths, 2013, 31, 559-564. doi.org/10.1016/S1002-0721(12)60320-2

[41] Peymani, M.; Alavi, S.M.; Rezaei, M. Preparation of highly active and stable nanostructured Ni/CeO_2 catalysts for syngas production by partial oxidation of methane. Int. J. Hydrogen Energy 2016, 41, 6316–6325. doi.org/10.1016/j.ijhydene.2016.03.033

[42] M.P. Allenet al., Introduction to molecular dynamics simulation. Computational soft matter: from synthetic polymers to proteins 2004, 23, 1–28. ISBN3-00-012641-4

[43] J.W. Ponder, D.A.Case, Force fields for protein simulations. Adv. Prot. Chem. 2003, 66, 27-85. doi.org/10.1016/S0065-3233(03)66002-X

[44] T.X.T. Sayle, M.Molinari, S.Das, U.M. BhattaG. Mobus, S.C. Parker,S. Seal, D.C.Sayle, Environment-mediated structure, surface redox activity and reactivity of ceria nanoparticles; Nanoscale. 2013, 13, 6063-73. doi.org/10.1039/c3nr00917c. Epub 2013 May 29.

[45] T. Ch. Lim, J.A. Dawson, A convenient and accurate wide-range parameter relationship between Buckingham and Morse potencial energy funcions; Molecular Physics, 2018, 116,1127-1132. doi.org/10.1080/00268976.2017.1407003

[46] W. L. Jorgensen, J. Chandrasekhar, J. D. Madura, R. W. Impey and M. L. Klein, Comparison of simple potential functions for simulating liquid water, J. Chem. Phys., 1983, 79, 926-935. doi.org/10.1063/1.445869

[47] M/ Abraham, D. van der Spoel, E.Lindahl, B. Hess and the GROMACS development team. GROMACS User Manual version 2016.3. www.gromacs.org, 2017.

[48] http://www.gromacs.org/

[49] https://materialsproject.org/materials/mp-20194/

Conclusions

Summarizing the overall work, the following conclusions can be drawn:

- A number of titanium oxide-based catalysts have been successfully prepared and characterized.

- The photocatalytic production of hydrogen from alcohol-water mixtures and under dynamic conditions with photocatalysts prepared by irradiating with ultraviolet light (365 nm) has been studied.

- Macroporous silicon disks containing ordered channels of 2 μm side and 0.2 mm length functionalized with a thin layer of Au/TiO_2 or Pt/TiO_2 photocatalysts have been prepared and characterized. A normalized photocatalytic hydrogen production rate three orders of magnitude higher than those achieved so far in any conventional photoreactor has been obtained using water-ethanol mixtures in gas phase.

- It was proved that temperature has a positive effect on the photoproduction of hydrogen in the range studied up to 60 °C. In addition, when commercial bioethanol was used in the macroporous silicon structure coated with Pt/TiO_2 the photoproduction of hydrogen improved.

- Composites of TiO_2 with 10 wt. % of reduced graphene oxide (rGO) were successfully prepared by a hydrothermal method and characterized.

- The use of rGO in TiO_2-rGO comoposites allowed for a 10-times higher photoproduction of hydrogen as a result of increasing the life of the electron-hole pairs in TiO_2 as a result of combining them with rGO and suppressing recombination centers.

- TiO_2-rGO composite calcined at 700°C exhibited the highest performance with a hydrogen photogeneration rate of 9.53 mmol h^{-1} g^{-1}.

- A series of Pt/Au-titanium dioxide-activated carbon composite photocatalysts were prepared, characterized and tested for the photoproduction of hydrogen from alcohol-water mixtures in gas phase.

- The highest value of hydrogen production was obtained with the Pt-1TiO_2-AC catalyst, with values of about 19-20 mmol h^{-1} g^{-1}. The better photocatalytic activity exhibited by the M-TiO_2-AC composites has been ascribed to an enhanced electron transport and electron-hole pair lifetime.

- Four distinct shapes of cerium dioxide (polycrystalline, rods, cubes, and octahedral) were successfully prepared and characterized.

- The best oxygen storage and exchange capacity for different shapes of cerium dioxide follow the order: CeO_2-rods>CeO_2-cubes>CeO_2 polycrystalline>CeO_2 octahedral.

- After conducting tests with various metals deposited on the surface of cerium dioxide (Ru, Pd, Au, Pt, Ni), it was found that nickel was the best to improve oxygen storage and exchange.

- It has been demonstrated that the use of the ball milling method compared to the incipient wetness impregnation method for the preparation of the ceria-based catalysts increases their redox capacity.

- A series of Ni-CeO_2 catalysts with 0.5, 1, 2, 5 and 10 wt.% Ni were obtained successfully by ball milling and characterized.

- The best reduction ability was measured for 10%Ni-CeO_2 rods and it was about 811.6 µmol/g_{cat}. The highest reoxidation value was achieved for 2%Ni-CeO_2-rods, and it was about 412 µmol/g_{cat}. As the metal content increases, the reduction capability of the catalyst increases. The ability of reoxidation with the participation of CO_2 decreases at high Ni loadings, which is a direct consequence of the increasing size of the Ni nanoparticles as the amount of nickel increases.

- Molecular dynamics simulations of [111] facets of ceria containing different amount of oxygen vacancies with water molecules were performed.

- Simulations showed that water molecules readily interact with oxygen vacancies of ceria.

- It has been found that the reaction between oxygen vacancies in ceria and water molecules occurs faster for oxygen vacancies forming close to each other. This concludes that clustering of oxygen vacancies in ceria is advantageous for the thermochemical water splitting process.